Weak-link Nb-based scanning nano-SQUID microscope system for local magnetic flux imaging

Yusuke Shibata

Submitted to the Graduate School of
Pure and Applied Sciences
in Partial Fulfillment of the Requirements
for the Degree of Doctor of Philosophy in
Science

at the
University of Tsukuba

Abstract

Superconducting quantum interference devices (SQUIDs) are quantitative magnetic flux detectors with high sensitivity. Nano-SQUIDs have been attracting much attention due to their potential capability for single electron spin detection because the estimated minimum spin flip detection is proportional to the loop size of SQUIDs. Furthermore, nano-SQUIDs have advantages in local magnetic flux imaging. As compared with SQUIDs with tunneling Josephson junction, weak-link SQUIDs have advantage in reducing the size of the SQUID loop. In order to realize an optimal magnetic flux measurement, improvements in reducing thermal hysteretic behavior in I-V relation have been required.

First, I describe on the development of a weak-link Nb-based scanning nano-SQUID probe with negligibly small thermal hysteresis. By utilizing a focused ion beam (FIB) milling, a deep silicon etching (Bosch) process and mechanical polishing, I have successfully reduced the distance between the probe tip and the nearest weak-link junction to 1 μm. The spatial resolution and the magnetic field sensitivity have been estimated to be less than 2 μm and 3.1 nT/Hz$^{1/2}$ at 2 kHz, respectively.

Then a Hall-bar structure sample of a GaAs/Al_xGa_{1-x}As modulation doped single heterojunction has been measured to evaluate the weak-link Nb based nano-SQUID microscope. From scanning measurements of local magnetic flux distributions induced by current flowing in the two-dimensional electron gas (2DEG), I demonstrate that the spatial resolution and the maximum detectable magnetic flux have been improved by using the mechanically polished probe as compared with the probe without polishing. Current density distributions in the 2DEG have been reconstructed from the magnetic flux distributions, and good agreement has been obtained with the current distribution calculated by solving a Laplace equation. The reconstructed current density distributions have revealed ballistic nature of conductance in the 2DEG.

Finally, tungsten carbide (W-C) wire and film fabricated by focused-ion-beam chemical vapor deposition (FIB-CVD) have been investigated by the weak-link Nb-based scanning nano-SQUID microscope. Because of potential large applications as nano-scale superconducting devices, W-C has been attracting much attention, recently. From mappings of magnetic flux induced by currents flowing in tungsten carbide wires, the current density distribution has been reconstructed. Meissner effect in tungsten carbide thin films

has also been investigated by mappings of magnetic flux, showing weakening of Meissner effect in tungsten carbide thin films.

The newly developed weak-link Nb based nano-SQUID microscope has great advantages in local detection and imaging of magnetic flux from small and fine objects in micro- to nano- range.

Contents

Chapter 1

Introduction

A local magnetic flux imaging is a powerful technique for investigations of solid state physics to latest industrial applications. With remarkable growth of nano-fabrication technologies, new probes with ever higher magnetic field sensitivity and ever more precise resolution are required. A superconducting quantum interference device (SQUID) [1, 2] is one of the promising techniques for local magnetic flux measurements because of its potential for single spin detection [3].

For utilizing SQUIDs as a probe for a local magnetic flux imaging, we should address technical challenges to improve a spatial resolution and a magnetic flux sensitivity. A miniaturization of a SQUID loop is one of the important guidelines to solve the technical challenges [3, 4, 5]. By comparing with weak-link Josephson junctions, tunneling Josephson junctions have relatively small critical current I_0. As a result, conventional SQUIDs, incorporating tunneling Josephson junction, generally have dimensions greater than 1 μm, due to junction current density limitations [6, 7]. The limitations come from a relationship of $2LI_0/\Phi_0 \approx 1$ for optimal SQUID operation [8, 9]. Here L is a SQUID inductance, which is proportional to a SQUID loop size, and $\Phi_0 \approx 2.07 \times 10^{-15}$ Tm^2 is a magnetic flux quantum. Because of relatively large I_c, weak link Josephson junctions have advantage for reducing the dimension of SQUID. A weak-link Josephson junction, called Dayem bridge, consists of a superconductor with nanometric constriction which can be fabricated by a single patterning process. As compared with tunneling Josephson junctions, which are fabricated by consecutive lithography processes and generally have three-dimensional configurations, a single patterning process is more suitable for preparing a scanning probe, and moreover, a simple planar

structure of weak-link SQUID is more resistant to the magnetic field applied in the plane of the SQUID loop [6, 10, 11]. The insensitivity to a high magnetic field applied in the SQUID plane is a necessary requirement for measurements of the properties of the two-dimensional electron system.

On the other hand, the presence of thermal hysteresis in current-voltage (I-V) characteristics of a weak-link Josephson junction prevent us from operating the SQUID as a magnetic flux to voltage transducer [10, 12]. Because of the thermal hysteresis, weak-link Josephson junctions have generally been regarded as too noisy for operation at the highest sensitivity level. There has been several investigations on SQUIDs based on weak-link Josephson junction in order to reduce the hysteretic behavior [13, 7, 6].

In this thesis, we describe construction, characterization, and some applicatoins of our weak-link scanning nano-SQUID microscope with small hysteresis in I-V characteristics.

1.1 Introduction to SQUID

A SQUID is known to be a highly sensitive magnetic flux probe utilizing the Josephson effect. The phase difference of two superconducting electrodes is detected as a change of macroscopic current in a dc-SQUID. A dc-SQUID has been widely used for a magnetic probe with high sensitivity in a wide variety of fields from medicine to engineering. A dc-SQUID is composed of a superconducting loop with two Josephson junctions. One of the advantages of the dc-SQUID is that the quantitatively accurate magnetic flux Φ penetrating the superconducting loop can be measured by detecting the SQUID critical supercurrent I_c as given by,

$$I_c = 2I_0|\cos(\pi\Phi/\Phi_0)| \tag{1.1}$$

where I_0 is a critical current of a Josephson junction and Φ_0 is a magnetic flux quantum [1]. From Eq. (1.1), critical current I_c is modulated sinusoidally as a function of magnetic flux Φ with a period of Φ_0. Because Φ is integration of magnetic field B over the effective area of the superconducting loop, magnetic field sensitivity is improved with increasing the loop area. For practical use as a magnetic field sensor, a superconducting loop diameter is often over several dozens of μm [14, 15].

Recently, remarkable developments of fabrication techniques in nanoscale range have open up possibilities for preparing magnetic sensors that are suit-

able to local measurements. With decrease in the area of a superconducting loop, while magnetic field sensitivity to an uniform magnetic field is reduced, it has been shown that the sensitivity to a local magnetic dipole moment is improved because the minimum detectable energy change decreases with decrease in the area of a superconducting loop. [16, 9, 17, 18, 3, 19] For a local magnetic flux measurement, there are three important factors to be considered: first, spatial resolution of magnetic flux measurement, second, sensitivity to external magnetic field, and third, coupling efficiency between a SQUID and a targeted local magnetic dipole moment to be measured. Nano-SQUIDs have been intensively investigated because of the third property of decrease in the minimum detectable energy change with reduction of area of a SQUID loop [16, 9, 17, 18, 3, 19]. For this unique property, nano-SQUIDs are considered as promising devices for single electron spin detection. I will further describe on this in the following Section.

Using an electron-beam lithography and reactive ion etching, Lam and Tilbrook developed a nano-SQUID based on Au/Nb thin film with the loop size of 200 nm [20]. They reported a magnetic flux sensitivity of $7\times10^{-6}\Phi_0/\mathrm{Hz}^{1/2}$ that corresponded to spin sensitivity of 250 spin/$\mathrm{Hz}^{1/2}$ in their nano-SQUIDs. Hao et al. also investigated a Nb/W based nano-SQUID fabricated by a FIB technique [6]. The magnetic flux sensitivity was around $0.2\times10^{-6}\Phi_0/\mathrm{Hz}^{1/2}$. These studies indicate the wide possibilities of nano-SQUIDs for a local magnetic dipole moment measurement. For an effective magnetic coupling between a dc-SQUID and a nanometer-scale samples, several techniques have been demonstrated by Wernsdorfer and his collaborators [21, 22, 23]. They successfully investigated magnetic susceptibilities of nano-size ferromagnetic samples that were positioned on the surface of a dc-SQUID or directly embedded in a dc-SQUID. Their results indicate that a well-established magnetic coupling is a key to local magnetic imagings by scanning probe measurements.

1.2 Trade off between magnetic field sensitivity and spatial resolution

A trade-off between spatial resolution and magnetic field sensitivity exists in recent local magnetic imaging techniques. A magnetic force microscope (MFM) shows one of the highest spatial resolution based on atomic force mi-

croscope technique. MFM can resolve magnetic structures in several nanometer range, however, the magnetic field sensitivity is of the order of milli tesla [24]. Hall devices are also used as magnetic field detector for scanning magnetic imaging. In a standard GaAs-2DEG Hall structure, a depletion layer thickness limits the size of the Hall structure. Thus alternative materials for Hall devices have been developed for higher spatial resolution magnetic imaging, such as a single crystal InSb Hall probe with the area of a 1.5 μm^2 [25], which showed magnetic field sensitivity of 0.6 μT/Hz$^{1/2}$. Sandhu et al. developed a Bi based scanning Hall probe microscope which was fabricated by optical lithography and FIB milling process [26]. The size of Hall probe was reduced to 50 nm $\times$ 50 nm and an optimum magnetic field sensitivity was 80 μ T/Hz$^{1/2}$. MFM and scanning Hall probe microscope have advantages in spatial resolution for local magnetic imaging. On the other hand, Kominis reported an ultra-high magnetic field sensitivity of sub-femto tesla by using thermal atom magnetometer (TAM) based on Larmor precession of spin-polarized atom [27] but the spatial resolution was sub-milimeter range. Efforts has been made to achieve both higher sensitivity and higher spatial resolution by breaking this trade-off. One of the most promising techniques is to use a nitrogen vacancy center in nano-diamond as a probe for a magnetic field sensor. A nitrogen vacancy center has been attracting much attention recently as a possible magnetic probe with high magnetic field sensitivity and high spatial resolution at room temperature. Optical detection of electron paramagnetic resonance from single nitrogen vacancy center was reported in 1997 [28], opening up possibilities to use a nitrogen vacancy center for a local magnetic probe with high sensitivity and spatial resolution. Magnetic field sensitivity of nitrogen vacancy centers is based on Zeeman splitting of spin triplet ground state. Degeneracy of the spin triplet ground state is lifted under finite magnetic field and the separation is given by $2\gamma\ B_z$, where $\gamma = 2\pi \times 28$ GHz/T is gyromagnetic ratio of the electron and B_z is the component of magnetic field parallel to the nitrogen vacancy axis. Thus a nitogen vacancy center can detect magnetic field without any limitation of scaling law. Improvements for magnetic spatial resolution are expected. This Zeeman splitting energy is measured by observation of drop of the luminescence intensity from negatively charged nitrogen vacancy center by sweeping the frequency of the externally applied microwave. Typical sensitivity for DC detection is 0.36 μT/Hz$^{1/2}$ [29].

In the case of scanning SQUID microscope, there is a trade off between magnetic field sensitivity and spatial resolution because a SQUID detects

change of magnetic flux Φ with period of Φ_0. Magnetic flux Φ is integrated magnetic field within the SQUID loop area as given by

$$\Phi = S \times B_{\perp}, \tag{1.2}$$

where S is the SQUID loop area and $B_{\perp}$ is the magnetic field component normal to the SQUID loop. For a fixed $\Phi = \Phi_0$, $B_{\perp}$ increases with decreasing the SQUID loop area S. This is associated with degradation of magnetic field sensitivity of SQUID. In order to achieve high spatial resolution, one should decrease the size of SQUID loop and should compromise with magnetic field sensitivity.

Still, SQUIDs have pursued as local probes of magnetic flux by reducing the size of a SQUID loop [30, 5, 15, 31]. This is because the minimum detectable energy change is proportional to $k_B T(LC)^{1/2}$ [16, 9, 17, 18, 3, 19], where T, L, and C are the temperature, the inductance of SQUID loop, and the capacitance of junction, respectively. The inductance L is proportional to the size of SQUID loop. As a result, the minimum detectable energy change is expected to be improved with decrease in the size of SQUID. For this reason, nano-SQUIDs have been attracting much attention due to their potential capability for single electron spin detection. [21] For local magnetic imaging, scanning nano-SQUID microscope system have been developed in recent years as described in the following section.

1.3 Local magnetic imaging by scanning-SQUID

Scanning SQUID microscope techniques have been developed to image various kind of magnetic phenomena.

For room temperature objects, for example, bioelectric currents in living tissue or electrical circuits, scanning SQUID microscope have been developed because of its high magnetic field sensitivity. Baudenbacher et al. reported magnetic field imaging at room temperature using niobium based SQUID sensor which was thermally connected to liquid Helium reservoir [14]. A spatial resolution and magnetic flux sensitivity of the system were about 100 μm and $5 \times 10^{-6}\Phi_0/\mathrm{Hz}^{1/2}$. High-temperature cuprate superconductor based SQUID has also been used for room temperature measurement. Faley et al. developed $YBa_2Cu_3O_{7-x}$ based dc SQUID sensor with spatial resolution of 25 μm and magnetic flux sensitivity of $5 \times 10^{-5}\Phi_0/\mathrm{Hz}^{1/2}$. [15] In these SQUID

microscopes, the spatial resolutions were mainly limited by the distance between the magnetic sensor and the sample placed at room temperature.

In cryogenic environments, magnetic sensors, SQUIDs or pick up coils, can directly couple to a sample. Thus improvements in spatial resolution and magnetic coupling are expected. Vu et al. reported imaging measurement of trapped vortices in two-dimensional superconductor arrays using Nb-trilayer dc SQUID with 10 μm spatial resolution and a magnetic sensitivity of about $3 \times 10^{-6}\Phi_0$ [32]. In their equipment, SQUID probe, which was fabricated within 50 μm of a probe edge, was magnetically coupled directly to test object without a pick up loop. Tokura et al. investigated the ballistic-electron current distribution in GaAs/Al_xGa_{1-x}As modulation-doped heterostructure by using a scanning dc micro-SQUIDs array with an effective area of $(14\ \mu\mathrm{m})^2$ and with a noise level of $\approx 10^{-5}\Phi_0/\mathrm{Hz}^{1/2}$ [33]. In their results, the current distribution was successively reconstructed from the magnetic imaging at the constant height of 8 μm. Hasselbach et al. reported the importance of miniaturizing a SQUID loop and reducing the distance between a sensor and a sample in order to obtain the highest possible spatial and magnetic resolution for a scanning SQUID microscope [5]. They also developed dc SQUID probes composed of Dayem bridges with niobium and aluminum thin film [34]. The diameter of the SQUIDs and the distance from the tip were 1 μm and few micrometers, respectively. The Al based SQUID probe were operated at 0.45 K with magnetic flux sensitivity of $10^{-3}\Phi_0/\mathrm{Hz}^{1/2}$. A highly integrated gradiometric SQUID susceptometer with a 0.6 μm diameter pickup coil were developed by Koshnick et al. [35] In their probe, SQUID was fabricated far from a probe edge and magnetically connected with pickup loop placed on the edge. They achieved magnetic flux resolution of $2.5 \times 10^{-7}\Phi_0/\mathrm{Hz}^{1/2}$ above 10 kHz at 125 mK. The same system was used for investigating current distributions in topological superconductor [36] and anomalous quantum Hall samples [37]. A scanning probe with the smallest dc SQUID loop diameter of 46 nm was fabricated on a sharpened quartz tube tip by Vasyukov et al. [31] Thermally evaporated Pb composed a dc SQUID on the tip. A flux noise of the nano-SQUID was reached at 50 $\mathrm{n}\Phi_0/\mathrm{Hz}^{1/2}$, which was lower than single electron spin sensitivity.

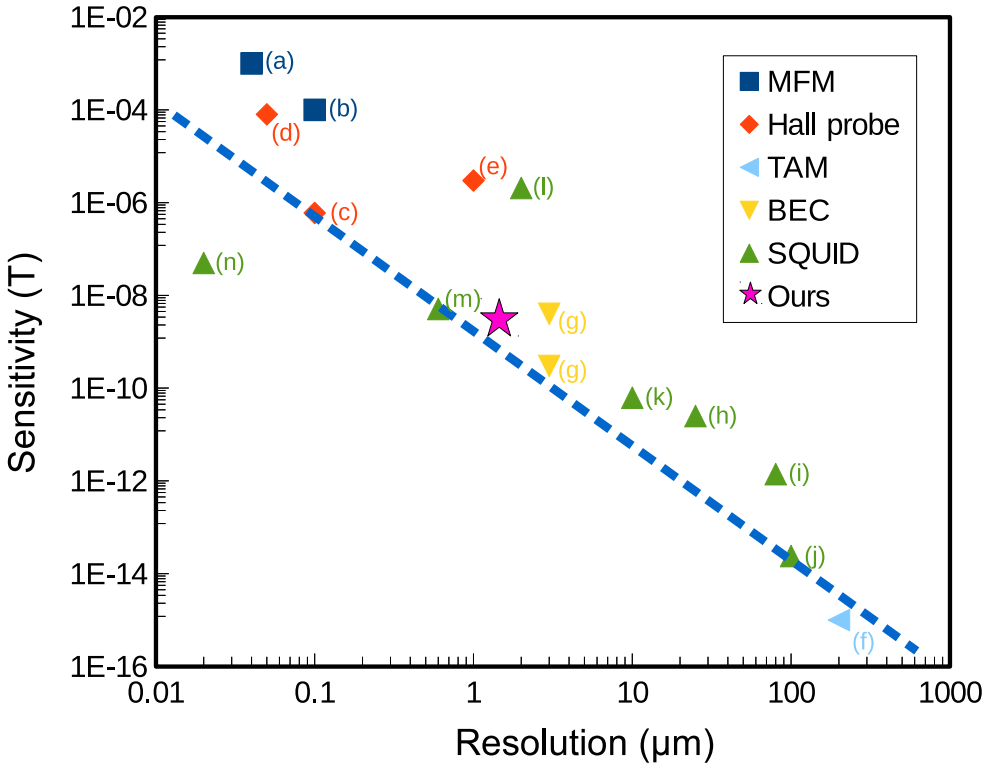

Fig. 1.1: Magnetic field sensitivity versus spatial resolution for several types of magnetic microscopes. (a) [24] and (b) [38] are magnetic force microscopes (MFM). (c) [25], (d) [26] and (e) [39] are scanning Hall probe microscopes. (f) [27] is a thermal atomic magnetometer (TAM). (g) [40] is a magnetic sensor based on Bose-Einstein condensate (BEC). (h) [15], (i) [14], (j) [41], (k) [32], (l) [34], (m) [35] and (n) [31] are scanning SQUID microscopes. The result of this work is shown by the star mark.

1.4 Purpose of this thesis

A weak-link nano-SQUID has a promising technology for local magnetic flux imaging, but the hysteretic behavior in I-V characteristics prevented us from setting optimal measurement operation condition. First purpose of this thesis is to develop a novel scanning nano-SQUID microscope based on weak-link Josephson junctions with sufficiently-small hysteresis that enables the SQUID to be operated as a magnetic flux to voltage transducer. I set the target of spatial resolution and magnetic sensitivity of SQUID microscope to be the order of 1 μm and 1 nT/Hz$^{1/2}$, respectively. Spatial resolution has been set to be comparable to the estimated penetration depth of tungsten carbide superconductor [42]. Magnetic field sensitivity has been set to be on the empirical trade-off line in Fig. 1.1.

Second purpose is to investigate current density distributions in a two-dimensional electron system from local magnetic flux imaging. This contributes to evaluate the performance of our weak-link Nb based scanning nano-SQUID microscope. Moreover, this may contributes to reveal the properties of ballistic carriers in a high-mobility GaAs/Al_xGa_{1-x}As modulation-doped single heterojunction sample as compared with electrons in a diffusive metal electrode.

Third purpose is to investigate the superconducting characteristics of tungsten carbide (W-C) films deposited by a focused-ion-beam chemical vapor deposition (FIB-CVD) technique by imaging local magnetic flux around W-C films. FIB-CVD depositions of superconducting films has been acquired much interest as a template-free method to fabricate superconducting circuits such as nano-SQUIDs. Clarification of superconducting characteristics of W-C films are important both practically and as a basic science.

1.5 A weak-link Nb based scanning nano-SQUID probe

A small thermal hysteresis

As previously indicated, weak-link Josephson junctions have several advantages for decreasing the dimensions of SQUID in spite of the presence of thermal hysteresis in I-V characteristics. In order to solve this issue, we have introduced a gold film on a thin niobium superconductor. The gold film acts

as a heat sink, a shunt resistor, and a protection film. The hysteretic behavior, which mainly comes from heat generations of the junctions at normal conducting state, can be suppressed by a heat sink [6, 20]. Moreover, the gold film protects the niobium superconducting film from unintended injections of Ga^+ ion during FIB milling processes, which is a cause of degradation of superconductivity [13, 7], This protection film enables us to employ fabrication processes utilizing FIB milling.

A shunt resistor is also important to reduce hysteresis as will be described in more details in Sec. 1.5. Thus the introduction of a gold film on a thin niobium superconductor is one of the keys for our successful development of a weak-link Nb-based nano-SQUID with small hysteresis at liquid He^4 temperature.

A high-precision scanning SQUID probe

Fabrication processes for dc SQUIDs have been developed over several decades [2]. Conventionally, a tunnel type Josephson junction has been widely used. Fabrication process of a tunneling Josephson junction, where two bulk superconductors are separated by a thin insulating layer, is based on the lithography process using spin-coated resist films. Because of unintentional increase of the resist thickness near the substrate edge, it is difficult to fabricate devices precisely at the edge of a scanning probe.

An FIB milling technique has been developed as a mask-less fabrication process for structures in the length-scale of micrometers to nanometers [43, 6, 44, 13, 7]. Typical FIB system employs gallium atom as an ion source. High-energy accelerated ions incident to a sample surface play two roles, *i.e.*, implantation of ions and milling a targeted object. Because of its great potential for fabrications and improvements of devices, FIB has been widely used to produce fine structures in a variety of researches. Weak-link Josephson junctions [45, 20] have advantages in that fabrication by milling without lithography process and observation of the resultant SQUID loop may be performed in situ by a FIB. High-precision FIB milling process enables us to fabricate weak-link Josephson junctions in nanometer scale without any mask or lithography processes.

In order to take advantages of FIB, we have developed a scanning probe, which is a thin silicon substrate with four terminal superconducting circuit at the substrate edge, by using a silicon deep etching (Bosch) process. The Bosch process enables us to prepare several dozen of probes at once.

From these processes, we have developed weak-link Nb-based scanning nano-SQUID probes within several μm from the tip of the Si probes. The SQUID has the loop size of about 1 μm and the widths of the loop and the weak-link were 0.5 μm and 80 nm, respectively. The geometrical inductance $L = 5\mu_0\alpha/16$, where α is the inner circumference of the SQUID [46] was 1.6 pH. The effect of the self-induced field as given by $\beta_m = 2LI_c/\Phi_0$ was 0.32. These results are adequately satisfy the condition in Eq. (1.62). As indicated in the following sections, the SQUID is wedged between wide terminals which acts as a large heat sink. These high-precision patterning contribute to optimal scanning SQUID operations.

An effective magnetic coupling

For a local magnetic imaging using scanning SQUID microscope, the distance between the SQUID and the object under test is one of the important parameters. Magnetic field $\mathbf{B}(\mathbf{r})$ induced by the current density $\mathbf{J}(\mathbf{r})$ is given by the law of Biot and Savart

$$\mathbf{B}(\mathbf{r}) = \frac{\mu_0}{4\pi}\int \frac{\mathbf{J}(\mathbf{r}')\times(\mathbf{r}-\mathbf{r}')}{|\mathbf{r}-\mathbf{r}'|^3}d^3\mathbf{r}'. \tag{1.3}$$

As described the law of Biot and Savart, the magnetic field decreases with increasing the distance between the SQUID probe and the current source. A similar argument holds for magnetic field produced by a magnetic moment. To achieve the highest possible spatial and magnetic field resolutions of a scanning SQUID measurement, reduction of the distance between the SQUID probe and the current source or the magnetic moment is simple but the most effective way [5, 47].

In our fabrication process of SQUID probes, there were degradation of superconductivity at the tip of probe substrate. The degradation was mainly originated from the Bosch process as described in the following Chapter. This unintended effect prevents us from locating the weak-link SQUID at the very edge of the probe tip. Thus, we have introduced a mechanical polishing process to remove the unavoidable degradation region.

By using the mechanical polishing process, we have improved the distance between the SQUID probe and the object under test. As shown in Fig. 2.6(b), the nearest weak-link Josephson junction to the probe tip was located within about 1 μm from the edge. Consequently, we could improve the spatial resolution and the magnetic coupling in local magnetic flux measurements

induced by current flowing in the two-dimensional electron system. We will describe in more details on the method of the measurements in Chapter 4.

1.6 Theoretical backgrounds

Traditional BCS type and other several type of superconductor are characterized by the macroscopic wave function which is also called order parameter. Contrary to superfluidity, as an allied phenomenon comes from Bose-Einstein condensation, charged particles take the center role in superconductor. These particles, electron pairs or quasi particles, is strongly coupled with electromagnetic field which is the gauge invariant system.

A principle of SQUID properties to an applied magnetic field is explained by Josephson effect of superconductor. In the history of theoretical prediction and discovery, Josephson effect was investigated in superconducting tunnel junctions. However Josephson effect is generally observed in not only tunnel junction but also other type junctions which consist of weakly linked superconductors. This phenomenon is widely understood by Ginzburg-Landau (GL) theory which is able to explain about the behavior of the macroscopic wave function in inhomogeneous superconductors.

1.6.1 Ginzburg-Landau theory

BCS theory is known to explain superconductivity in a bulk superconductor with spatially homogeneous superconducting energy gap [48]. By contrast, Ginzburg-Landau theory is widely used to explain superconductivity in spatially inhomogeneous devices. In the followings, a Josephson junction is modeled based on Ginzburg-Landau theory [49, 50, 51].
We introduce a pseudo-wave function $\Psi(\mathbf{r})$ as a complex order parameter in a superconductor. $|\Psi(\mathbf{r})|^2$ corresponds to a local density $n_s(\mathbf{r})$ of superconducting electron pairs. We assume small $\Psi(\mathbf{r})$ and small spatial variation of $\Psi(\mathbf{r})$. A free energy density f_s is expanded in a power series in $|\Psi(\mathbf{r})|^2$. Using a variational principle, we will develop an expression for Ginzburg-Landau (GL) differential equation.

According to GL theory, a free energy density is given by

$$f_s = f_{n0} + \alpha|\Psi|^2 + \frac{\beta}{2}|\Psi|^4 + \frac{1}{2m^*}\left|\left(\frac{\hbar}{i}\nabla - e^*\mathbf{A}\right)\Psi\right|^2 + \frac{\mu_0 H^2}{2}, \qquad (1.4)$$

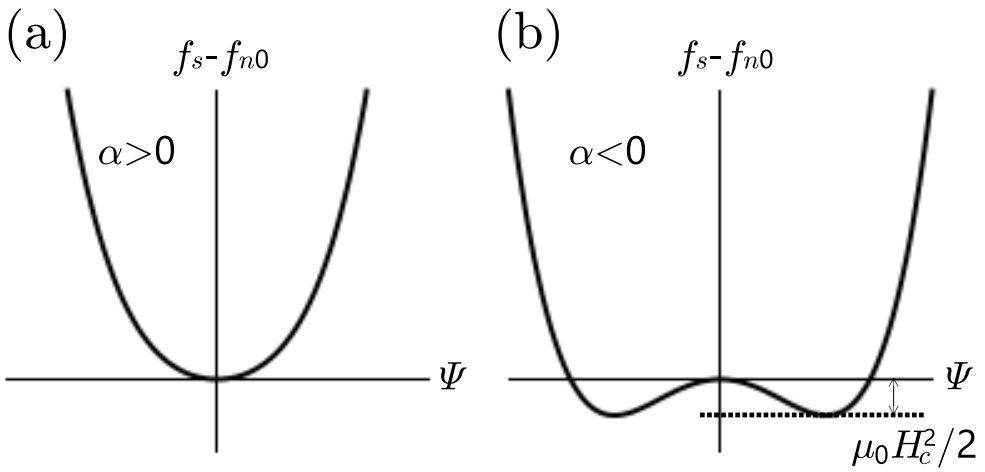

Fig. 1.2: Schematic illustrations of a free energy density described by Eq.(1.5) for the case of $\beta > 0$. (a) and (b) are show the case of α is positive and negative, respectively.

where f_{n0} is an energy density of a normal state, α and β are expansion coefficients, and $m^*$and e^* are the effective mass and the effective charge of pseudo-wave function, respectively. [49] According to a microscopic theory of Gor'kov [52], the correct value of e^* is corresponding to the value of an electron pair of $2e$. The effective mass m^* is nearly identical to $2m$ which is double value of the mass of a free electron [51]. The last term in the right side $\frac{\mu_0 H^2}{2}$ in Eq.(1.4) is the energy from magnetic field as given by $\mathbf{H} = \frac{1}{\mu_0}\nabla \times \mathbf{A}$. In the case of $\Psi = 0$, Eq.(1.4) gives the ground state of a normal conductor in magnetic field.

First, we assume that the gradient of Ψ is negligibly small and that the vector potential $\mathbf{A}$ is zero in order to investigate temperature dependencies of α and β. The difference in the free energies in a superconducting state and a normal state is given by

$$f_s - f_{n0} = \alpha|\Psi|^2 + \frac{\beta}{2}|\Psi|^4, \tag{1.5}$$

which is a power series expansion of superconducting electron density $|\psi|^2 = n_s$. β has to be positive to have a minimum free energy state at finite $|\Psi|^2$. Fig. 1.2 shows schematic illustrations of Eq.(1.5) for positive β. If α is positive, the free energy has a local minimum at $|\Psi|^2 = 0$. This corresponds

to a normal conducting state. On the other hand, if α is negative, the energy difference has a local minimum under the condition

$$|\psi|^2 = |\psi_\infty|^2 = \frac{\alpha}{\beta}, \tag{1.6}$$

where Ψ_∞ is a pseudo-wave function of a superconducting state far from the sample surface, and is well shielded from the disturbance of surface current or magnetic field at the surface. According to the definition of thermodynamic critical magnetic field $H_c(T)$, the difference in the free energies at zero magnetic field is given by

$$f_n - f_s = \frac{\mu_0}{2} H_c(T)^2 = \frac{\alpha^2}{2\beta} \tag{1.7}$$

by substituting Eq.(1.6) into Eq.(1.5). Critical temperature T_c is defined by the highest temperature where the free energy of the state at $|\Psi|^2 \neq 0$ is lower than that of the state at $|\Psi|^2 = 0$. Consequently we obtain

$$\begin{aligned} \alpha < 0 &: (T < T_c) \\ \alpha \geq 0 &: (T \geq T_c). \end{aligned}$$

If temperature is set close to T_c, α takes a value around zero. The sign of α must change at $T = T_c$. We consider a Taylor expansion of α around $T = T_c$ as

$$\alpha(t) = \alpha'(t-1), \tag{1.8}$$

where we have defined $t = T/T_c$. The term which contains the vector potential $\mathbf{A}$ and the gradient of Ψ in Eq.(1.4) is rewritten by using the order parameter $\Psi = |\Psi| e^{i\phi}$ as

$$\begin{aligned} & \frac{1}{2m^*} \left| \left(\frac{\hbar}{i} \nabla - e^* \mathbf{A} \right) \Psi \right|^2 \\ = & \frac{1}{2m^*} \left| \frac{\hbar}{i} \nabla |\Psi| e^{i\phi} + \frac{\hbar}{i} |\Psi| e^{i\phi} i \nabla \phi - e^* \mathbf{A} |\Psi| e^{i\phi} \right|^2 \\ = & \frac{1}{2m^*} \left| \left(\frac{\hbar}{i} \nabla |\Psi| + \hbar |\Psi| \nabla \phi - e^* \mathbf{A} |\Psi| \right) e^{i\phi} \right|^2 \\ = & \frac{1}{2m^*} \left| \frac{\hbar}{i} \nabla |\Psi| + (\hbar \nabla \phi - e^* \mathbf{A} |\Psi|) \right|^2 \\ = & \frac{1}{2m^*} \left[\hbar^2 (\nabla |\Psi|)^2 + (\hbar \nabla \phi - e^* \mathbf{A})^2 |\Psi|^2 \right]. \end{aligned} \tag{1.9}$$

Here the first term is the excess energy due to the gradient of the the intensity of the order parameter, and the second term is the kinetic energy of the gauge-invariant superconducting current.

1.6.2 Ginzburg-Landau differential equation

In this section, we consider minimization of the GL free energy (Eq.(1.4)) with respect to Ψ and $\mathbf{A}$. [50, 51] Without any boundary conditions to magnetic field, current or the gradient of current, the free energy is minimum at $\Psi = \Psi_\infty$. Under application of specific boundary conditions, the order parameter Ψ is adjusted such that to minimize the total free energy as given by the volume integration of Eq.(1.4). According to a variational principle, an Euler differential equation of Eq.(1.4) is given by

$$\begin{aligned} & \frac{\partial}{\partial \Psi^*}\left[f_{n0} + \alpha\Psi^*\Psi + \frac{\beta}{2}\Psi^{*2}\Psi^2 + \frac{1}{2m^*}\left|\left(\frac{\hbar}{i}\nabla - e^*\mathbf{A}\right)\Psi\right|^2 + \frac{\mu_0 H^2}{2}\right] \\ = \;& \alpha\Psi + \beta|\Psi|^2\Psi + \frac{1}{2m^*}\left(\frac{\hbar}{i}\nabla - e^*\mathbf{A}\right)^2\Psi = 0. \end{aligned} \tag{1.10}$$

The order parameter in a spatially inhomogeneous system is described by solving the differential equation Eq.(1.10) with appropriate boundary conditions.

A quantum-mechanical description of the current operator is derived by minimizing with respect to the vector potential
$\mathbf{A}(A_x(x,y,z), A_y(x,y,z), A_z(x,y,z))$. An Euler differential equation is given by

$$\frac{\partial}{\partial A_i}f - \frac{d}{dx}\frac{\partial f}{\partial A_{ix}} - \frac{d}{dy}\frac{\partial f}{\partial A_{iy}} - \frac{d}{dx}\frac{\partial f}{\partial A_{iz}} = 0 \tag{1.11}$$

where we define $i = (x, y, z)$ and $(A_{ix}, A_{iy}, A_{iz}) = \left(\frac{\partial A_i}{\partial x}, \frac{\partial A_i}{\partial y}, \frac{\partial A_i}{\partial z}\right)$ [53]. The partial derivative with respect to $\mathbf{A}$ is calculated as

$$\begin{aligned} & \frac{\partial}{\partial \mathbf{A}}\left[\frac{1}{2m^*}\left|\left(\frac{\hbar}{i}\nabla - e^*\mathbf{A}\right)\Psi\right|^2\right] \\ = \;& \frac{1}{2m^*}\frac{\partial}{\partial \mathbf{A}}\left[\hbar^2\nabla\Psi^*\nabla\Psi - \frac{\hbar e^*}{i}\Psi^*\nabla\Psi\mathbf{A} + \frac{\hbar e^*}{i}\Psi\nabla\Psi^*\mathbf{A} + (e^*\mathbf{A})^2\Psi^*\Psi\right] \\ = \;& \frac{1}{2m^*}\left[\frac{\hbar e^*}{i}\left(\Psi\nabla\Psi^* - \Psi^*\nabla\Psi\right) + 2e^{*2}\mathbf{A}\Psi^*\Psi\right]. \end{aligned} \tag{1.12}$$

Other terms in Eq.(1.11) are zero for GL free energy function f except for the energy from magnetic field $H = \frac{1}{\mu_0}\nabla \times \mathbf{A}$. The energy term from magnetic field may be written except for the coefficient as

$$\begin{aligned}(\nabla \times \mathbf{A})^2 &= (A_{zy})^2 - 2(A_{zy}A_{yz}) + (A_{yz})^2 \\ &\quad +(A_{xz})^2 - 2(A_{xz}A_{zx}) + (A_{zx})^2 \\ &\quad +(A_{yx})^2 - 2(A_{yx}A_{xy}) + (A_{xy})^2. \end{aligned} \tag{1.13}$$

By using Eq.(1.13), the x component of Eq.(1.11) is calculated as

$$\begin{aligned}&\left(\frac{\partial}{\partial A_x} - \frac{d}{dx}\frac{\partial}{\partial A_{xx}} - \frac{d}{dy}\frac{\partial}{\partial A_{xy}} - \frac{d}{dz}\frac{\partial}{\partial A_{xz}}\right)(\nabla \times \mathbf{A})^2 \\ &= -\frac{d}{dy}(2A_{xy} - 2A_{yx}) - \frac{d}{dz}(2A_{xz} - 2A_{zx}) \\ &= 2\left[\frac{d^2}{dxdy}A_y + \frac{d^2}{dxdz}A_z - \left(\frac{d^2}{dy^2} + \frac{d^2}{dz^2}\right)A_x\right] \\ &= 2(\nabla \times \nabla \times \mathbf{A})_x. \end{aligned} \tag{1.14}$$

We have used a formula of vector analysis $\nabla \times \nabla \times \mathbf{A} = \nabla\nabla\mathbf{A} - \Delta\mathbf{A}$ for the last equation. y and z components may be calculated similarly. From Eqs.(1.12) and (1.14), Euler differential equation of GL free energy function is given by

$$\frac{\hbar e^*}{2m^* i}\left(\Psi\nabla\Psi^* - \Psi^*\nabla\Psi\right) + \frac{e^{*2}}{m^*}\mathbf{A}\Psi^*\Psi + \frac{1}{\mu_0}\nabla \times \nabla \times \mathbf{A} = 0.$$

Considering the relationship $\mathbf{J} = \frac{1}{\mu_0}\nabla \times \nabla \times \mathbf{A}$, where $\mathbf{J}$ is the current density of supercurrent, we obtain

$$\mathbf{J} = \frac{\hbar e^*}{2m^* i}\left(\Psi^*\nabla\Psi - \Psi\nabla\Psi^*\right) - \frac{e^{*2}}{m^*}\Psi^*\Psi\mathbf{A}. \tag{1.15}$$

This form is identical to the quantum mechanical representation of the current induced by a particle with mass m^*, charge e^* and wave function $\Psi(r)$ [50, 51]. The current $\mathbf{J}$ may also be rewritten by

$$\mathbf{J} = \frac{e^*}{m^*}|\Psi|^2\left(\hbar\nabla\phi - e^*\mathbf{A}\right) = e^*|\Psi|^2\mathbf{v}_s. \tag{1.16}$$

1.6.3 Ginzburg-Landau coherence length

In this section, we model a weak-link type Josephson junction using GL differential equation Eq.(1.10). We consider one dimensional system with $\mathbf{A} = 0$ for simplicity [50, 51]. The order parameter Ψ is normalized by Ψ_∞, which is the order parameter at the position far from the surface of a bulk superconductor. By using the normalized order parameter $f = \frac{\Psi}{\Psi_\infty}$, Eq.(1.10) can be calculated as

$$\begin{aligned}
\alpha\frac{\Psi}{\Psi_\infty} + \beta|\Psi_\infty|^2\left|\frac{\Psi}{\Psi_\infty}\right|^2\left(\frac{\Psi}{\Psi_\infty}\right) - \frac{\hbar^2}{2m^*}\left(\frac{d^2}{dx^2}\frac{\Psi}{\Psi_\infty}\right) &= 0 \\
\alpha f + \beta|\Psi_\infty|^2|f|^2 f - \frac{\hbar^2}{2m^*}\frac{d^2}{dx^2}f &= 0 \\
\alpha f - \alpha|f|^2 f - \frac{\hbar^2}{2m^*}\frac{d^2}{dx^2}f &= 0 \\
-|\alpha|f + |\alpha||f|^2 f - \frac{\hbar^2}{2m^*}\frac{d^2}{dx^2}f &= 0 \\
\frac{\hbar^2}{2m^*|\alpha|}\frac{d^2}{dx^2}f + f - |f|^2 f &= 0 \\
\xi^2(T)\frac{d^2}{dx^2}f + f - |f|^2 f &= 0, \qquad (1.17)
\end{aligned}$$

where we have used $\Psi_\infty^2 = \frac{-\alpha}{\beta} > 0$ and $\alpha < 0$ at temperatures T below the critical temperature T_c. Here we define $\xi(T)$ as a length scale corresponding to the spatial variation of the order parameter. $\xi(T)$ is known as Ginzburg-Landau coherence length.

$$\xi(T)^2 = \frac{\hbar^2}{2m^*|\alpha|} \propto \frac{1}{1-t} \qquad (1.18)$$

1.6.4 DC Josephson effect

In the previous section, a one dimensional Ginzburg-Landau differential equation has been derived. By using Eq.(1.17), we will describe the relationship between super-current and phase difference in a weak-link type Josephson junction [50]. We assume that two bulk superconductor L and R are connected with one dimensional bridge structure. A schematic illustration of

the bridge structure is shown in Fig. 1.3 . The length of the bridge satisfies $d \ll \xi$, where ξ is a GL coherence length. We assume that the system is made from a single type of superconductor. In the absence of a magnetic field and at the temperature below T_c, the order parameter is given by Eq.(1.17). We introduce a phase difference $\Delta\phi = \phi_R - \phi_L$, where ϕ_L and ϕ_R are the phases of the order parameter in bulk superconductor L and R, respectively. Boundary conditions are set such that the phase difference is zero at $x = 0$ and $\Delta\phi$ at $x = d$. The normalized order parameter f satisfies

$$\begin{aligned} f &= 1 \quad at \quad x = 0 \\ f &= e^{i\Delta\phi} \quad at \quad x = d. \end{aligned}$$

According to Aslamazov and Larkin [54], if the bridge length satisfies $d \ll \xi$, $\left(\frac{\xi}{d}\right)^2$ is much larger than 1. Because the absolute value of normalized order parameter $|f|$ is smaller than 1, the leading term in Eq.(1.17) is $\xi^2 \frac{d^2}{dx^2} f$. We rewrite Eq.(1.17) and obtain a Laplace equation

$$\frac{d^2}{dx^2} f = 0. \tag{1.19}$$

A conventional solution to Eq.(1.19) is $f = a + bx$. Applying the above boundary conditions, a and b are given by solving

$$f(0) \;=\; a + 0 = 1$$

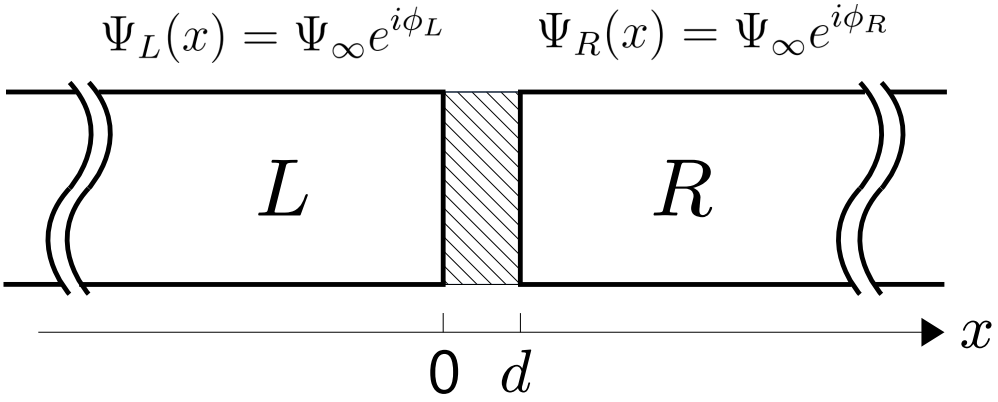

Fig. 1.3: Schematic illustration of a weak-link type Josephson Junction. Two bulk superconductors L and R are connected through the junction indicated by the dashed area with a width of d.

$$f(d) \;=\; a + bd = e^{i\Delta\phi}.$$

Then we obtain a normalized order parameter as

$$f = 1 + (e^{i\Delta\phi} - 1)\frac{x}{d} = (1 - \frac{x}{d}) + \frac{x}{d}e^{i\Delta\phi}. \tag{1.20}$$

This solution indicates that a superposition of penetrations of order parameters come from left and right sides of the bridge.

To develop the relationship between the phase difference $\Delta\phi$ and the current density J, we introduce a GL expression for current density as shown in Eq.(1.15). Because the vector potential is negligible, one dimensional current density is defined by

$$J(x) = \frac{e^*\hbar}{2m^*i}(\Psi^*(x)\frac{d}{dx}\Psi(x) - \Psi(x)\frac{d}{dx}\Psi^*(x)), \tag{1.21}$$

where $e^*$and m^* are charge and mass of carriers in superconductor, respectively. From Eq.(1.20), we know the form of the order parameter in the bridge $\Psi(x) = \Psi_\infty \times f$. Thus we obtain the current density as

$$\begin{aligned}
J(x) &= \frac{e^*\hbar}{2m^*i}|\Psi_\infty|^2\left[f^*\frac{df}{dx} - f\frac{df^*}{dx}\right] \\
&= \frac{e^*\hbar}{2m^*i}|\Psi_\infty|^2\left[(1 - \frac{x}{d} + \frac{x}{d}e^{-i\Delta\phi})(-\frac{1}{d} + \frac{1}{d}e^{i\Delta\phi}) - c.c.\right] \\
&= \frac{e^*\hbar}{m^*}|\Psi_\infty|^2\frac{1}{d}\frac{e^{i\Delta\phi} - e^{-i\Delta\phi}}{2i} \\
&= \frac{e^*\hbar}{dm^*}|\Psi_\infty|^2\sin(\Delta\phi).
\end{aligned} \tag{1.22}$$

Then an expression for the current through the junction is given by

$$I_s \;=\; I_0\sin(\Delta\phi), \tag{1.23}$$

where I_0 is a supercurrent amplitude of the junction. I_0 is given by

$$I_0 \;=\; \frac{e^*\hbar}{m^*}|\Psi_\infty|^2\frac{S}{d}, \tag{1.24}$$

where S is the cross-section area of the junction. Eq.(1.23) is known as DC Josephson effect in weakly linked superconductor junction [50, 51]. The supercurrent through the Josephson junction depends on the phase difference $\Delta\phi$ and does not depend on the voltage difference between the electrodes [45].

1.6.5 AC Josephson effect

The order parameter Ψ, which is introduced in Ginzburg-Landau theory, is considered as a pseudo-wave function to describe superconducting states. In the bridge structure as described in the previous section, we assume two order parameters for bulk superconductor L and R as

$$\Psi_L = \sqrt{n_L} e^{i\phi_L} \tag{1.25}$$

$$\Psi_R = \sqrt{n_R} e^{i\phi_R}, \tag{1.26}$$

where n_L and n_R are local densities of superconducting electron pairs in L and R, respectively. By using a very simple derivation due to Feynman [55], we discuss time dependences of the phase in Josephson junction. Through the bridge structure, these two order parameters satisfy

$$i\hbar \frac{\partial}{\partial t} \Psi_L = U_L \Psi_L + K \Psi_R \tag{1.27}$$

$$i\hbar \frac{\partial}{\partial t} \Psi_R = U_R \Psi_R + K \Psi_L, \tag{1.28}$$

where K describes characteristics of the junction and $U_{L,(R)}$ is the minimum energy of bulk superconductor L (R) [55]. In the case where K is zero, we obtain the ground states of the bulk superconductor L and R. In the case where the two superconductors are connected through the bridge, K is finite and there is an interaction between L and R due to penetration of the order parameter from one side to the other. The penetration is described by the amplitude K.

Consider the case where a voltage V is applied to the two superconductor L and R across the bridge, i.e. $U_L - U_R = q^* V$. By setting the energy at the middle point of the bridge to zero, Eqs. (1.27) and (1.28) are rewritten as

$$i\hbar \frac{\partial}{\partial t} \Psi_L = \frac{qV}{2} \Psi_L + K \Psi_R \tag{1.29}$$

$$i\hbar \frac{\partial}{\partial t} \Psi_R = -\frac{qV}{2} \Psi_R + K \Psi_L. \tag{1.30}$$

In order to separate the real and the imaginary parts, Eq. (1.25) is calculated by using Eqs.(1.29) and (1.30) as

$$i\hbar \frac{\partial}{\partial t} (\sqrt{n_L} e^{i\phi_L}) = \frac{q^* V}{2} \sqrt{n_L} e^{i\phi_L} + K \sqrt{n_R} e^{i\phi_R}$$

$$
\begin{aligned}
&i\hbar\left(\frac{1}{2\sqrt{n_L}}e^{i\phi_L}\dot{n}_L+\sqrt{n_L}ie^{i\phi_L}\dot{\phi}_L\right)=\frac{q^*V}{2}\sqrt{n_L}e^{i\phi_L}+K\sqrt{n_R}e^{i\phi_R}\\
&\frac{i\hbar}{2\sqrt{n_L}}\dot{n}_L-\hbar\sqrt{n_L}\dot{\phi}_L=\frac{q^*V}{2}\sqrt{n_L}+K\sqrt{n_R}e^{i\Delta\phi}\\
&i\left(\frac{\hbar}{2\sqrt{n_L}}\dot{n}_L-K\sqrt{n_R}\cos\Delta\phi\right)+\left(-\hbar\sqrt{n_L}\dot{\phi}_L-\frac{q^*V}{2}\sqrt{n_L}-K\sqrt{n_R}\sin\Delta\phi\right)=0.
\end{aligned}
$$

Eq. (1.26) may be calculated similarly. Finally we obtain the following four equations

$$
\begin{aligned}
\dot{n}_L &= +\frac{2}{\hbar}\sqrt{n_Ln_R}\sin\Delta\phi\\
\dot{n}_R &= -\frac{2}{\hbar}\sqrt{n_Ln_R}\sin\Delta\phi \qquad (1.31)\\
\dot{\phi}_L &= -\frac{K}{\hbar}\sqrt{\frac{n_R}{n_L}}\cos\Delta\phi-\frac{q^*V}{2\hbar}\\
\dot{\phi}_R &= -\frac{K}{\hbar}\sqrt{\frac{n_L}{n_R}}\cos\Delta\phi+\frac{q^*V}{2\hbar}. \qquad (1.32)
\end{aligned}
$$

By considering the geometrical symmetry of the bridge structure, we set the origin of the axis to the middle point of the bridge. The local density of the superconducting electron pairs satisfy $n_L = n_R = n_0$ at the positions where the distance from the origin is equal. Therefore $\sqrt{\frac{n_R}{n_L}} = \sqrt{\frac{n_L}{n_R}}$ is satisfied at the edges of the bridge ($x = 0, d$). From Eq. (1.32), the phase difference is given by

$$
\frac{d\Delta\phi}{dt}=\frac{q^*V}{\hbar}. \qquad (1.33)
$$

Eq. (1.33) describes time evolution of the phase difference $\Delta\phi$ at a finite voltage V across the bridge and is known as AC Josephson effect.

1.6.6 Phase difference in dc-SQUID

A dc-SQUID consists of two Josephson junctions which are connected in parallel. A schematic illustration of a dc-SQUID is shown in Fig. 1.4. Characteristics of phase differences in each Josephson junction are argued before discussing quantum interferences of superconducting current in a dc-SQUID [2].

From Eq.(1.16), the gradient of the phase $\nabla\phi$ is given by

$$\nabla\phi = \frac{m^*}{\hbar}\mathbf{v_s} + \frac{e^*}{\hbar}\mathbf{A}. \tag{1.34}$$

First, we consider an integration of $\nabla\phi$ along the superconducting loop. The integrals of Eq. (1.34) along the paths of integration b to a and a' to b', are given by

$$\int_b^a \nabla\phi d\mathbf{s} = \frac{m^*}{\hbar}\int_b^a \mathbf{v}_s d\mathbf{s} + \frac{e^*}{\hbar}\int_b^a \mathbf{A} d\mathbf{s} \tag{1.35}$$

$$\int_{a'}^{b'} \nabla\phi d\mathbf{s} = \frac{m^*}{\hbar}\int_{a'}^{b'} \mathbf{v}_s d\mathbf{s} + \frac{e^*}{\hbar}\int_{a'}^{b'} \mathbf{A} d\mathbf{s}. \tag{1.36}$$

By using a superconducting current density $\mathbf{j} = n^* m^* \mathbf{v}_s$ and $\lambda_L = \left(\frac{m^*}{\mu_0 n^* e^{*2}}\right)^{1/2}$, Eqs. (1.36) and (1.36) are rewritten as

$$\phi(a) - \phi(b) = \frac{2\pi}{\Phi_0}\mu_0\lambda_L^2\int_b^a \mathbf{j} d\mathbf{s} + \frac{2\pi}{\Phi_0}\int_b^a \mathbf{A} d\mathbf{s} \tag{1.37}$$

$$\phi(b') - \phi(a') = \frac{2\pi}{\Phi_0}\mu_0\lambda_L^2\int_{a'}^{b'} \mathbf{j} d\mathbf{s} + \frac{2\pi}{\Phi_0}\int_{a'}^{b'} \mathbf{A} d\mathbf{s}, \tag{1.38}$$

where λ_L is a London magnetic penetration depth [50]. and $\Phi_0 = \frac{h}{2e}$ is a flux quanta. Here we add $\frac{2\pi}{\Phi_0}\left(\int_{b'}^{b} \mathbf{A} d\mathbf{s} + \int_a^{a'} \mathbf{A} d\mathbf{s}\right)$ to both sides of Eqs. (1.37) and

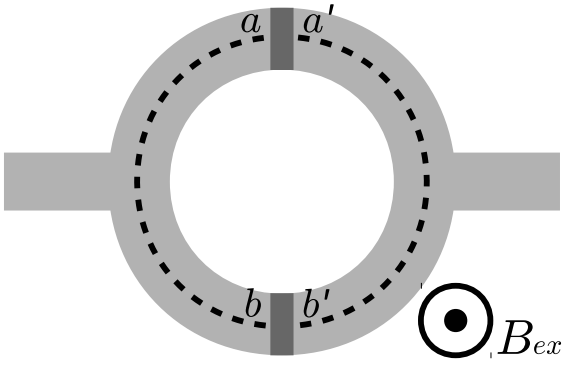

Fig. 1.4: A schematic illustration of a dc-SQUID with an applied external magnetic field B_{ex}. The dark gray areas indicate two Josephson junctions. The dashed line indicates the integration path as described in the text.

(1.38) and obtain

$$\left(\phi(b') - \phi(b) - \frac{2\pi}{\Phi_0}\int_b^{b'} \mathbf{A}d\mathbf{s}\right) - \left(\phi(a') - \phi(a) - \frac{2\pi}{\Phi_0}\int_a^{a'} \mathbf{A}d\mathbf{s}\right)$$
$$= \frac{2\pi}{\Phi_0}\mu_0\lambda_L^2\left(\int_b^a \mathbf{j}d\mathbf{s} + \int_{a'}^{b'} \mathbf{j}d\mathbf{s}\right) + \frac{2\pi}{\Phi_0}\oint_s \mathbf{A}d\mathbf{s}, \quad (1.39)$$

where the integration path s at the right hand side of Eq.(1.39) is the circumference of the superconducting loop. The integration of $\mathbf{A}$ along s equals to the magnetic flux $\Phi = A_{eff}B_{ex}$ penetrating the superconducting loop. Here A_{eff} is the effective area of the superconducting loop surrounded by the integration path s, and B_{ex} is the perpendicular component of the external magnetic field applied to the superconducting loop. A part of integrated current density in Eq.(1.39) corresponds to a self-flux induced by the circulating current I_s [2]. Eq. (1.39) is rewritten as

$$\delta(b) - \delta(a) = \frac{2\pi}{\Phi_0}\Phi_T, \quad (1.40)$$

where $\delta(a)$ and $\delta(b)$ are gauge-invariant phase differences of two Josephson junctions. A gauge-invariant phase difference δ is defined by

$$\delta = \Delta\phi - \frac{2\pi}{\Phi_0}\int \mathbf{A}d\mathbf{s}, \quad (1.41)$$

where the integration path is taken to be one side of the Josephson junctions from a to b. Φ_T in the left-hand side of Eq. (1.40) is the total magnetic flux and is given by $\Phi_T = B_{ex}A_{eff} + LI_s$ using the total inductance L [2, 50, 56]. According to Eq. (1.40), the phase difference varies with the magnetic field applied to the dc-SQUID.

1.6.7 A resistively and capacitively shunted junction model

As described in the previous section, a magnetic field is related to the phase difference at Josephson junctions by Eq. (1.40). The critical current I_c of a dc-SQUID is modulated by the magnetic field. In order to model the modulation of I_c with magnetic field, we introduce an equivalent circuit as shown in Fig. 1.5 based on a resistively and capacitively shunted junction

(RCSJ) model for a Josephson junction [2, 57, 58]. In the two Josephson junction A and B which are connected in parallel, the currents flow in A and B are defined by $i_a(t)$ and $i_b(t)$, respectively. The bias current I and the circulating current I_s of the SQUID are given by

$$I = i_a(t) + i_b(t) \tag{1.42}$$

$$I_s = \frac{i_b(t) - i_a(t)}{2}. \tag{1.43}$$

$i_a(t)$ and $i_b(t)$ depend on the resistance R, the capacitance C connected in parallel to the Josephson junctions, and the voltage applied to the junctions. i_a and i_b are given by

$$i_a(t) = I_a \sin\delta_a(t) + \frac{V_a}{R_a} + C_a\frac{dV_a}{dt} \tag{1.44}$$

$$i_b(t) = I_b \sin\delta_b(t) + \frac{V_b}{R_b} + C_b\frac{dV_b}{dt}. \tag{1.45}$$

where $I_{a(b)}$ is the current through the junction A (B), $R_{a(b)}$ is the shunt resistance, $C_{a(b)}$ is the shunt capacitance, $V_{a(b)}$ is the voltage, and $\delta_{a(b)}$ is the phase difference at the junction A (B).

From the AC Josephson effect, time evolution of the phase difference at

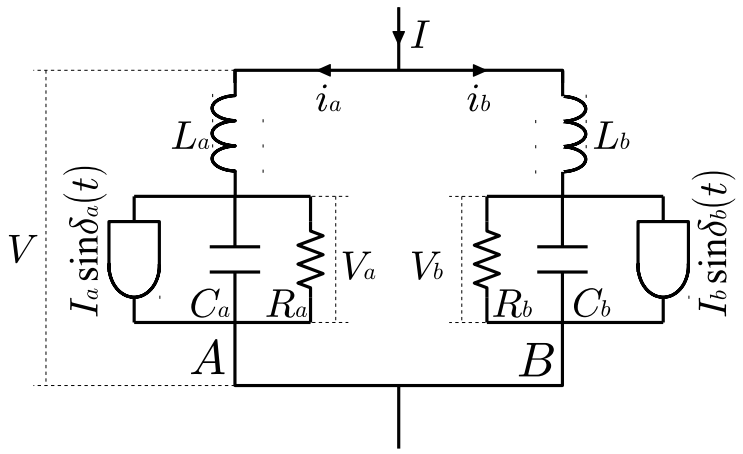

Fig. 1.5: An equivalent circuit of a dc-SQUID. Two Josephson junctions A and B are modeled by a resistively and capacitively shunted junction (RCSJ) model.

each junction is given by

$$\frac{d\delta_a(t)}{dt} = \frac{2e}{\hbar}V_a \tag{1.46}$$

$$\frac{d\delta_b(t)}{dt} = \frac{2e}{\hbar}V_b. \tag{1.47}$$

We assume that the inductance of each branch connected to the junction A and B satisfies $L_a = L_b = L/2$, where L is the self-inductance of the SQUID. We also assume that the mutual inductance is negligibly small. The total voltage V applied to the SQUID is given by using V_a and V_b as

$$V = V_a + \frac{L}{2}\frac{di_a(t)}{dt} \tag{1.48}$$

$$V = V_b + \frac{L}{2}\frac{di_b(t)}{dt}. \tag{1.49}$$

From Egs. (1.48) and (1.49), the total voltage $V(t)$ is given by

$$\begin{aligned} V(t) &= \frac{1}{2}\left(V_a + V_b + \frac{L}{2}\frac{d}{dt}(i_a + i_b)\right) \\ &= \frac{\hbar}{2e}\frac{d}{dt}\delta(t), \end{aligned} \tag{1.50}$$

where we assume that the bias current I is constant. The phase difference $\delta(t)$ is defined by $\delta(t) = (\delta_a + \delta_b)/2$. In the case where the currents through the junctions satisfy $I_a = I_b = I_0$, the bias current I is rewritten as

$$\begin{aligned} I &= I_0\left[\sin\delta_a(t) + \sin\delta_b(t)\right] + \frac{V_a + V_b}{R} \\ &= 2I_0 \sin\left(\frac{\delta_a + \delta_b}{2}\right)\cos\left(\frac{\delta_a - \delta_b}{2}\right) + \frac{2V(t)}{R} + 2C\frac{dV(t)}{dt} \\ &= I_c \sin\delta(t) + \frac{2V(t)}{R} + 2C\frac{dV(t)}{dt}. \end{aligned} \tag{1.51}$$

Here the critical current I_c is defined by using Eq. (1.40) as

$$I_c = 2I_0\left|\cos\left(\pi\frac{\Phi_T}{\Phi_0}\right)\right|. \tag{1.52}$$

In the case where the self-inductance L is negligible, $\Phi_T \approx \Phi_{ex}$ holds, where Φ_{ex} is a geometrical applied flux. From Eq. (1.52), the critical current of SQUID is a periodic function of Φ_{ex} with a period of flux quanta $\Phi_0 \cong 2.07 \times 10^{-15}$ Tm^2. Therefore, a SQUID can be used as a highly sensitive magnetic field detector.

1.6.8 On design of SQUIDs

In this section, we will review design guides for setting parameters in order to achieve an appropriate operation of a SQUID. The conditions for the parameters are introduced to avoid hysteresis in a current to voltage (IV) characteristics and a magnetic flux, and to avoid unwanted effects due to thermal fluctuations.

Hysteresis in current to voltage characteristics

According to the RCSJ model described in the previous section, we describe the IV characteristics of a single Josephson junction. From Eq.(1.44), a bias current i is rewritten as a function of a phase difference. i is given by using a dimensionless variable for time $\tau = \omega t \equiv \frac{2eI_0R}{\hbar}t$ as

$$\begin{aligned} \frac{i}{I_0} &= C\frac{\hbar}{2eI_0}\omega^2\frac{d^2\delta}{d\tau^2} + \frac{\hbar}{2eI_0R}\omega\frac{d\delta}{d\tau} + \sin\delta \\ &= \beta_c\frac{d^2\delta}{d\tau^2} + \frac{d\delta}{d\tau} + \sin\delta, \end{aligned} \tag{1.53}$$

where $\beta_c \equiv \omega CR = \frac{2eI_0CR^2}{\hbar}$ is a damping factor introduced by Mc Cumber [58] and Stewart [57] independently. The dynamics of Eq.(1.53) are qualitatively described by the dynamics of a particle experiencing a viscosity resistance in a tilted washboard potential [50, 51, 2]. The mass of the particle and the viscous force correspond to $\left(\frac{\hbar}{2e}\right)^2$ and $\left(\frac{\hbar}{2e}\right)^2\frac{1}{R}\frac{d\delta}{dt}$, respectively. The tilted washboard potential is given by

$$U(\delta) = -E_J\cos\delta - \frac{\hbar i}{2e}\delta, \tag{1.54}$$

where $E_J = \frac{\hbar I_0}{2e}$ is the binding energy of a Josephson junction. The particle may move along δ-axis in the potential. Fig. 1.6 shows schematic illustrations of the tilted washboard potential.

We consider the dynamics of a particle at $T = 0$ for simplicity. In the case of $i < I_0$, the particle may stay in a local minimum of the potential and a kinetic energy is described by $\frac{1}{2}m\left(\frac{d\delta}{dt}\right)^2 = \frac{1}{2}CV^2 = 0$. Because the voltage V is zero, it is a zero voltage state. On the other hand, in the case of $i > I_0$, the particle may move along the potential slope. An averaged voltage V related with the kinetic energy may become proportional to the bias current i, and

hence the IV relation obeys Ohm's law. Here, note that whether the IV characteristics exhibit hysteresis or not depends on the values of the inertia moment and the viscous force. We consider the case where a particle starts to move at $i = I_0$ with increase in the bias current and then is trapped at a local minimum at $i = I_r$ by decreasing the bias current. In the case of a large inertia moment and a small viscous force, I_r may be different from I_0. This hysteretic behavior of IV characteristics is characterized by a damping factor β_c. When the damping factor β_c satisfies

$$\beta_c = \frac{\pi I_0 C R^2}{\Phi_0} \leq 1, \tag{1.55}$$

a hysteresis in the IV characteristics can be avoided [50, 58]. This is called an over damping state of a SQUID.

In the case of $\beta_c \ll 1$, Eq. (1.53) is rewritten by

$$\frac{d\delta}{dt} = \frac{2eI_0R}{\hbar}\left(\frac{i}{I_0} - \sin\delta\right). \tag{1.56}$$

By averaging the voltage over a period of δ, a time averaged voltage is given

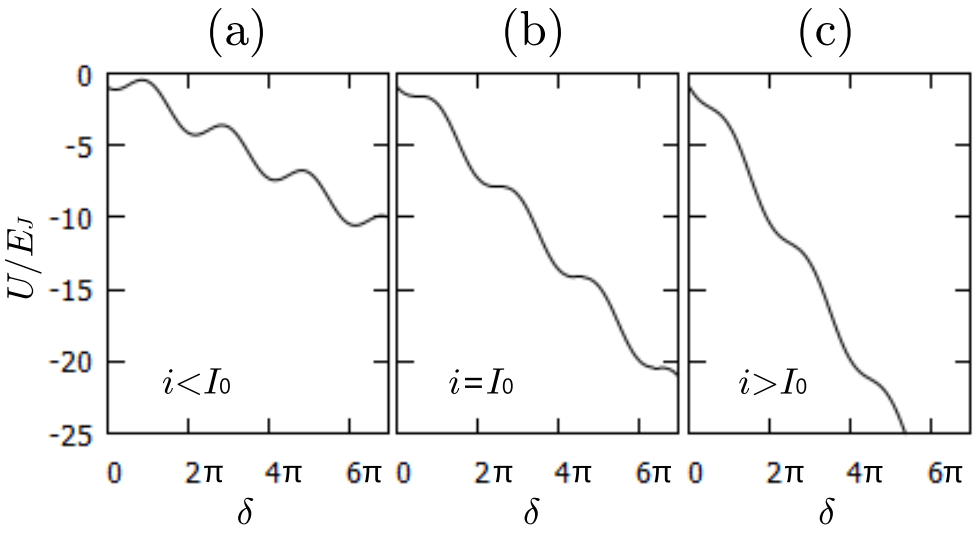

Fig. 1.6: Schematic illustrations of a tilted washboard potential for $i < I_0$ (a), $i = I_0$ (b) and $i > I_0$ (c). A vertical axis is normalized by a binding energy of Josephson junction.

by

$$V = R(i^2 - I_0^2)^{1/2}. \tag{1.57}$$

The zero voltage state at $i < I_0$ and an Ohmic state at $i \gg I_0$ are connected smoothly through Eq. (1.57).

In the case where two Josephson junctions connected in parallel exhibit identical magnetic response of a critical current as in Eq. (1.52), we may apply the previous discussions to a dc-SQUID [50]. In a weak-link type dc-SQUID, Eq. (1.55) is safely satisfied because the capacitance is usually negligibly small.

Hysteresis in magnetic flux

We consider the condition for a self-inductance L, which is mainly determined by the geometric design of a SQUID. The total flux Φ_T is a sum of an external magnetic flux Φ_{ex} and a self magnetic flux $\Phi_s = LI_s$ induced by a circulating current I_s as indicated in Eq. (1.43). We ignore the effects due to resistance and capacitance for simplicity. From Eqs. (1.44) and (1.45), a bias current I and a circulating current I_s are given by

$$I = I_0(\sin\delta_a + \sin\delta_b) \tag{1.58}$$

$$I_s = \frac{I_0}{2}(\sin\delta_b - \sin\delta_a). \tag{1.59}$$

In the case of $I \approx 0$, the phase difference satisfies $\delta_a \approx -\delta_b$. Therefore the circulating current I_s is rewritten by using Eq. (1.40) as

$$I_s = -I_0 \sin\left(\frac{\pi\Phi_T}{\Phi_0}\right). \tag{1.60}$$

From Eq. (1.60), the external magnetic flux is given by

$$\Phi_{ex} = \Phi_T + LI_0 \sin\left(\frac{\pi\Phi_T}{\Phi_0}\right). \tag{1.61}$$

By using Eq. (1.61), Φ_T can be expressed as a function of Φ_{ex}. In the case of $\beta_m \equiv \frac{2LI_0}{\Phi_0} \leq \frac{2}{\pi}$, where β_m is a magnetic shielding factor of a SQUID, Φ_T becomes a single-valued function of Φ_{ex}, and hence there is no hysteresis in a $\Phi_T - \Phi_{ex}$ relation. Computer simulations [9] showed that a magnetic

flux sensitivity is optimized when β_c takes a value just below the onset of hysteresis and $\beta_m = 1$. Therefore a condition for self-inductance L is given by

$$\beta_m \equiv \frac{2LI_0}{\Phi_0} \leq \frac{2}{\pi} \approx 1. \tag{1.62}$$

Thermal fluctuations

In order to keep phase coherences in Josephson junctions, phase fluctuation in the junctions must be smaller than the binding energy E_J. From computer simulations [59], quantitative condition is given by

$$E_J = \frac{\hbar I_0}{2e} \geq 5kT, \tag{1.63}$$

where k is a Boltzmann coefficient.

On the other hand, by considering the effect due to thermal fluctuations in the magnetic flux, a condition for the self-inductance L is given as follows. According to the principle of equipartition of energy in statistical mechanics, a mean-square noise of a magnetic flux in a loop with self-inductance L is given by $< \Phi_N^2 >^{1/2} = (kTL)^{1/2}$. If $< \Phi_N^2 >^{1/2}$ is greater than a period of the magnetic flux $\Phi_0/2$, a periodic response of a SQUID may be smeared out by magnetic flux noise. Then a condition for the self-inductance is given by

$$L \leq \frac{\Phi_0^2}{4kT}. \tag{1.64}$$

Limit of a magnetic flux sensitivity

We consider the case where a SQUID is operated as a magnetic flux to voltage transducer. The time-averaged voltage of a SQUID at a constant bias current is given using Eq. (1.56) as

$$V = \frac{R}{2}\left[I^2 - \left(2I_0 \cos\left(\frac{\pi\Phi}{\Phi_0}\right)\right)^2\right]^{1/2}. \tag{1.65}$$

The transform coefficient of magnetic flux to voltage at a bias current I is given by $V_\Phi \equiv |(\partial V/\partial\Phi)_I|$. In the case of Eq. (1.65), the maximum transform efficiency is $V_\Phi = 2I_0R/\Phi_0$. The condition Eq. (1.62) is rewritten as $V_\Phi \leq R/L$.

The magnetic flux resolution of a SQUID is given by the equivalent magnetic flux noise level with a spectrum density $S_\Phi(f)$ at a frequency f. By using the transform coefficient of magnetic flux to voltage $V_\Phi = 2I_0R/\Phi_0$ and the voltage noise spectrum density $S_V(f) = 4kTR$ due to the Johnson noise, $S_\Phi(f)$ is given by

$$S_\Phi(f) = S_V(f)/V_\Phi \approx 4kTL^2/R. \tag{1.66}$$

The magnetic flux noise spectrum density in Eq.(1.66) is rewritten as the energy spectrum density by [9]

$$\epsilon(f) = S_\Phi(f)/2L \approx 2kTL/R. \tag{1.67}$$

This indicates that the magnetic flux sensitivity is improved by reducing the self-inductance L through miniaturization of the SQUID loop.

1.7 Organization of this thesis

The remainder of this thesis is organized as follows. In Chapter 2, I describe on the development of weak-link Nb-based nano-SQUID probes and a newly developed scanning measurement system that can be operated at low temperature. I also describe on targeted samples of GaAs/Al_xGa_{1-x}As modulation-doped single heterojunction and tungsten carbide films prepared by focused ion-beam (FIB) induced deposition.

Characterizations of our weak-link Nb-based scanning nano-SQUID microscope system are described in Chapter 3. Characterizations of nano-SQUID probes are examined.

In Chapter 4, I describe on measurements of magnetic flux induced by current density in two-dimensional electron system. I also describe details of the reconstruction method of two-dimensional current densities from the measured magnetic flux distributions.

In Chapter 5, I describe on measurements of tungsten carbide thin films and wires prepared by FIB induced deposition to investigate superconducting properties of tungsten carbide samples. Meissner effect and current density distribution in tungsten carbide samples are studied.

Concluding remarks are described in Chapter 6. In this thesis, weak-link Nb-based scanning nano-SQUID microscope is shown to be a powerful tool for investigations of magnetic flux induced by current in two-dimensional electron systems, and Meissner effect and current distribution in tungsten carbide thin films.

Chapter 2

Experimental

2.1 Fabrication procedures of SQUID probes

2.1.1 A laser-lithography and a deep pulsed reactive ion etching

We used a silicon (100) substrate with thickness of 100 μm. The size of our nano-SQUID probes was 2 mm$\times$0.6 mm. Fig. 2.1 shows a typical structure pattern of nano-SQUID probe. We used a Nb/Au thin film as superconducting layer. The Au film was prepared as a protective layer during the FIB milling. The Au film was also served as a parallel shunt resistor and a heat sink to reduce the effects of Joule heating. We use Bosch process and FIB milling process to prepare the weak-link type nano-SQUID probes positioned near the probe edge.

Lithography for superconducting electrode

First we employ a bilayer lithography for preparing superconducting four terminal electrodes on a 100 μm-thick silicon substrate. A slit was prepared near the edge of nano-SQUID probes as shown in Fig. 2.1 by the laser lithography. The milling time of FIB process was significantly reduced by this slit. Also there are several small patterns near the SQUID that assist the alignment process before FIB milling.

First, as a bottom resist, MGI-SF3 was spin-coated at 3000 rpm for 60 s and baked in 180 °C for 5 minutes. Subsequently, AZ5214E, as a top resist, was spin-coated at 3000 rpm for 60 s and baked in 110 °C for 2 minutes.

We use a laser-lithography system (DL-1000, Nano-System Solutions, Inc). This laser-lithography system is a maskless lithography system and is useful for improvements of electrode patterns and process conditions at a short turn-around time. In the system, positioning and superposition accuracy was about 1 μm. In our experiment, exposed dose was 140 mJ/cm^2 using a 405 nm-semiconductor laser diode. Developer was tetramethylammonium hydroxide (TMAH) with dilution rate 2.38%.

Deposition of superconducting film

We used a rf-sputtering system for depositing 23 nm thick niobium superconducting film. Base pressure was typically 1.0×10^{-5} Pa and the pressure during sputtering was about 1.3×10^{-1} Pa. The RF power was 100 W and the deposition rate of niobium film was 0.2 nm/s. Without breaking vacuum, a gold film with thickness of 70 nm was prepared by an electron-beam deposition at the rate of 0.1 nm/s. After preparing a Nb/Au (23 nm/70 nm) film, the electrode patterns were lifted off in N-methylpyrrolidone (NMP) at 80 °C for 40 minutes.

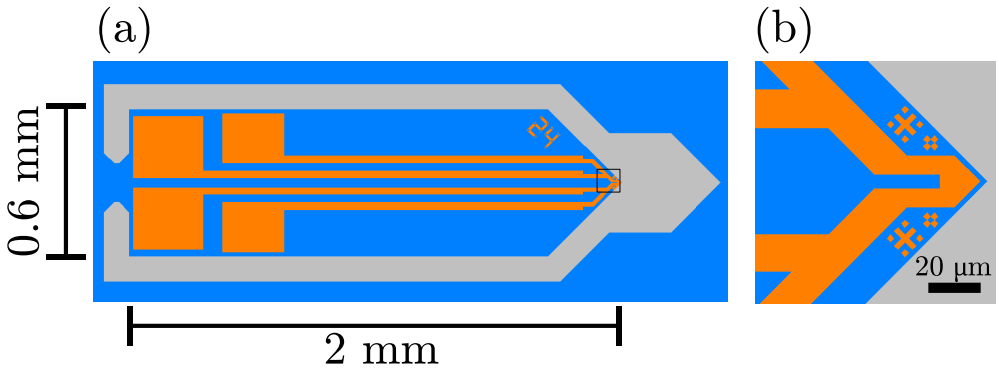

Fig. 2.1: Schematics of a typical structure pattern of nano-SQUID probe. (a) and (b) indicate a whole pattern and a magnified image of the probe tip, respectively. The orange indicates pattern for Nb/Au film deposition, and the gray indicates pattern for a deep pulsed reactive ion etching.

Deep silicon etching

Next, we used a AZ-P4620 for deep silicon etching process hereafter called Bosch process. Deep silicon etching area is indicated by gray pattern in Fig. 2.1. By using a viscous resist of AZ-P4620, a film with thickness of 5 μm was prepared by spin-coating at 5000 rpm. This thick resist prevented the sample surface from unintentional etching during reactive ion etching (RIE) process. Bosch process is a variant of the RIE process. The main difference between Bosch and other RIE processes is repeating procedure of etching and passivation of lateral side. We used a MUC-21 manufactured by Sumitomo Precision Products. We used SF_6 and C_4F_8 for reactive etching process and passivation process, respectively. After 200 cycles of etching and passivation, silicon substrate with thickness of 100 μm was completely etched. Probes with high aspect ratio was formed.

After Bosch process, an O_2 plasma cleaning process was done to remove hardened AZ-P4620 resist due to heating and passivation procedures. This cleaning is required for removal of AZ-P4620 resist using NMP. Several dozens of probes were fabricated at single cycle of fabrication process.

2.1.2 Mechanical polishing at the apex of a probe tip

In the fabrication process, during silicon deep etching, there was an unavoidable degradation of niobium superconductor film placed around a probe substrate edge, Thus we developed a mechanical polishing process for SQUID probe to remove the deteriorated niobium area.

Polishing slurry

First, we prepared a polishing slurry (abrading agent diluted with some solvent). Almost all commercially available slurries contain water and several chemical compounds in their solution. In order to prevent unnecessary exposure of a niobium film to water, we prepared slurry with aluminum oxide nano-particles as abrading agent and n-octanol $C_8H_{18}O$ as solvent. Because the degradation area was several micrometer from the probe substrate edge, precise polishing with sub-micrometer range were needed. We selected high purity alumina particle TM-DAR (Taimei Chemicals Co.,Ltd.) with average particle diameter of 100 nm. A low volatile solvent was necessary for a concentration control of slurry during polishing. An n-octanol is a low volatile alcohol which is easily removed by washing with isopropanol. After blending n-octanol and TM-DAR with a mass ratio of 2 to 1, the slurry were agitated by ultrasonic dispersion for about 1 hour.

Fixing jig

In order to obtain a constant load and fixed angle during polishing, we used a fixing jig as shown in Fig. 2.2(a). A long support rod achieved a constant load polishing utilizing see-saw mechanism. Typical value of a loading was 0.4 g which was measured by digital weighing machine. Because several heavy supersonic washing processes for the probe substrates were needed to remove the slurry, we fixed the substrate by gluing to a brass rod with two-component epoxy adhesive as shown in Fig. 2.2(b). By heating the brass rod to 80 C°, we could remove the adhesive.

Mechanical polishing process

Utilizing the fixing jig with a slide glass, we polished the probe substrate manually. After putting a few drop of slurry on a slide glass, the probe substrate was mounted on the drop. The slide glass was slowly moved in

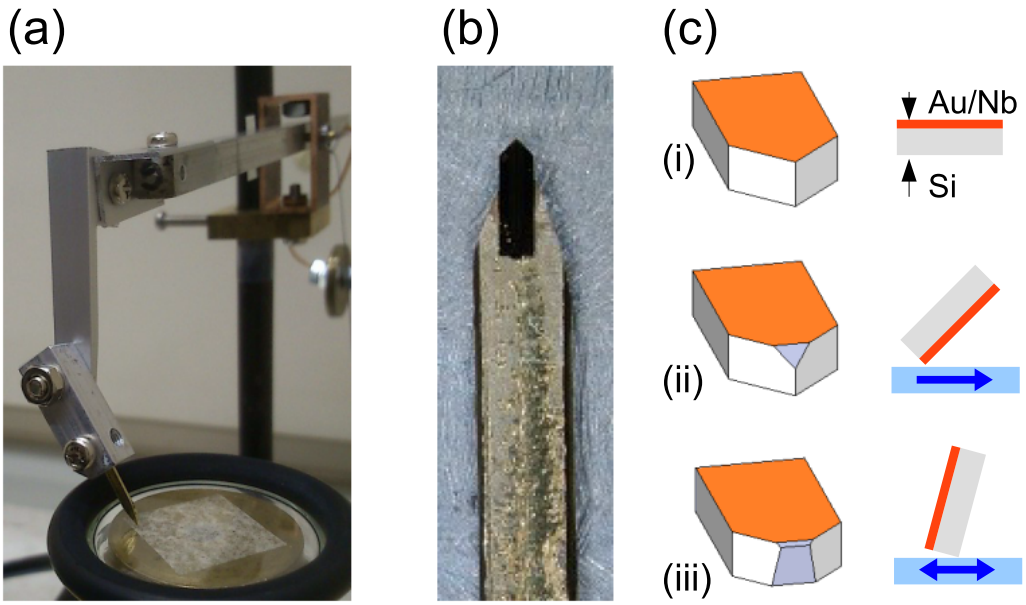

Fig. 2.2: A photographic image of a fixing jig for polishing (a) and a fixed substrate to a brass needle(b). (c) Schematic image of polishing process. At first a bare probe substrate (i) was polished to remove the degradation area of Au/Nb film (ii). A residual substrate edge was polished from the bottom (iii). Right hand pictures indicate side views of polishing and polishing directions (blue arrow).

certain direction. Schematic illustrations of typical polishing process are shown in Fig. 2.2(c). At first we removed the degradation area by polishing from the topside of probe (ii). In this time, to prevent from unexpected residual film, one way polishing was applied as shown in the right panel. A blue arrow indicates the polishing direction. A polishing angle and a sliding length of the glass was 45° and less than 30 mm respectively. This short polishing length was enough to remove the degradation film which touched to the glass surface directly. After supersonic washing in isopropanol for 10 minutes, we checked polished area by optical microscope at 1000-fold magnification. For second process, an otiose part of the probe substrate was polished from bottom side(iii). During the tilted polishing, we found that a polishing rate was changing caused by widening area where touched to the glass slide. From a test polishing, we obtained a rough indication for

polishing rate which was quite empirical. Thus we had to check a remaining substrate length by optical microscope frequently.

Optical image of a test polishing are shown in Fig. 2.3(a) and (b). In this test, a round trip polishing from bottom side were applied with angle of 70° as shown in the inset of Fig. 2.3(b). We found that an unexpected residual film (red arrow) turned outward. In order to avoid the residual film, several types of polishing were tried. As already mentioned, one of a solution was one way polishing from topside.

Fig. 2.3(c) shows a optical image of polished surface. We can see a flat surface on left side in a silicon substrate with a width of 100 μm. In Fig. 2.3(d) we show a magnified view indicated black rectangular in (c). We can see many horizontal lines which were produced by repetition Bosch procedure of reactive ion etching and passivation. Comparing with the surface from Bosch process, mechanically polished surface is sufficiently flat. On the other hand, we should mention that the optimal condition of our slurry changed with time. A long time polishing, typically over 20 minutes, made a rough surface caused by a concentration change of the slurry. Thus we frequently changed the slurry to achieve a flat surface polishing.

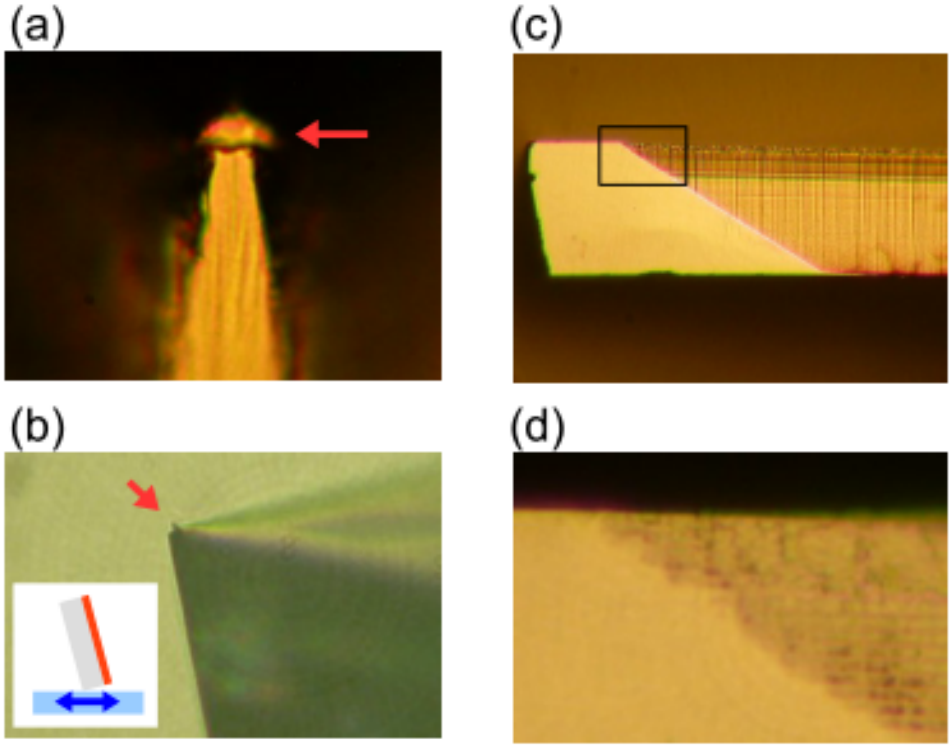

Fig. 2.3: An photographic image from top side of the tentatively polished probe edge (a) and a perspective (b). Inset shows a schematic illustration of polishing configuration from bottom side. Red arrows indicates a residual film which was turned outward. A photographic image of polished flat surface and a magnified view are shown in (c) and (d) respectively. Horizontal lines in (c) was produced by Bosch process.

2.1.3 Resistance-temperature characteristics of Nb films

R-T characteristic of our SQUID probe was evaluated by PPMS (Quantum Design, Inc.). First, we measured *R-T* characteristic of a probe before FIB milling. Second, *R-T* measurement was done after forming a slit as shown in Fig. 2.5 (b) and (e). After this milling, a small region of superconducting film was left near the substrate edge. Thus superconductivity of Nb/Au thin film positioned close to the probe top was characterized. Fig. 2.4 indicates FIB milling fabrication steps in two probe samples with different length of slit near the sample edge. Fig. 2.5 shows correspondent *R-T* characteristics of the probes in Fig. 2.4. These two probe samples were fabricated on the same substrate by single cycle of fabrication process. The *R-T* characteristics indicates the critical temperature (T_c) of 6.1 K. After FIB milling, T_c of the probe with the deeper slit in Fig. 2.4(b) fell off to 5.6 K, while T_c of the probe with shallower slit was 6.1 K. This result suggests that the degradation of superconductivity of Nb/Au film by the Bosch and O_2 cleaning process was located in the region about 2.2 μm from the edge of Nb/Au film.

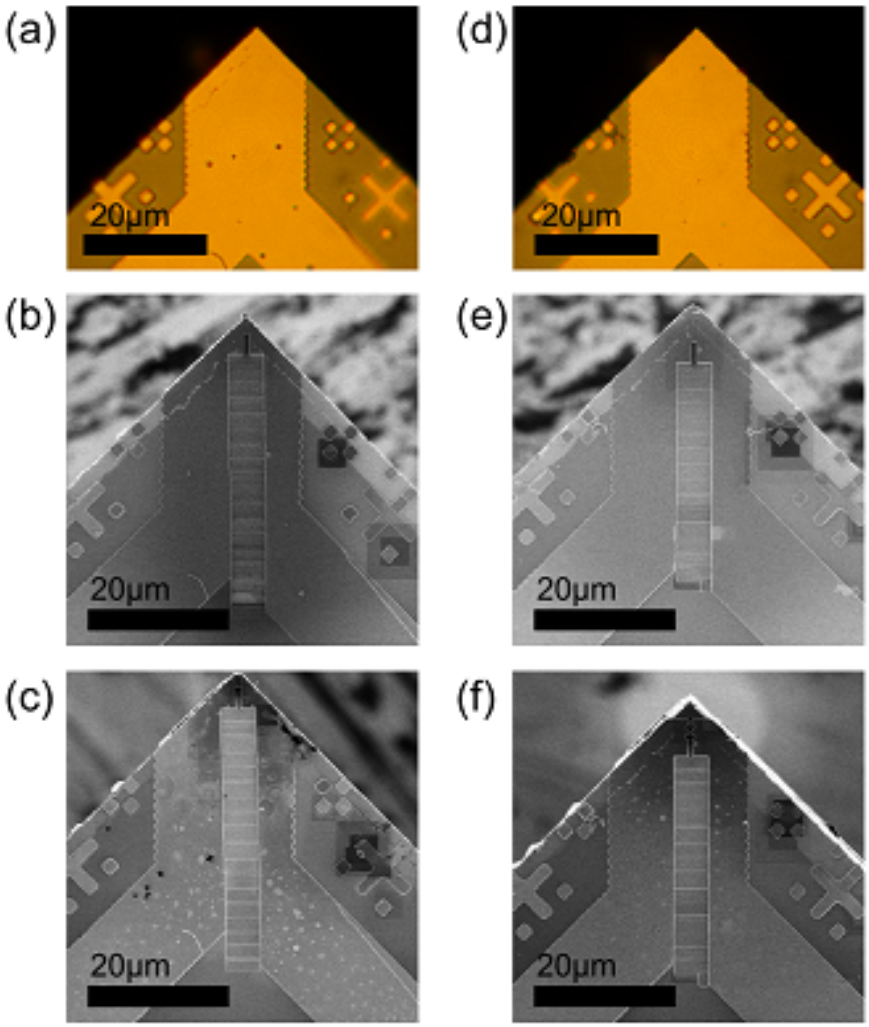

Fig. 2.4: Optical microscope images of two probes at each stage of SQUID fabrication. Left panels (a), (b), and (c) show deeper slit than the right panels (d), (e), and (f). (a) and (d) show optical micrographs of scanning probes, which were fabricated at single cycle of fabrication process on the same Si substrate. (b) and (e) show scanning ion microscope (SIM) images after slit formation by FIB milling. The widths of the remaining Nb/Au film at the tip in (b) and (e) were 2.2 μm and 5.5 μm, respectively. (c) and (d) show typical SIM images after SQUID fabrication.

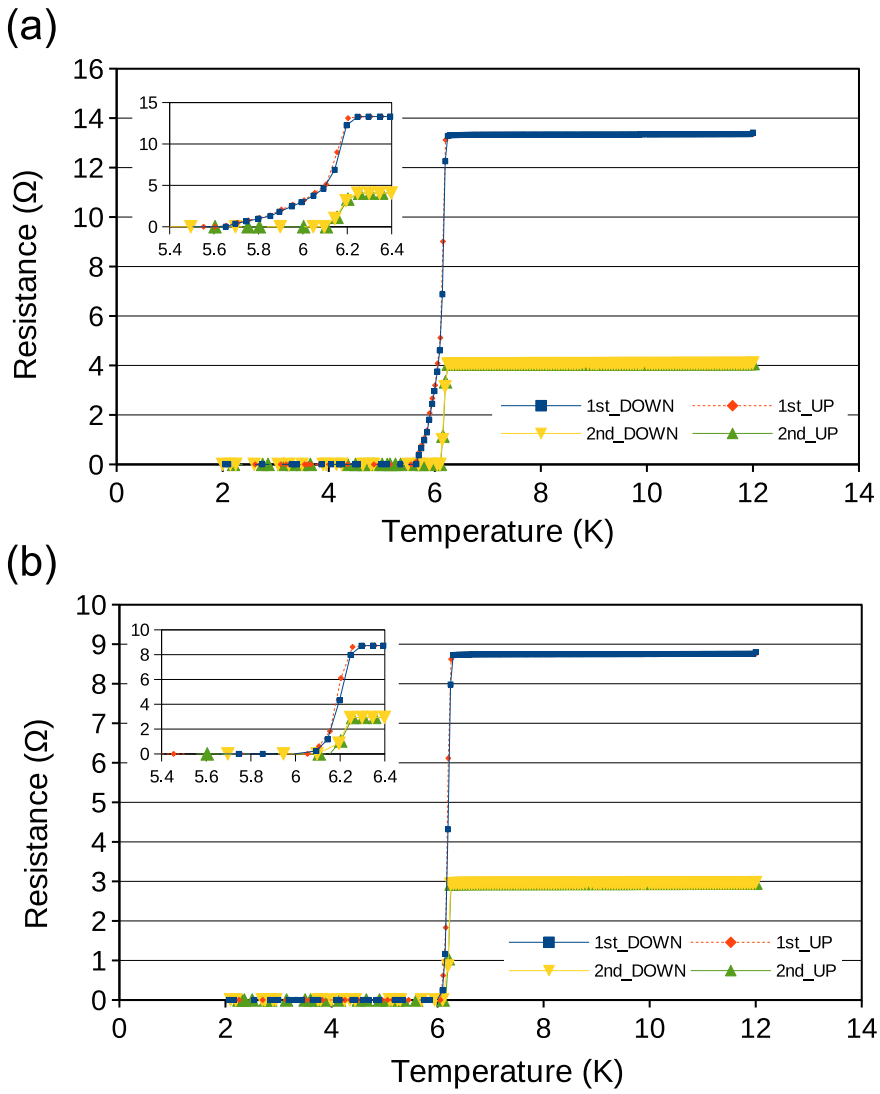

Fig. 2.5: (a) *R-T* characteristics of the probe displayed in the left panel of Fig. 2.4. "1st" and "2nd" indicate before and after formation the slit, respectively. "DOWN" and "UP" indicate sweep directions of temperature. (b) *R-T* characteristics of the probe in the right panel of Fig. 2.4. The critical temperature of the nano-SQUID probe was 6.1 K.

2.1.4 Fabrication of SQUIDs by FIB process

Before FIB process, we attached a nano-SQUID probe to a quartz tuning fork (TF) as described in next chapter. A nano-SQUID probe was glued to a side of a TF by two-component epoxy adhesive. Superconducting four terminal electrodes were connected to external circuit with aluminum thin wires by wedge bonding.

Finally, weak-link type dc-nano-SQUIDs were fabricated by FIB milling similar to the method in the literature [13]. The superconducting loop and weak-link junctions were milled by the FIB process with typical beam voltage and current of 31 kV and 5 pA, respectively. The SQUID loop with the size of 1 μm was located within 4.8 μm from the tip of the Si probe. The dimensions of the SQUID loop and the weak-link width were 1.0 μm and 80 nm, respectively. Figs. 2.6 (a) and (b) show scanning ion microscope images of SQUID probes without mechanical polishing and after mechanical polishing of the tip of the probe. The geometrical inductance $L = 5\mu_0 C/16$, where C is the inner circumference of the SQUID [46] was 1.6 pH. The effect of the self-induced field as given by $\beta_m = 2LI_c/\Phi_0$ was 0.32.

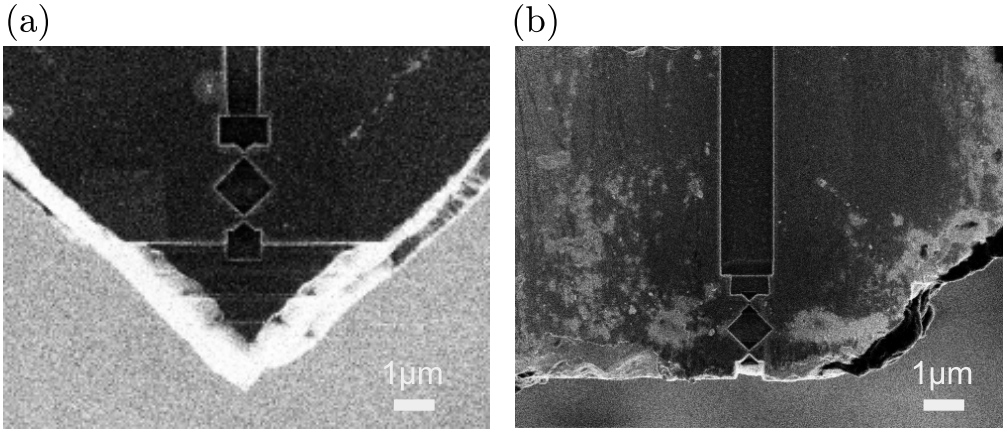

Fig. 2.6: (a) Scanning ion microscope images of SQUID probes without mechanical polishing and (b) after mechanical polishing of the tip of the probe. SQUID loop and weak link junctions were fabricated by an FIB milling system.

2.2 Measurement apparatus for nano-SQUIDs

At first we describe our measurement system for current to voltage ($I-V$)characteristics of a nano-SQUID in the temperature range of ^{4}He cryogen-free refrigerator. Before measuring $I-V$ curves, the sample stage was separated from the SQUID probe. A nano-SQUID was current biased through a 3780 Ω-bias resistor. We used a function generator (DF1906, NF Corporation) as a voltage source in Fig. 2.7. Voltage shift of the SQUID $V_{\rm sq}$ was amplified using a differential preamplifier located at room temperature. The gain of the differential amplifier was typically 500. We applied a continuous triangular wave current at the frequency of 0.1 Hz to the SQUID probe and measured $V_{\rm sq}$ with a digital multimeter (34401A, Agilent) at the interval of 10 ms. After measurements for 10 s, we obtained a current-voltage curve corresponding to a cycle of the applied triangular wave. This method was used to obtain current-voltage curves in the external field $B_{\rm ex}$.

In our nano-SQUID, I-V characteristics near the superconducting transition was rounded and no hysteresis was observed as shown in Fig. 2.8. Thus we could use a lock-in detection for SQUID voltage measurement under a constant current bias I_{sq}. Fig. 2.7 shows a typical setup for ac flux distribution measurement induced by ac current flowing in a Hall-bar sample. A programmable dc voltage source (GS200, Yokogawa) was used as a constant voltage source in Fig. 2.7. During ac current was applied to Hall-bar sample, the ac magnetic field was detected as SQUID voltage change with high signal-noise ratio using a lock-in amplifier (LI5640, NF Corporation) at synchronizing frequency was 1873 Hz. A bias resistor for Hall-bar sample was 10 and 100 kΩ for applied current of 70 μA and 2.8 μA, respectively.

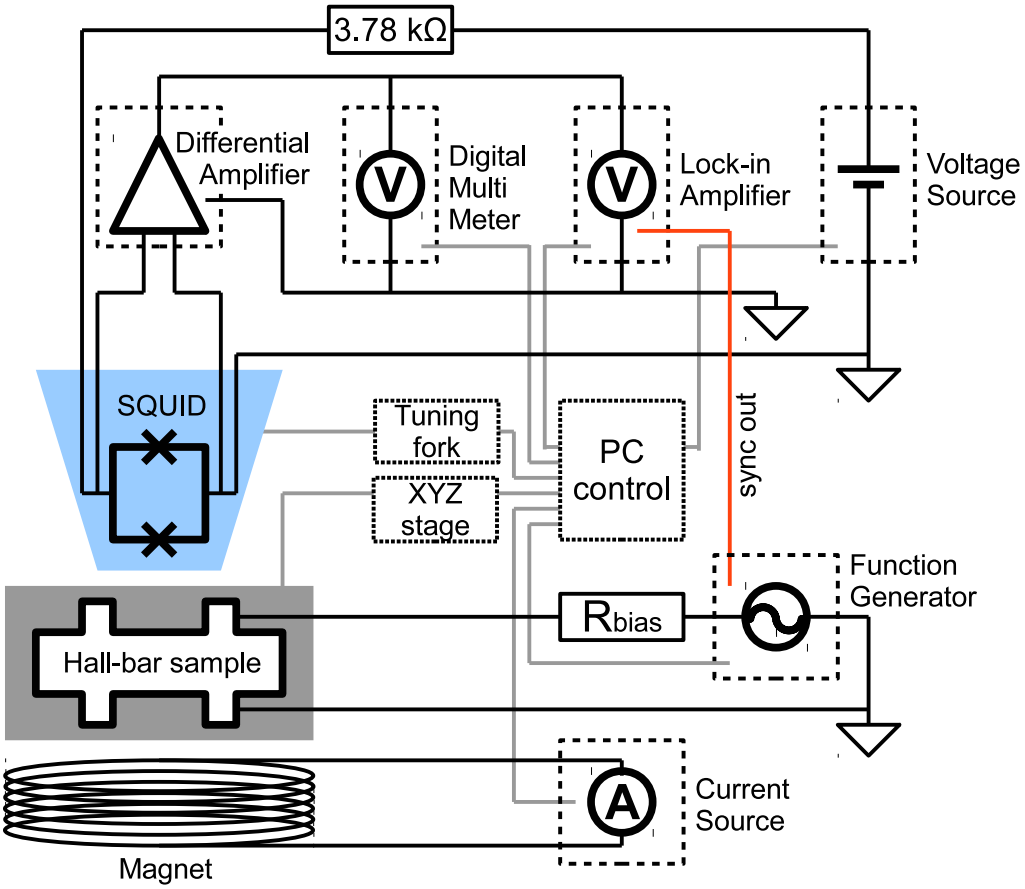

Fig. 2.7: Schematics of setup for ac flux distribution measurement induced by ac current flowing in a sample. Black lines and gray lines show a primary circuits and control connections, respectively. Constant current bias I_{sq} is applied to the SQUID probe by a voltage source V_{in} through a bias resistor of 3.78 kΩ. The output voltage signal from the SQUID V_{sq} is amplified at room temperature by a differential preamplifier, and is detected using a digital multimeter and a lock-in amplifier synchronously at $f = 1873$ Hz. The synchronizing frequency is the same with sinusoidal current frequency in Hall-bar sample applied by a function generator.

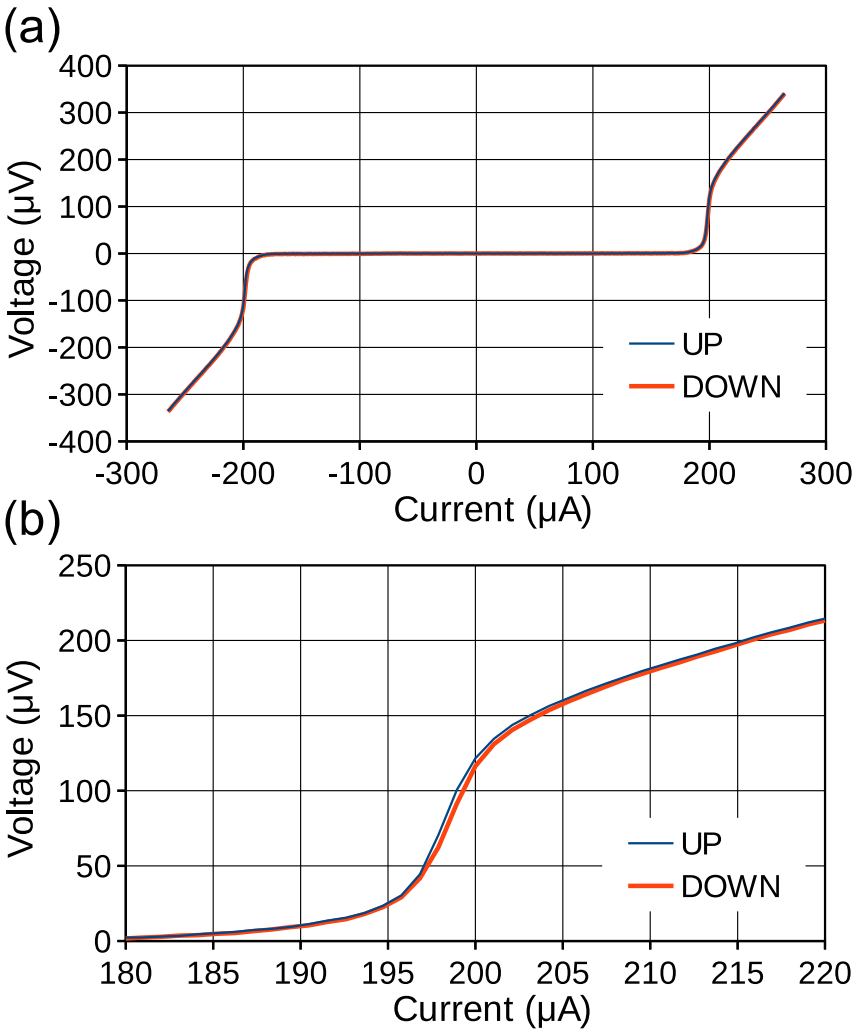

Fig. 2.8: (a) Typical current voltage characteristics of SQUID probe at 3.6 K without external magnetic field. Current bias was swept by a triangular wave at the frequency 0.1 Hz. Blue and orange curves indicate upward and downward current sweep direction, respectively. (b) The sample plot as (a) but for the current between 180 and 220 μA. The observed hysteresis was small.

2.3 Scanning system in a ^{4}He cryogen-free refrigerator

We constructed a scanning nano-SQUID microscope system in a ^{4}He cryogen-free refrigerator. In this section, we describe several components which are used for scanning measurements. We will describe the evaluations of our system in Chapter 3.

Cryogenic environment

A ^{4}He cryogen-free refrigerator is a closed-cycle refrigerating system that can maintain a cryogenic environment without liquid ^{4}He. A cryogenic stage, called 4 K-plate, was large enough to accommodate a scanning stage, a superconducting magnet and thermal anchors for electrical measurement wires. The base temperature was measured by a calibrated celnox thermometer to be 3.6 K. The temperature was controlled by a temperature controller (Model 340, Lake Shore) using a heater on the 4 K plate. We also introduced a thermometer and a ceramic heater on the scanning stage. A home-made NbTi solenoidal superconducting magnet was introduced on the 4 K-plate and was connected to an external current source.

Scanning stage

A schematic illustration of our scanning nano-SQUID system in ^{4}He cryogen-free pulse-tube refrigerator is shown in Fig. 3.1 (a). A nano-SQUID probe was attached to a quartz tuning fork. A sample stage was placed on a triaxial piezoelectric inertial stages described below. The SQUID probe and the piezoelectric inertial stages were housed in a stainless cage. In order to decrease vibrations from the compressor, the cage was connected to the 4 K plate of the cryostat with four springs. A sample stage and the 4 K plate were thermally connected by a bundle of copper wires.

Piezo triaxial inertial stages

We used a triaxial piezoelectric inertial stage with resistive position encoders(ANPx101/RES and ANPz101/RESs, Attocube systems). The range of travel and coarse positioning accuracy were 5 mm and 100 nm, respectively, at 4 K. The repeatability of the resistive position encoders were estimated

to be about 200 nm at 3.4 K. The stainless housing was placed in the bore of a home-made superconducting magnet with the bore size of 50 mm.

Quartz tuning fork for tip-sample distance control

For scanning probe measurements, control of the distance between probe tip and the sample surface is important, and a variety of techniques has been developed. We have constructed a setup to precisely control the tip-sample distance using a quartz tuning fork in cryogenic temperatures. [60] By using a functional generator (DF1906, NF Corporation), we applied a sinusoidal voltage with typical amplitude of 20 mV and detected the displacement current by a lock-in amplifier . To achieve high signal-noise ratio, coaxial cables with impedance matched connections were used.

Chapter 3

Evaluation of scanning SQUID microscope system

3.1 A scanning operation system in ^{4}He cryogen-free refrigerator

In general, scanning probe microscopes (SPMs) utilized height feed back technique. The optical lever technique is widely used at room temperature operation. However, optical system is often incompatible with measurements at low temperatures. In near-field optical microscopy, a quartz tuning fork has been utilized as a non-optical height feedback sensor. It can be applied for scanning measurement in dilution refrigerator system [61, 62].

We used a commercially available quartz tuning fork as a height feed back sensor in ^{4}He cryogen-free refrigerator. A cooling time and a typical base temperature of our system were 20 hours and 3.6 K. The large space on the 4 K stage and rapid cooling repetition rate enables us to improve the system configuration at a short cycle.

Fig. 3.1(a) shows a schematic illustration of scanning nano-SQUID system in a cryogen-free ^{4}He refrigerator. A triaxial piezoelectric inertial stage was placed in a stainless cage. Sample was fixed on the stage by a copper block. A nano-SQUID probe was attached to the quartz tuning fork above the sample surface. From optical micrographs, the angle between the sensor surface and the sample stage was estimated to be 51°.

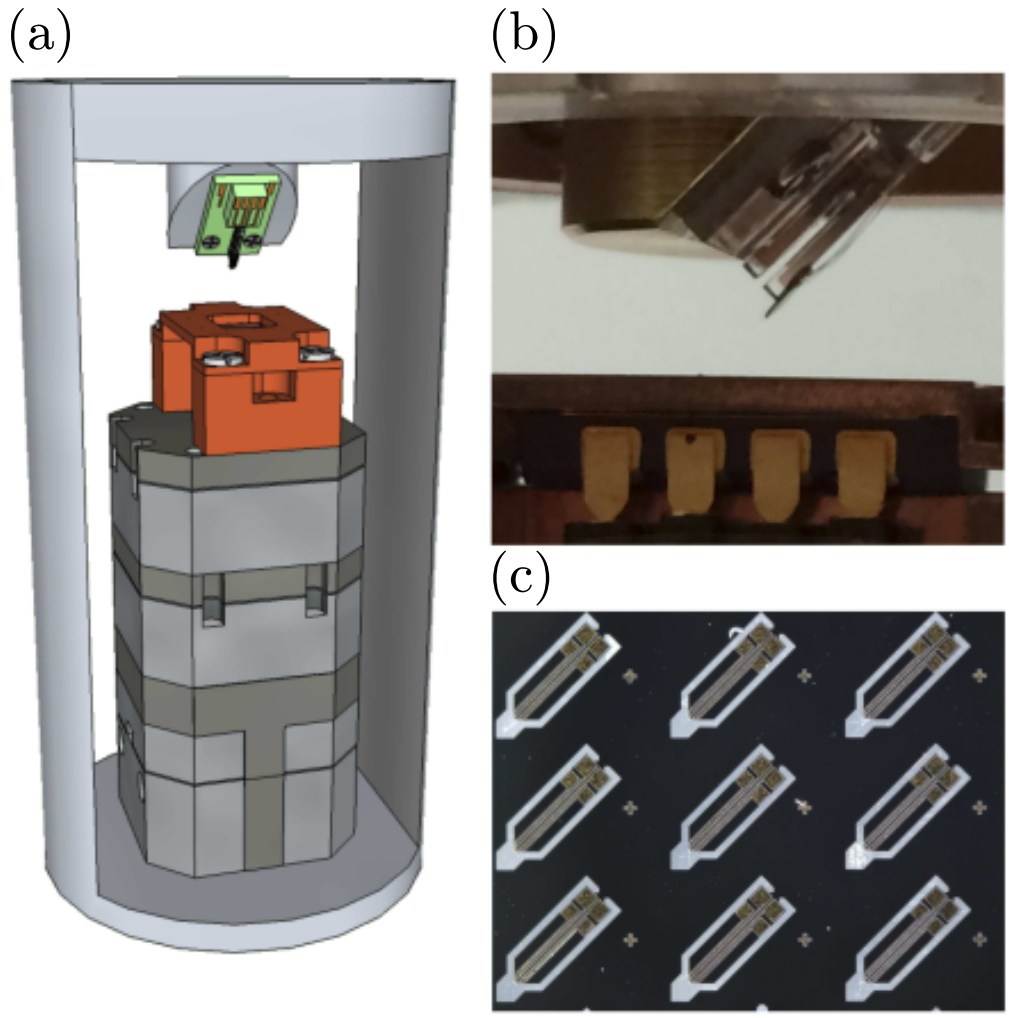

Fig. 3.1: (a) Schematic illustration of a scanning nano-SQUID system in a cryogen-free ^{4}He refrigerator. Upper green part indicates a holder for a scanning SQUID probe attached to a quartz tuning fork. A sample stage is placed on triaxial piezoelectric inertial stages. The SQUID probe and the piezoelectric inertial stages are settled in a stainless housing which is connected to the 4 K plate with four springs. (b) Optical image of a SQUID probe attached to a tuning fork and a sample chip carrier. (c) Optical image of probes fabricated by a laser-lithography and deep etching of a silicon substrate. After detaching each pieces, a nano-SQUID was fabricated at the tip of the probe by an FIB.

3.1.1 Characteristics of piezoelectric stages

A piezoelectric inertial stage is one of a linear actuator that is often used at low temperatures. It utilizes static friction and impulsive force caused by rapid displacement of a piezoelectric actuator. Piezoelectric actuator is extended by application of high voltage. When the applied voltage is switched off instantaneously, the actuator makes rapid contraction of the stage, which is placed on the actuator, and stays at nearly the same position. This mechanism is similar to "table-cloth-trick". A sawtooth wave is applied to achieve rapid displacement. We use this method of piezoelectric inertial stage for translation of x- and y- axis stages. The absolute positions were detected by resistive position encoders. Fluctuations of position reading value from the averaged values in each axis are shown in Fig. 3.2(a). Assuming a Gaussian distribution, the accuracy of the reading values of the position was estimated to be ± 38, ± 22, and ± 17 nm for x-, y- and, z-stage, respectively. We developed a control program for stage positionings using LabVIEW. In the program, stepping motion of x- and y- axis were repeated until reading values from the resistive encoder fell in the specified condition. Typical amplitude and period of applied sawtooth waves were 40 V and 50 ms, respectively.

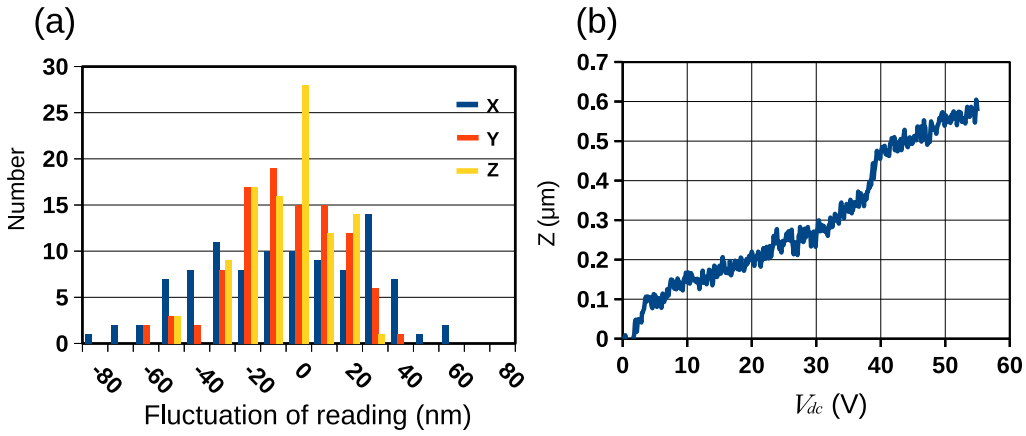

Fig. 3.2: (a) Histogram of reading position detected by resistive encoders. (b) Typical displacement of z-axis stage induced by dc voltage V_{dc} at 4 K.

In order to avoid unexpected crash of SQUID probe with sample surface, we avoid application of sudden sawtooth wave to the piezoelectric actuator for z-axis stage. Displacement of z-axis stage induced by applied dc voltage

V_{dc} at 4 K is shown in Fig. 3.2(b). The maximum displacement of 600 nm was archived at V_{dc} = 55 V. If a sudden displacement happens in range of several hundred nanometer, it is enough to make fatal destruction in the edge of SQUID probe Instead of the simple piezoelectric inertial stage driving, the z-axis stage was scanned by monitoring the signal of the quartz tuning fork in the fine positioning mode.

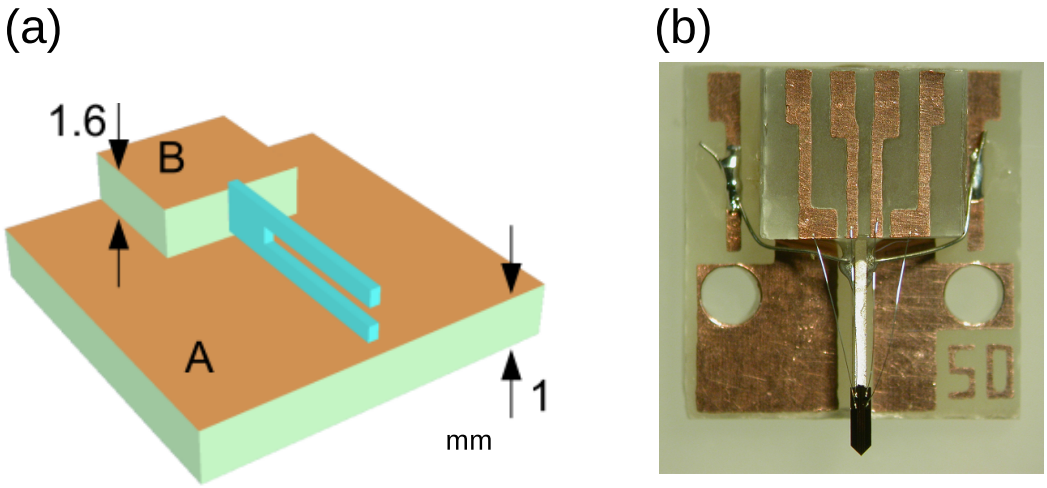

Fig. 3.3: (a) Schematic illustration of a scanning probe utilizing a quartz tuning fork. A and B are glass epoxy board with copper electrodes. A quartz tuning fork is glued on the side of the board B and the both stems are free-standing. (b) Photographic image of scanning nano-SQUID probe. A nano-SQUID substrate is glued on one side of stems.

3.1.2 Characteristics of quartz tuning fork

We employed a commercially available quartz tuning fork as a height feedback sensor of our probe in cryogenic environment. The resonance frequency of a commercial tuning fork in a metal cylindrical package was 32.768 kHz with a Q-factor $\sim$ 1,000,000 at room temperature.

A commercially available quartz tuning fork has two electrodes. For frequency characteristic measurement, we applied AC voltage to one side of the electrodes and detected piezoelectric signal as displacement current by a lock-in amplifier. In our system, we mainly measured the amplitude of

the displacement current (I_{TF}) for resonant frequency shift detection. To achieve a high signal to noise ratio, coaxial cables with impedance matched connections were used.

Schematic illustration and photographic image of our probe are shown in Fig. 3.3. At first, we unpacked a quartz tuning fork from cylindrical package and glued on a side of glass epoxy board B indicated in Fig. 3.3(a). After complete gluing, board B was fixed on a glass epoxy board A which had two electrodes for the quartz tuning fork. At this time, a down side stem of the fork should spread from a surface of board A. In other words, we utilized the quartz tuning fork in free-standing. After soldering the two electrodes, we glued a SQUID probe substrate to the top of the quartz tuning fork by two-components epoxy adhesive. Finally, we connected four electrodes of the probe substrate to the board B by aluminum wire of 30 μm in diameter.

Fig. 3.4(a) indicates typical frequency-I_{TF} characteristics of a tuning fork in each step of assembling, gluing on the board B (i), with the probe substrate (ii) and after wire bonding(iii). All the measurements in Fig. 3.4(a) were carried out under atmospheric pressure at room temperature. The applied voltage was 7 mV. After gluing a tuning fork to the substrate of a SQUID probe, the resonance frequency decreased and the Q-factor was degraded to several hundred at room temperature.

A frequency-I_{TF} characteristics at 4 K is shown in Fig. 3.4(b). At cryogenic temperature, the resonance frequency typically increased to around 30 kHz, and the Q-factor increased to over 10,000. These improvements in the resonance characteristics are mainly caused by rigid gluing at low temperature. With this high Q-factor, a tuning fork can be used in a phase-locked loop circuit.

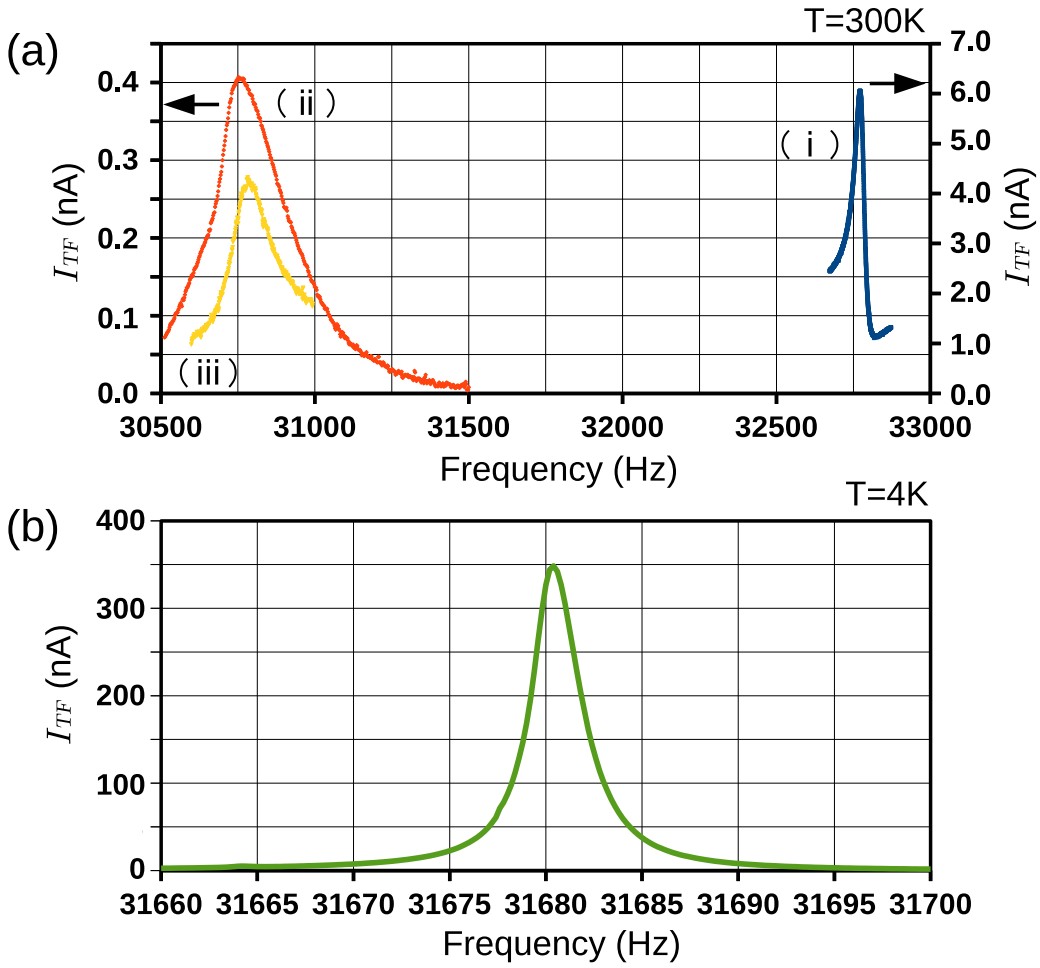

Fig. 3.4: (a) Typical frequency-I_{TF} characteristics of tuning fork without a nano-SQUID substrate (i), with the substrate (ii) and with four aluminum wires (iii) under atmospheric pressure at room temperature. The estimated Q-factors were 480, 100 and 130 for (i), (ii) and (iii), respectively. (b) Typical frequency-I_{TF} characteristic of a nano-SQUID probe at 4 K. Q-factor was about 10,000.

3.1.3 Operating procedures for height and scan control

Height control procedure was achieve by successive measurement of the quartz tuning fork current during stepwise increment of the applied voltage to the z-axis piezoelectric stage. As shown in Fig. 3.2(c), the length of the piezoelectric actuator increases by application of static voltage V_{dc}. The relation between a shift of z-axis and applied voltage is approximately expressed as $12\frac{nm}{V}$.

A schematic diagram of the height are shown in Fig. 3.5(a). We applied incremental voltage to a piezoelectric actuator of z-axis stage with a step size d. In each step, we measured I_{TF} with waiting time t. If the edge of the probe touched to the sample surface, visible change in I_{TF} was detected. When a change of I_{TF} was larger than threshold value, the increment process was stopped immediately and V_{dc} was decreased to zero. The threshold value was empirically determined. In a typical height control procedure, the increment voltage step d, the maximum applied voltage $\max(V_{dc})$, and the delay time for I_{TF} measurement t were 0.5 V, 50 V, and 40 ms, respectively. With these parameters, the increment shift step was about 6 nm. As mentioned earlier, application of a sawtooth wave may cause sudden crash of the nano-SQUID probe to the sample surface with several hundred nanometer range. As Compared with the case of sawtooth modulation, our procedure more precisely controls the height.

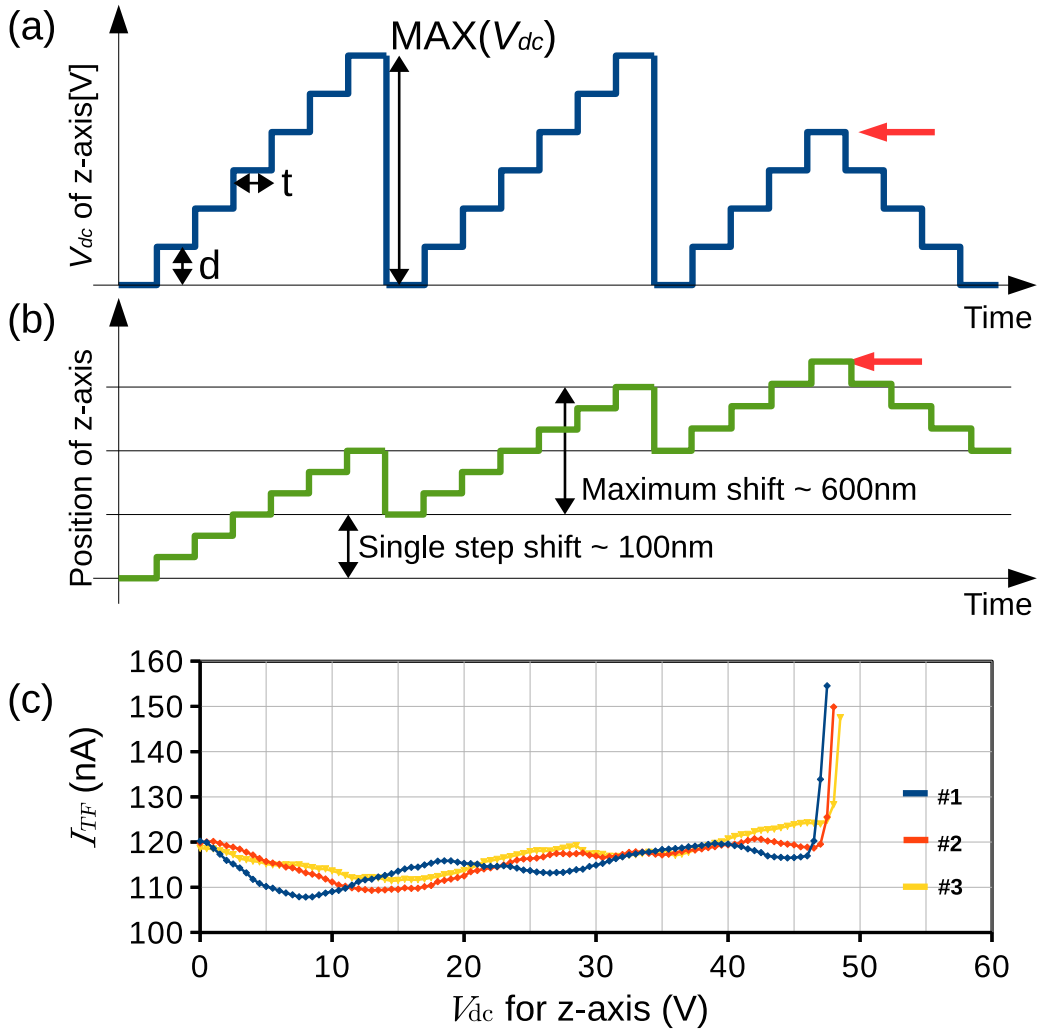

Fig. 3.5: (a) Schematic diagram of height control procedure. During stepwise increment of applied static voltage V_{dc}, displacement current I_{TF} of a tuning fork was measured successively. If a sudden shift of I_{TF} is detected, increment procedure is stopped immediately and V_{dc} will decrease slowly. A corresponding position of z stage is shown in (b). Typical value of the step d, the maximum V_{dc}, and the delay time t were 0.5 V, 50 V and 40 ms, respectively. (c) Typical behavior of I_{TF} during height control procedure. Three curves were measured using the same parameters.

3.1.4 Calibration of solenoidal superconducting magnet

We used a home-made solenoidal superconducting magnet for SQUID measurements. An photograph and a schematic configuration are shown in Figs. 3.6 (a) and (b), respectively. The length and the diameter of the superconducting magnet are 60 mm and 40 mm, respectively. The magnet is fixed to the 4 K plate of our ^{4}He cryogen-free refrigerator through four copper rods. Triaxial scanning stages and a SQUID probe are suspended by four springs to reduce low-frequency vibrations caused by the cooling cycle. A nano-SQUID probe was positioned at the center of the magnet. The displacement of the nano-SQUID was small.

The home-made solenoidal superconducting magnet was calibrated by a linear output Hall effect transducer (SS94A1F, Honeywell Co., Ltd.) with a magnetic sensitivity m_{Hall} of 250±5 mV/mT. The transducer was fixed at the center of the magnet and the output voltage V_{Hall} was measured at room temperature by digital multi meter (34410A, Agilent Co., Ltd.) and the magnet current I_{mag} was supplied by a current source (GS200, Yokogawa Co., Ltd.). From the measurement, we obtained a proportional relation of $V_{Hall} = aI_{mag}$. By using a least square linear fitting, the slope a was determined to be 1.282±0.002 mV/mA. V_{Hall} follows the relation $V_{\mathrm{Hall}} = m_{\mathrm{Hall}}\mu_0 H$. Consequently, the proportional relation of the magnet was given by $\mu_0 H = \frac{a}{m_{\mathrm{Hall}}} I_{\mathrm{mag}}$. By considering the propagation of errors, a proportional coefficient $\frac{a}{m_{\mathrm{Hall}}}$ was estimated to be (5.13±0.10)×10^{-3} mT/mA. Assuming the diameter of superconducting wire is much smaller than the diameter of the magnet, magnetic field at the center of the single-layered solenoidal coil with a length l, a diameter d and the number of turns in unit length n is approximately given by

$$\mu_0 H = \mu_0 n I_{\mathrm{mag}} \frac{l/2}{\sqrt{(l/2)^2 + (d/2)^2}}. \tag{3.1}$$

The number of turns n was counted from optical micrographs of the magnet as 7100 turns/m. Consequently, a proportional constant of the $\mu_0 H$-I_{mag} relation at the magnet center was estimated to be 4.95×10^{-3} mT/mA.

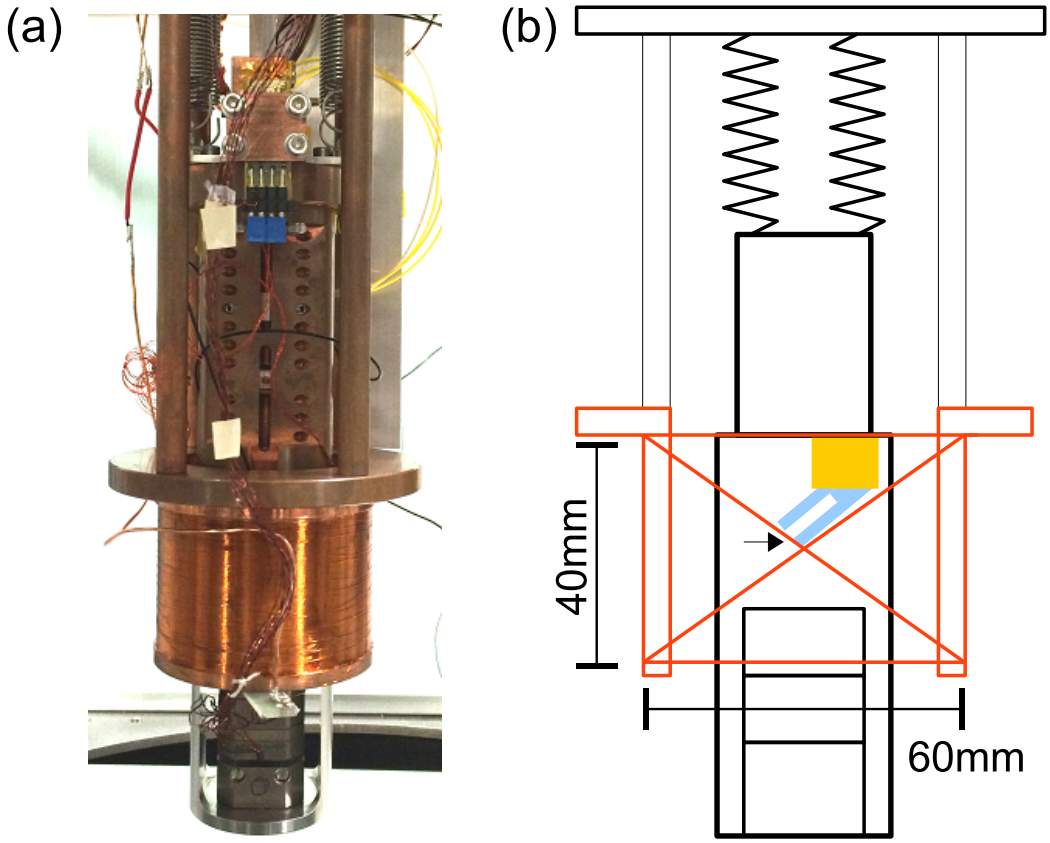

Fig. 3.6: (a) Optical image of triaxial piezoelectric inertial stage accommodated in a copper enclosure and a superconducting magnet in a ^{4}He cryogen-free pulse tube refrigerator. The SQUID probe is located at the center of the bore of the superconducting magnet. (b) Schematic illustration of the stage and the magnet. Orange line indicates a home-made solenoidal superconducting magnet suspended by four copper rods from the 4 K stage of the refrigerator. Black arrow indicates the position of a SQUID probe. Triaxial piezoelectric inertial stage and a SQUID probe accommodated in a copper enclosure are suspended by four springs from the 4 K plate to reduce vibrations due to a pulse tube refrigerator.

3.2 Characteristics of SQUID probes

SQUID readout circuit based on standard four-terminal measurements were constructed in ^{4}He cryogen-free refrigerator. We used a differential voltage amplifier at room temperature. DC voltage measurements using a digital multimeter and ac voltage measurements using a lock-in amplifier and a functional generator were conducted simultaneously.

3.2.1 Temperature dependences of current-voltage characteristics

Figs. 3.7 (a), and (b) show I-V characteristics of nano-SQUID probes without and after mechanical polishing, respectively, at temperatures between $T =$ 3.6 and 6.8 K at zero applied magnetic field. The current was swept in both negative and positive directions, and no hysteresis was observed in the I-V characteristics in Figs. 3.7 (a), and (b). The Dayem nano-SQUID was shown to exhibit a hysteretic behavior for $L_{\rm SQ}/\xi > 3.5$, [45] where $L_{\rm SQ}$ is the Dayem nano bridge size and ξ is the Ginzburg-Landau coherence length, which is 38 nm for Nb. [2] The constrictions of the nano-SQUID were milled to wedged shape by the FIB process with the weak link width of $w = 80$ nm. Although the model by Likharev [45] is not directly applicable to the geometry of our nano-SQUIDs, the nonhysteretic behavior of I-V characteristics is explained by small $w/\xi = 2.1$. Furthermore, we reduced the effects of Joule heating by reducing the critical current I_c and preparing Au film above Nb film for heat conduction, which is also important for the nonhysteretic behavior of I-V characteristics of our nano-SQUIDs.

The critical temperature T_c of the nano-SQUID without mechanical polishing was 6.0 K, which is reduced from typical T_c of Nb of 9.2 K due to small thickness of the Nb film and the proximity effect between Nb and Au. [13] Fig. 3.7(a) shows a typical I-V characteristics of the nano-SQUID probe without mechanical polishing (Fig. 2.6(a)) at applied magnetic fields between 0.1 and 0.5 mT at 4.2 K. The critical current I_c is seen to change with the applied magnetic field.

The SQUID loop of the probe after mechanical polishing of the tip of the nano-SQUID probe (Fig. 2.6(b)) was located very close to the edge of the Si substrate and the probe did not exhibit zero resistance as shown in Fig. 3.7(b) above 3.6 K because of the damage of Nb film during the fabrication process. Nevertheless, the change of the voltage with the applied

magnetic field was observed as shown in Fig. 3.8(b), indicating that this nano-SQUID probe is useful as a magnetic field sensor. The nonhysteretic behavior of our nano-SQUIDs enables us to measure the voltage of a nano-SQUID (V_{SQ}) at a constant bias current to obtain magnetic flux threading the SQUID loop. This is particularly advantageous to use a nano-SQUID as a magnetic sensor for a scanning microscope. If a nano-SQUID shows a hysteretic I-V characteristic, I_c has to be measured by sweeping I at each point.

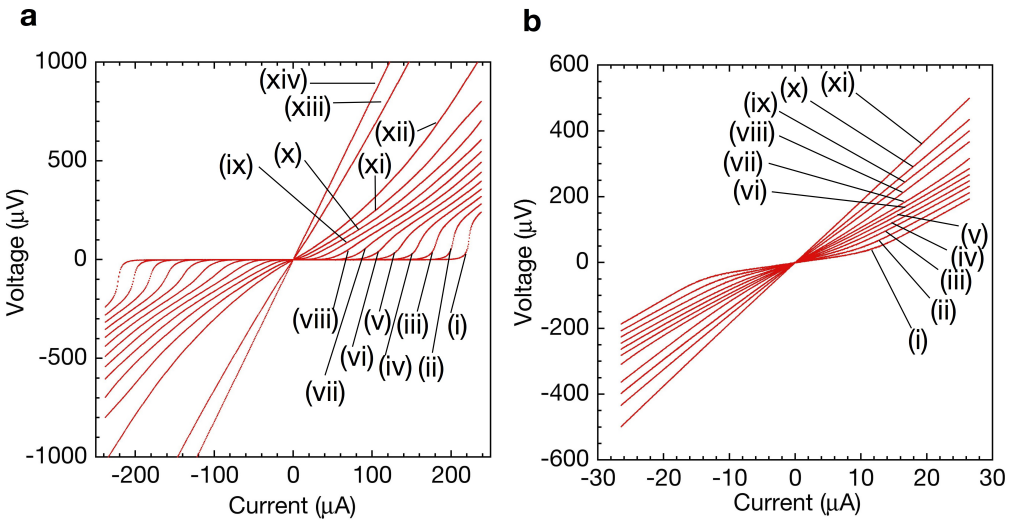

Fig. 3.7: (a) Current-voltage characteristics of a SQUID probe without mechanical polishing at T = (i) 3.6, (ii) 3.8. (iii) 4.0, (iv) 4.2, (v) 5.0, (vi) 5.2, (vii) 5.4, (viii) 5.6, (ix) 5.8, (x) 6.0, (xi) 6.2, (xii) 6.4, (xiii) 6.6, (xiv) 6.8 K. The current was swept for both negative and positive directions, and no hysteresis in the I-V characteristics was observed. (b) Current-voltage characteristics of a SQUID probe after mechanical polishing at T = (i) 3.6, (ii) 3.8. (iii) 4.0, (iv) 4.2, (v) 5.0, (vi) 5.2, (vii) 5.4, (viii) 5.6, (ix) 5.8, (x) 6.0, (xi) 6.2 K. No hysteresis in the I-V characteristics was observed.

3.2.2 Magnetic filed dependences of current-voltage characteristics

Fig. 3.8 (a), and (b) show typical current-voltage characteristics of nano-SQUID probes without and after mechanical polishing, respectively, at external magnetic fields between 0.1 and 0.5 mT. We applied a continuous trianguler wave current at the frequency of 0.1 Hz to our SQUID through a bias resistor and measured the voltage between the two SQUID terminals with a digital multimeter at the interval of 10 ms. After measurements for 10 s, we obtained a current-voltage curve corresponding to a cycle of the applied triangular wave. This method was used to obtain current-voltage curves in the external field B_{ex}.

3.2.3 Critical current modulation in a magnetic field

The current-voltage curves are seen to change with the external magnetic field ($B_{\rm ext}$) as shown in Figs. 3.8 (a) and (b). Typical critical current modulations in a magnetic field are shown in Figs. 3.9(a) and (b). Here we plotted the current at threshold voltage $V_{\rm th}$ as critical current I_c. The effective area of the SQUID loop was estimated to be 2.24 μm $\times$ 2.24 μm from the modulation period of I_c.

3.2.4 SQUID voltage modulation in a magnetic field

Typical voltage-magnetic field ($V_{\rm SQ}$-$B_{\rm ext}$) characteristics in Figs. 3.8(c) and 3.8(d) show oscillations of SQUID voltage $V_{\rm SQ}$ with $B_{\rm ext}$ at constant current-bias. The noise of the probe without mechanical polishing was estimated to be 3.1 nT/$\sqrt{\rm Hz}$ at 2 kHz. The noise of the probe after mechanical polishing was degraded to 40 nT/$\sqrt{\rm Hz}$ at 2 kHz while the spatial resolution was improved.

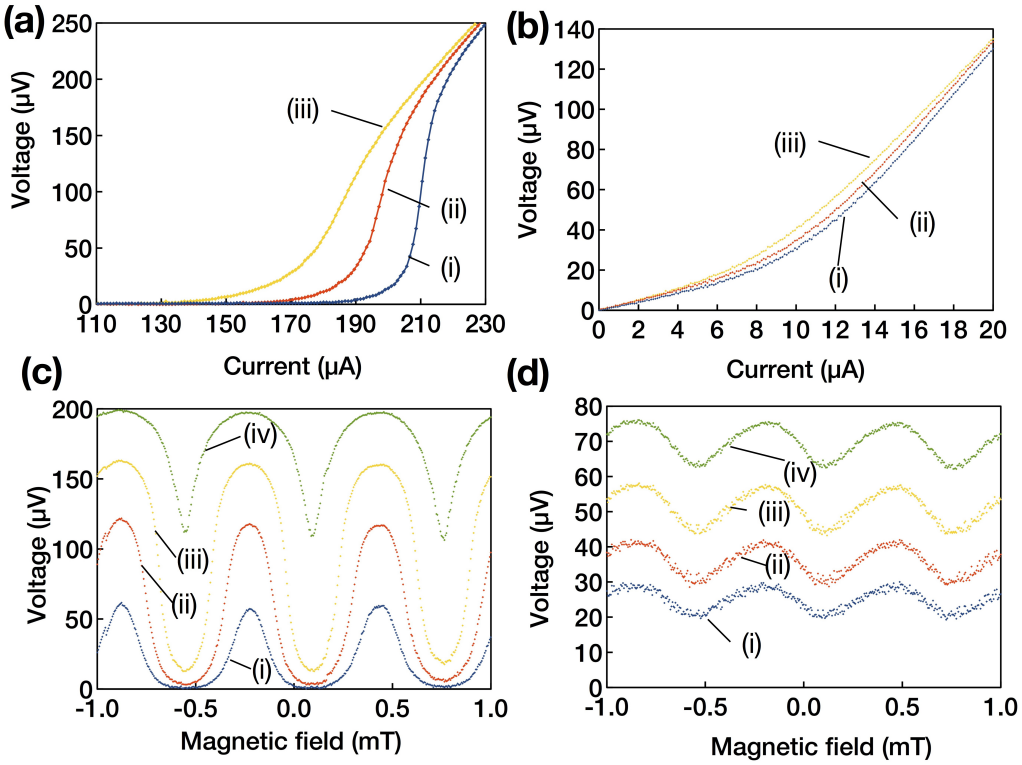

Fig. 3.8: (a) Typical current-voltage characteristics of a nano-SQUID probe without mechanical polishing and (b) after mechanical polishing of the tip of the probe at applied magnetic field of (i) 0.5, (ii) 0.3, and (iii) 0.1 mT. No hysteresis in the I-V characteristics was observed. (c) Modulation of SQUID voltage (V_{SQ}) by B_{ext} at current-bias of (i) 196.2, (ii) 198.1, (iii) 200.0, and (vi) 201.9 μA for a nano-SQUID probe without mechanical polishing. (d) Modulation of SQUID Voltage (V_{SQ}) in B_{ext} at current-bias of (i) 8.0, (ii) 10.0, (iii) 12.0, and (vi) 14.0 μA for a nano-SQUID probe after mechanical polishing.

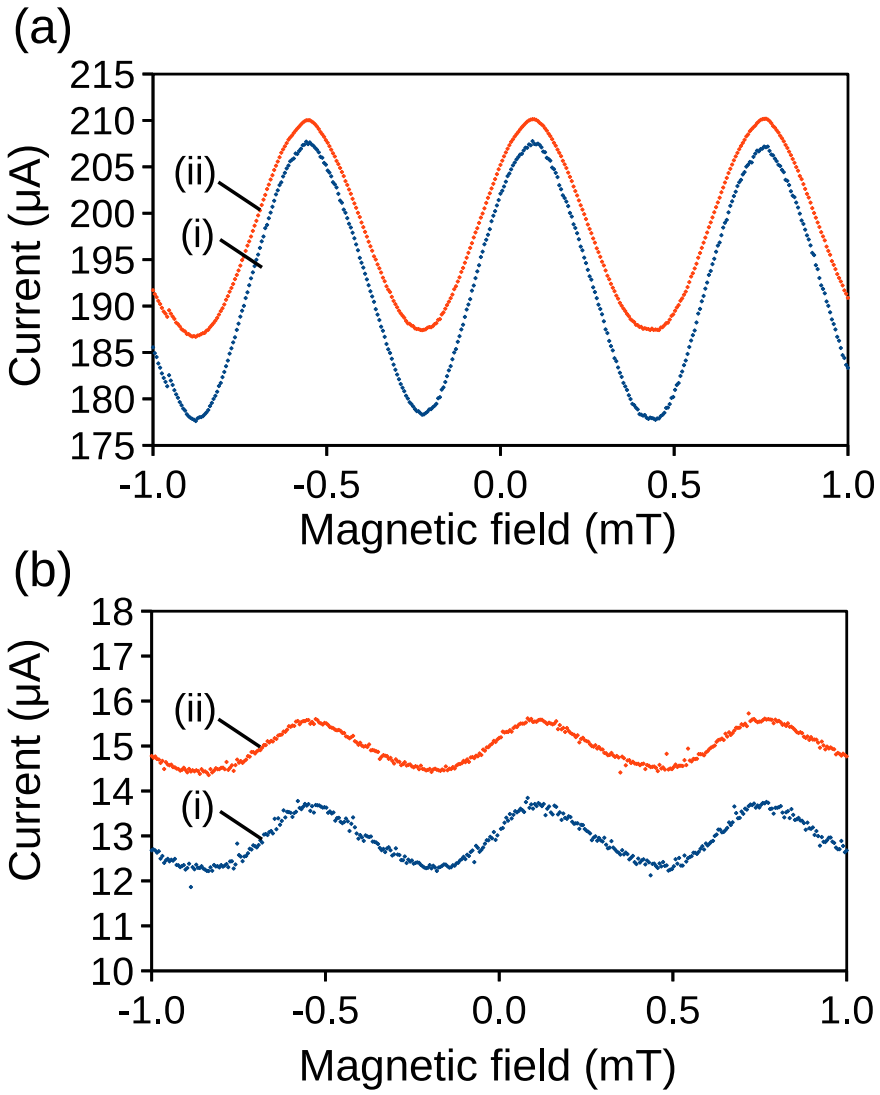

Fig. 3.9: (a) Modulation of critical current (I_c) in B_{ext} at threshold voltage of (i) 50 and (ii) 100 μV for a nano-SQUID probe without mechanical polishing. (b) Modulation of critical current (I_c) in B_{ext} at threshold voltage of (i) 60 and (ii) 80 μV for a nano-SQUID probe after mechanical polishing.

3.3 Magnetic field sensitivity of SQUID probe

As described in Sec.2.2, we used a lock-in detection for SQUID voltage (V_{sq}) at a constant current bias (I_{sq}). Because of current-voltage characteristics without hysteresis and rounded superconducting transition as shown in Fig. 3.8(a) and (b), V_{sq} was measured continuously by sweeping the external magnetic field. In a typical measurement, the magnitude of the current was set such that the slope of current-voltage characteristics is maximum in sweeping the external magnetic field. Higher sensitivity to the external magnetic field may be achieved by optimizing the SQUID current. Fig. 3.10(a) shows a typical magnetic field dependence of SQUID voltage. The red line indicates the slope of the curve. We assume a linear dependence of V_{sq} on magnetic field for small deviation from the magnetic field indicated by the arrow. The slope was estimated to be 2.01 V/T. We also measured noise spectra of the output voltage from a differential preamplifier (LI75A, NF Corporation) with a voltage gain of 100. Fig. 3.10 (b) shows magnetic field noise spectra of our system. Using the magnetic sensitivity estimated from Fig. 3.10(a), the output voltage noise was converted to magnetic field noise. From the noise spectra, minimum magnetic field sensitivity was estimated to be 3.1 nT/Hz$^{1/2}$ at 2 kHz. Normalized minimum magnetic flux sensitivity by Φ_0 was estimated to be 7.5 $\mu\Phi_0$/Hz$^{1/2}$ at 2 kHz. Here we used an effective SQUID loop area of 2.24 μm $\times$2.24 μm, which was derived from modulations of critical current in external field (Fig. 3.9). From Eq.(1.66), an optimal magnetic flux sensitivity $\approx (4kTL^2/R)^{1/2}$ was estimated to be 4.5 nΦ_0/Hz$^{1/2}$, where the inductance L of 1.6 pH, temperature T of 3.7 K and the normal resistance R of 3.6 Ω was used. The difference of the sensitivities was mainly caused by the electrical noise from a preamplifier at room temperature. However, the magnetic flux sensitivity of our system is comparable to previous works for scanning SQUIDs which was coupled to the measuring objects directly [5, 32, 34].

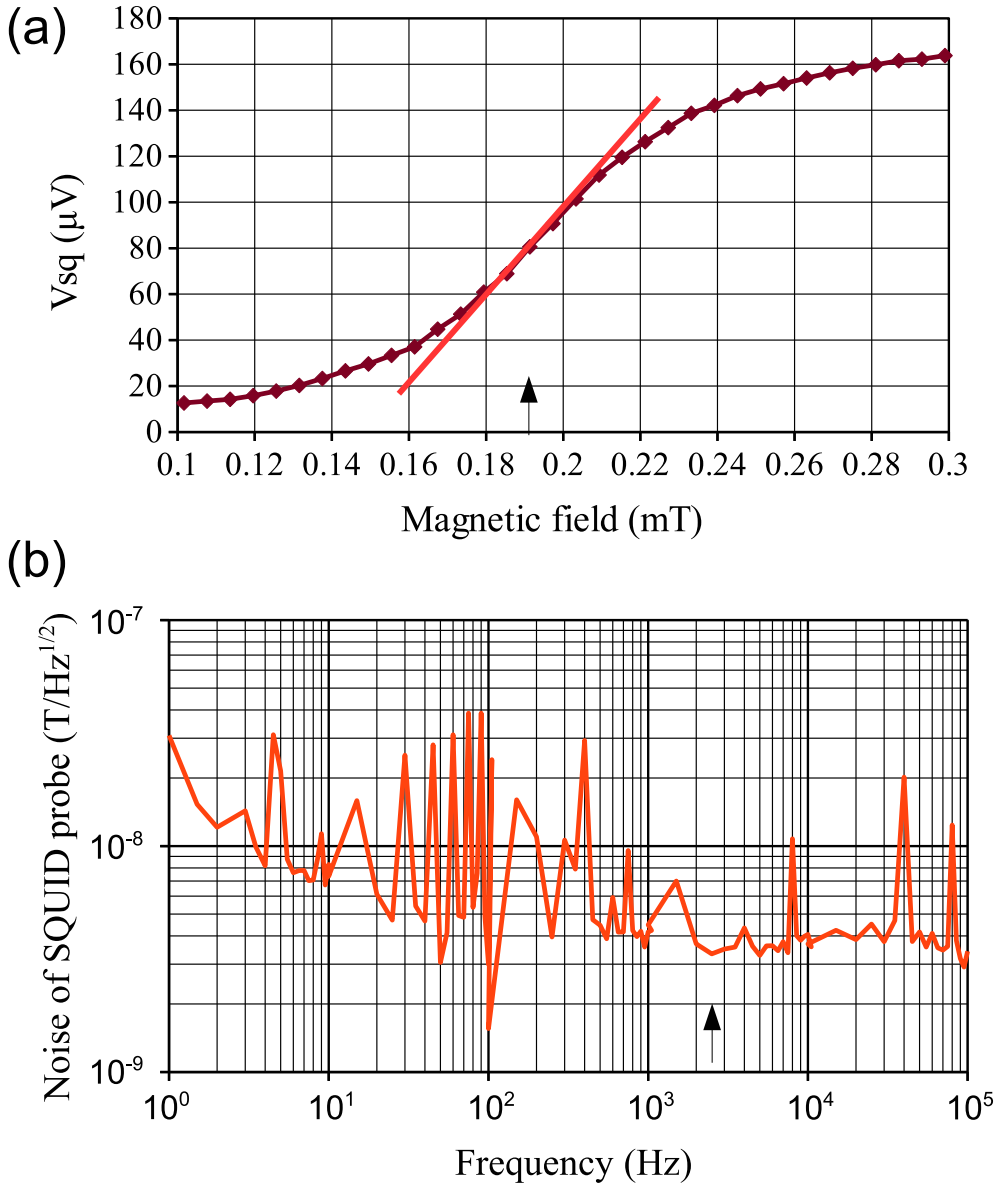

Fig. 3.10: SQUID voltage and magnetic field noise spectra of scanning nano-SQUID probe. (a) Magnetic field dependence of SQUID voltage (V_{sq}) at a constant current bias of 210 μA. (b) Magnetic field noise at the external magnetic field of 0.19 mT at 3.7 K.

3.4 Spatial resolution and magnetic coupling of scanning nano-SQUID microscope

In local magnetic measurement for small samples, a spatial resolution of magnetic image and an efficiency of magnetic coupling which is given by the highest detectable magnetic signal from samples are important features of measurement system. The spatial resolution and the efficiency depend extensively on a distance d between samples and magnetic sensor [5]. One of a challenging approach in developing of our scanning nano-SQUID microscope system was reducing the distance. In this section, at first, we introduce some reports for a spatial resolution of scanning SQUID microscope and explain about our evaluation of the resolution. Second, we mention a magnetic coupling efficiency using the result of height dependent scanning measurement.

3.4.1 Evaluation of spatial resolution

There are several schemes for evaluation of spatial resolution in scanning SQUID microscope measurements in the literatures. One method is to simply define the spatial resolution of a scanning SQUID microscope as the size of the SQUID loop [32]. Faley et al. measured line profiles of magnetic field induced by current carrying wires [15]. The distance d and the inner diameter of their SQUID were 400 μm and 50 μm, respectively. From the maximum horizontal gradient of a magnetic field profile and the magnetic field resolution, they estimated the spatial resolution to be 25 μm. For a self-aligned nano-SQUID on tip, Vasyukov et al. demonstrated a minimum spatial resolution of 20 nm based on a simulation for single spin oriented in the plane of the SQUID loop. [31] In their simulation, the distance d and the diameter of the loop were assumed be 10 nm and 160 nm, respectively. Baudenbacher et al. measured a spatial distribution of remnant magnetization of a 50 μm-thick geological thin section taken from a meteorite [14]. From the magnetic image, they estimated the spatial resolution to b 80 μm. In their experiment, the distance d and the effective area of SQUID were 100 μm and 86 μm $\times$ 86 μm, respectively.

We evaluated the spatial resolution of our scanning nano-SQUID microscope system from a magnetic field image around Nb/Au superconducting electrodes as shown in Fig. 3.11(a). The designed width and the spacing between the electrodes were 2 μm and 7 μm, respectively. The thicknesses of Nb and Au films were 600 and 30 nm, respectively. The superconducting

critical temperature of the Nb/Au electrode was 8.6 K. To evaluate the spatial distribution of our system, we used a mechanical polished nano-SQUID probe that was used for measurements in Fig. 4.3. We measured the SQUID voltage V_{sq} under a constant current bias I_{sq} of 13 μA in a constant applied magnetic field of 1.1 mT at 4 K. The estimated distance d between the nearest JJ and a sample surface was 1.2 μm. V_{sq} was measured by ordinal digital multimeter. The voltage to magnetic field transfer function was 30 mT/V which measured just before this scanning operation. An magnetic field image of niobium superconducting electrode is shown in Fig. 3.11(b). Scanning direction was shown by the black arrow. One can recognize a visible depression of magnetic field corresponding to the niobium electrode. Line profiles of each y-axis are shown in Fig. 3.11(c). We evaluated the full width at half maximum (black dashed line) of the magnetic field depression induced by perfect diamagnetism of single niobium electrode. From this evaluation, we concluded that a spatial resolution of our microscope system was better than 2 μm.

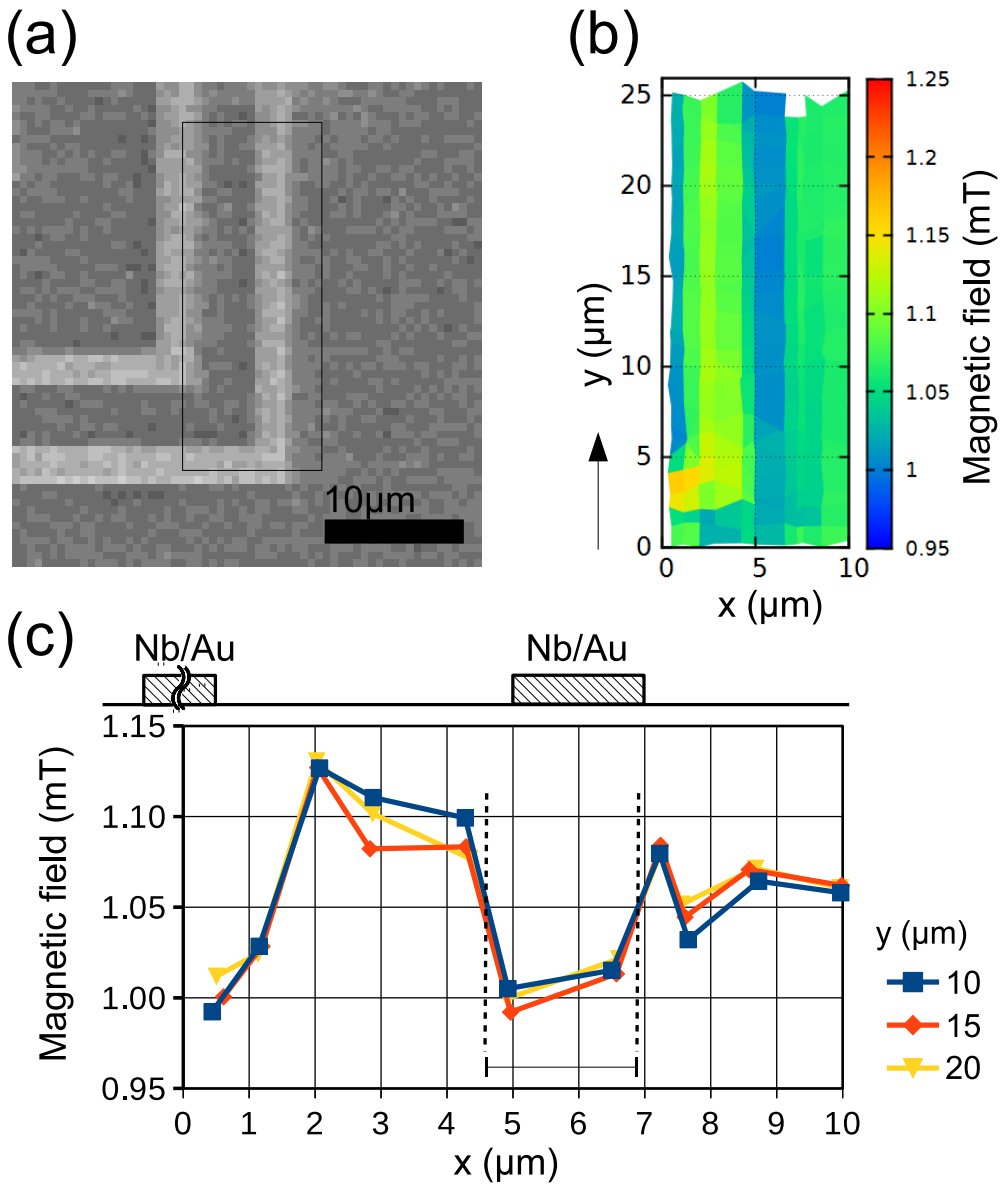

Fig. 3.11: Image and mapping of magnetic field distribution of Nb/Au strips. (a) Scanning electron microscope image of Nb/Au strips with a width of 2 μm and a spacing of 5 μm at applied magnetic field of 1.05 mT at 4 K. Scanning area is shown by black line. (b) Mapping of magnetic field distribution of Nb/Au strips. (c) Line profiles of magnetic field distribution along (i) y = 10, (ii) 15, and (iii) 20 μm.

Chapter 4

Local measurement of magnetic flux induced by current density in two-dimensional electron system

4.1 Background: local magnetic flux imaging and 2-dimensional current density distribution

Imaging of current distribution is a common problem in not only physics but also biology and industry. In many situation, noninvasive and nondestructive measurement technique is desired. Reconstruction technique for current distribution based on local magnetic imaging is one of a solution. In general, a correspondence relationship between magnetic field and current distribution is too complex to deal with analytically. However, in two dimensional system, we can obtain a unique solution for the inverse problem. Bradiey ,et al. investigated a mathematical algorithm for imaging of two-dimensional current distribution from local magnetic field imaging. They used a Fourier transform and green function as a spatial filtering to obtain a two-dimensional real space current distribution from local imaging of normal component of magnetic field. With considering about $\nabla \cdot \mathbf{J}(\mathbf{r}) = 0$ where $\mathbf{J}(\mathbf{r})$ is a current in real space, we can also obtain a current distribution in arbitrary angle of

geometrical configuration of SQUID. In above section, we discussed in detail.

Ideal two-dimensional electron system is formed in GaAs/Al_xGa_{1-x}As modulation-doped single heterojunction. In the system, current flowing through the sample is consisted of high-mobility electrons. Differently from ordinal metal electrode, a current distribution caused by high-mobility carriers is not trivial. Thus it is expected that an imaging of such a current distribution reveals a behavior of ballistic carriers in detail.

At first, we will explain properties of our Hall-bar structure sample formed in GaAs/Al_xGa_{1-x}As modulation-doped single heterojunction. Next, we will show results of local imaging of magnetic field induced by current flowing in the Hall-bar structure with using two different type of SQUID probe. Finally, we will discuss about current distributions obtained from magnetic field imaging.

4.2 Samples

4.2.1 A Hall-bar structure of GaAs/Al_xGa_{1-x}As modulation-doped single heterojunction

GaAs/Al_xGa_{1-x}As modulation-doped single heterojunction is widely used to host high mobility 2DEG. We fabricated a Hall-bar structure and measured the magnetic flux distribution due to current in the Hall-bar structure by using our scanning nano-SQUID system. Scanning nano-SQUID microscope is expected to be useful in investigating unknown current distributions in two-dimensional systems. The sample GaAs/$Al_{0.3}Ga_{0.7}$As modulation-doped single heterojunction consists of a GaAs/AlAs superlattice buffer layer, 200 nm-thick undoped GaAs layer, 40 nm-thick undoped $Al_{0.3}Ga_{0.7}$As layer, 30 nm-thick Si-doped $Al_{0.3}Ga_{0.7}$As layer, and 10 nm-thick Si-doped GaAs capping layer. The density and the mobility of the two-dimensional electron gas were 3.3×10^{15} m^{-2} and 91 m^2/Vs at 2.8 K, giving the mean free path of electrons of 8.7 μm. A Hall-bar structure of the width and the length of 25 and 300 μm was fabricated by photolithography. Figs 4.3 (a) and (b) are a schematics and an optical micrograph of the Hall-bar sample. Mesa of Hall-bar structure was defined by a wet chemical etching using H_2O_2/citric acid solution. The etching depth was about 100 nm. The distance between the voltage probes was 100 μm. Current between ohmic contacts of the Hall-bar structure was modulated at 1873 Hz. The voltage of a SQUID probe at a

constant current bias changes due to magnetic field created by the current in the Hall-bar structure. This voltage change was detected synchronously with a lock-on amplifier at a time constant of 1 s by scanning the nano-SQUID probe on the surface of the sample.

4.2.2 Characterization of GaAs/Al_xGa_{1-x}As modulation-doped single heterojunction sample

To investigate properties of GaAs/Al_xGa_{1-x}As modulation-doped single heterojunction sample, we performed Hall-bar measurements at 320 mK and 2.8 K using a ^{3}He cryogen-free refrigerator. From results measured at 320 mK and 2.8 K with bias current $I_{\rm bias} = 9.9$ nA, the electron mobility was 97.7 and 90.6 $\rm m^2V^{-1}s^{-1}$, respectively. We also evaluated the bias current dependence of Hall resistance and longitudinal resistance. In our sample, the Shubnikov-de Haas oscillations of longitudinal resistance disappeared for $I_{\rm bias} > 10$ μA.

4.3 Mappings of flux distribution in GaAs/$Al_xGa_{1-x}As$ modulation-doped single heterojunction sample

In this section, scanning probe measurements of flux distribution on the surface of a Hall bar structure are described. All of the results in this section were measured under geometrical configuration as schematically shown in Fig. 4.1.

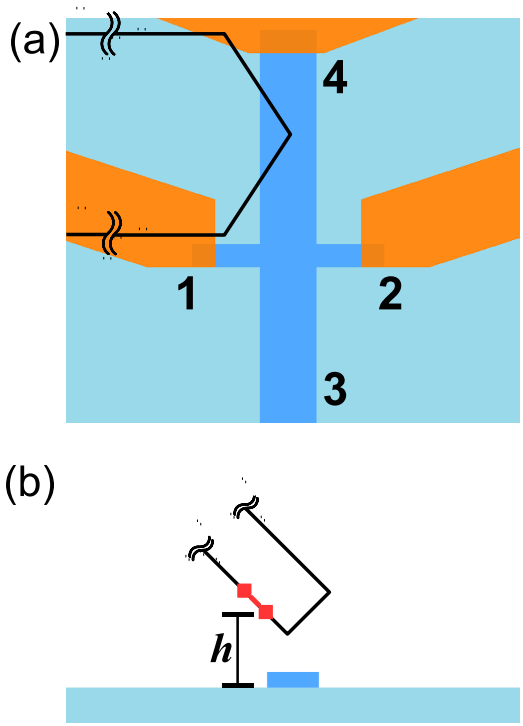

Fig. 4.1: Schematic configuration of scanning measurement of a Hall-bar structure. (a) Top view (b) and side view are shown. A Hall-bar structure is indicated by blue in (a) and (b). A SQUID probe is indicated by black thick line. A dc-SQUID is illustrated by red line in (b). Diamonds at the both sides of the red line indicate the positions of weak link type Josephson junctions (JJ). We define the height h of the probe as the distance between the nearest JJ and the sample surface as shown in (b).

Height dependence of flux signal

As described in Chapter 2, degradation of superconductivity on the top of the probe makes it difficult to fabricate a nano-SQUID structure within 2.2 μm from the substrate edge.

We performed scanning probe measurements using one of a nano-SQUID probe without polishing called No. 04. In the probe No. 04, a Josephson junction was fabricated 5.5μm from the probe tip of the nano-SQUID structure. After several scanning experiments using a prototype of touch down procedure, the tip of No. 04 was ground down and the distance between the JJ and the probe edge became 3.1μm. In the following measurements, we used improved touch down procedure and constant height scanning process. Thus we could assume that the distance between the nearest JJ and the probe top was unchanged. For the mounting angle of 51° to the sample surface, the minimum value of the height h was 2.4 μm.

Height dependence of flux signal for sample current (I_{sample}) of 7, 35, and 70 μA is shown in Fig. 4.2.

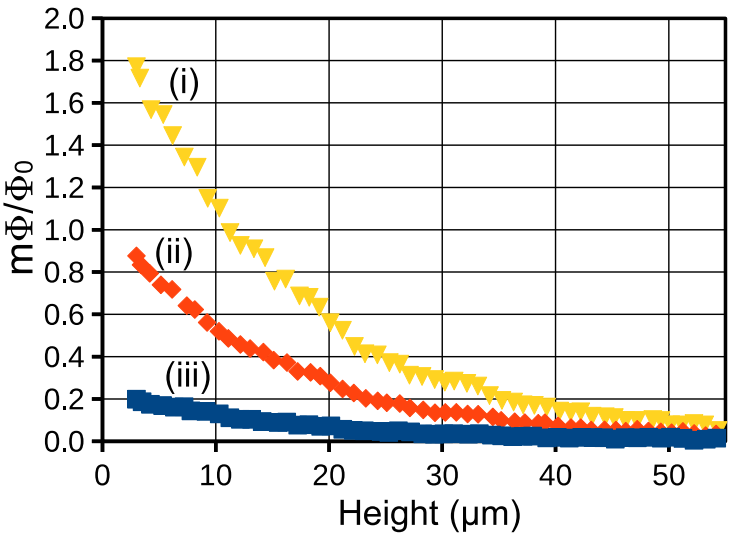

Fig. 4.2: Height dependence of magnetic flux at I_{sample} = (i) 70, (ii) 35, and (iii) 7 μA.

Mappings of flux distribution

Results of mappings of magnetic field created by ac current between the voltage probes 1 and 2 of the Hall-bar structure (Figs. 4.3 (a, b)) at $I_{\rm sample}$ = 70 and 2.8 μA are shown in Figs. 4.3 (c) and (d), respectively, at $T = 4$ K at the applied magnetic field by a superconducting magnet of 0.0 mT using a probe after mechanical polishing. The distance between the nearest JJ and the probe top is 1 μm, and the minimum height from the sample surface, in our configuration of scanning measurement, is estimated as 700 nm. We will show some results of local magnetic field measurement using this nano-SQUID probe.

The measurements were performed in unshielded laboratory environment, and hence the sample and the nano-SQUID probe were subject to the environmental magnetic field. The size of the scanning area was 80×80 μm^2 with a step size of 2 μm for x- and y-directions. The height of the SQUID probe from the sample surface was $z_0 = 1.5$ μm. The voltage of a SQUID at a constant current bias of 12 μA changes due to magnetic field created by the current in the Hall-bar structure. This voltage change was synchronously detected with a lock-in amplifier at a time constant of 1 s by scanning the position of the nano-SQUID probe on the surface of the sample. The bias current of $I_{\rm sample}$ = 70 and 2.8 μA corresponds to current density of 7.0 and 0.28 A/m, respectively. The mapping in Fig. 4.3 (c) (Fig. 4.3 (d)) corresponds to the case of the current density above (below) the condition for the breakdown of the quantum Hall effect. [63, 64] The maximum source-drain voltage ($V_{\rm SD}$) was 8.0 mV at $I_{\rm sample} = 70$ μA. The Fermi energy of the electrons is $\epsilon_F = 12$ meV at the electron density of the sample of $n_s = 3.3 \times 10^{15}$ m^{-2}, which gives $eV_{\rm SD} < \epsilon_F$. The positive and negative magnetic fields are observed near the edges of the stem of the Hall-bar structure with the width of 10 μm as shown in Fig. 4.3(c). The magnetic field distributions are seen to be broadened in the center region where the 10 μm width stem crosses with the bar with the width of 25 μm. Similar structures are seen in the magnetic field distribution at $I_{\rm sample} = 2.8$ μA (Fig. 4.3(d)) although the signal-to-noise ratio was degraded.

We demonstrate two mapping results measured at different current directions. Fig. 4.4 indicates mappings of flux distribution in same sample at $T = 3.8$ K for current $I_{sample} = 70$ μA flowing (a) straight from downward to upward, and (b) from left to upward. The height of the SQUID probe from the sample surface was 1.5 μm.

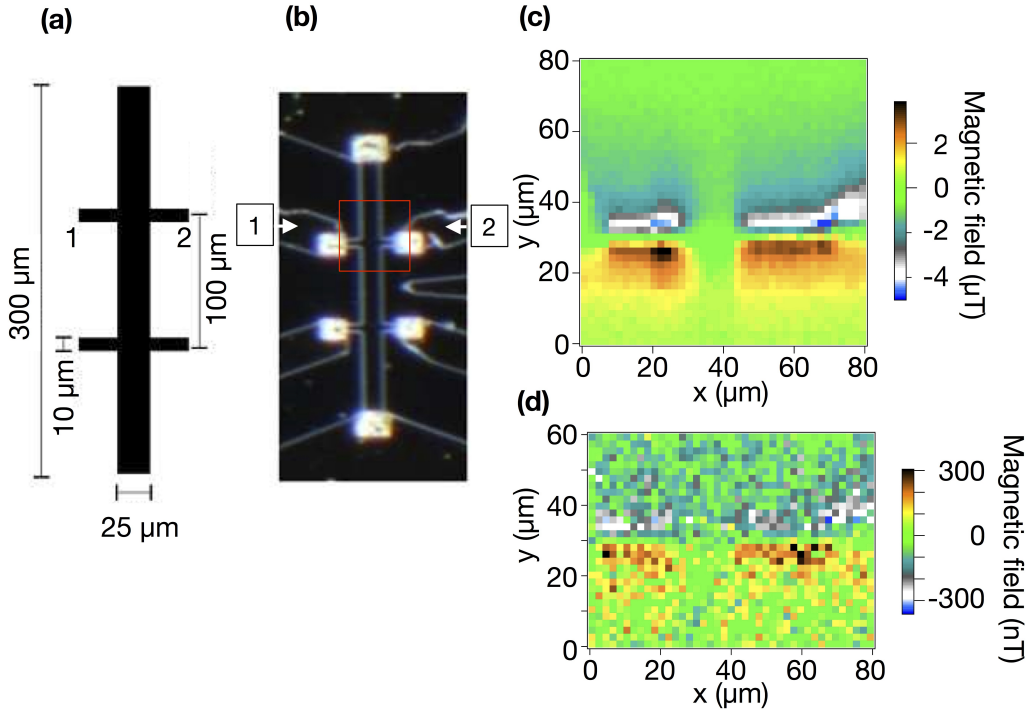

Fig. 4.3: (a) Schematic structure of a sample Hall-bar. (b) Optical micrograph of a sample Hall-bar structure. Red square indicates the scanning area of 80 μm $\times$ 80 μm for (c). Mappings of magnetic field distribution induced by current in a GaAs/$Al_xGa_{1-x}As$ modulation-doped single heterojunction sample at $T = 4$ K for current (c) $I_{\mathrm{sample}} = 70$ and (d) 2.8 μA at the applied magnetic field by a superconducting magnet of 0.0 mT using a nano-SQUID probe after mechanical polishing of the tip of the probe. The height of the SQUID probe from the sample surface was 1.5 μm.

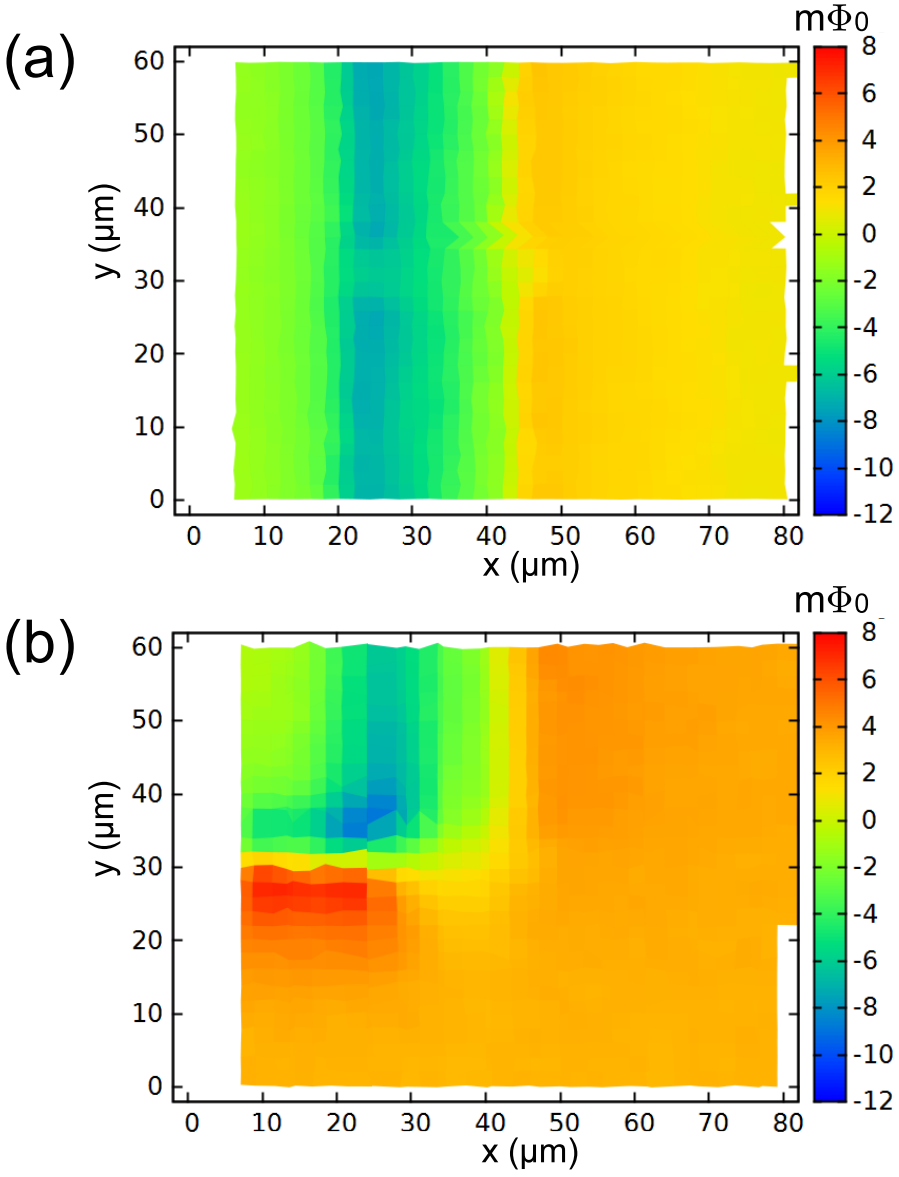

Fig. 4.4: Mappings of flux distribution in GaAs/$Al_xGa_{1-x}As$ modulation-doped single heterojunction sample at $T = 3.8$ K for current $I_{sample} = 70$ μA flowing (a) straight from downward to upward, and (b) from left to upward. The height of the SQUID probe from the sample surface is 1.5 μm.

Height dependence of flux distribution

We describe on the height dependence of scanning image of local magnetic field induced by current flowing in 2DEG. Figures 4.5 and 4.6 show line profiles of magnetic flux and scanning images measured at different height. Sample current was 70 μA as in the case of Fig. 4.3 (c). Magnitude of magnetic flux decreases with increasing the distance from the sample surface. As clearly seen in Fig. 4.6, the distance between the negative and the positive peaks is wider with the increase in the height. These results demonstrate that the minimum detectable magnetic flux and the spatial resolution are improved with decreasing the distance between the nano-SQUID and the sample surface.

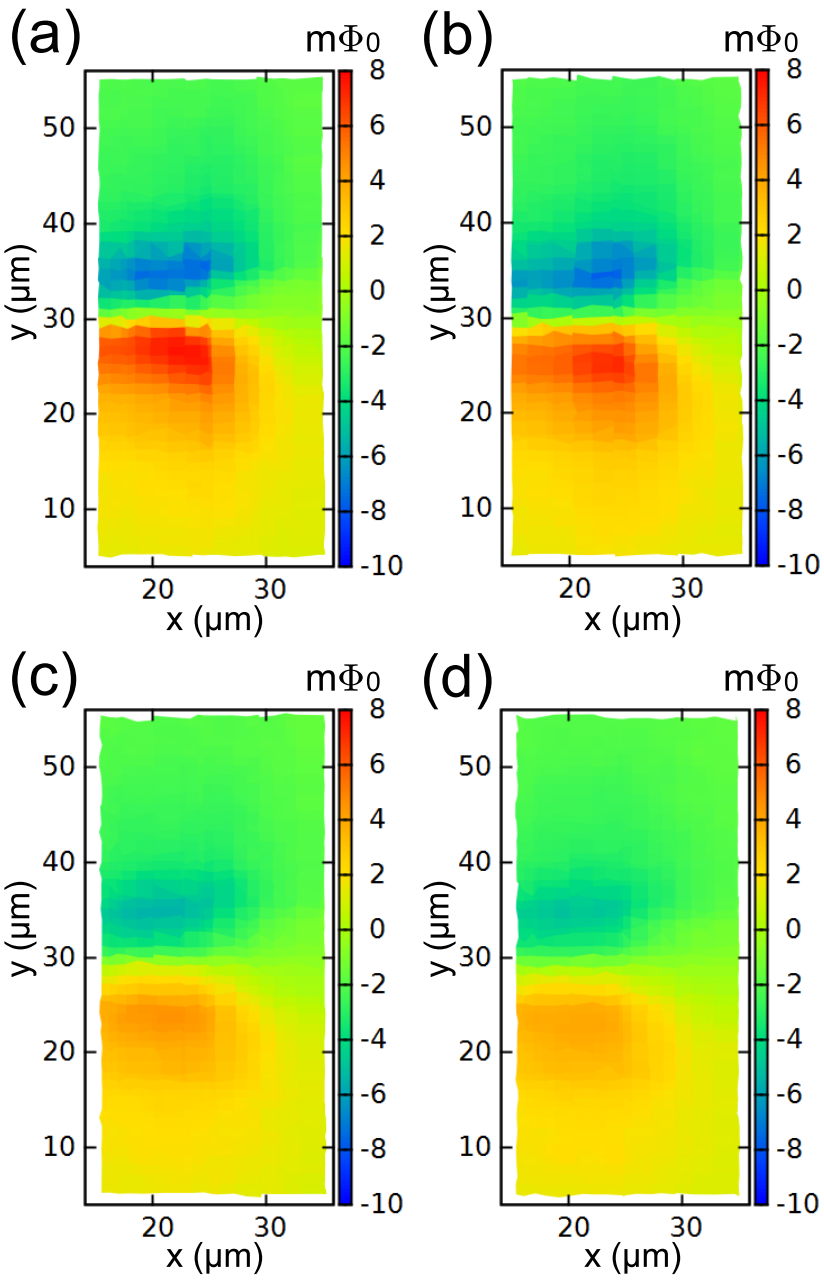

Fig. 4.5: (a)-(d) SQUID height dependence of mappings of flux distribution in GaAs/$Al_xGa_{1-x}As$ modulation-doped single heterojunction sample induced by sample current $I_{\text{sample}} = 70$ μA applied between the voltage probes 1 and 2 of the Hall-bar structure. The height of the SQUID probe from the sample surface was (a) 1.0, (b) 1.5, (c) 2.5, and (d) 3.5 μm.

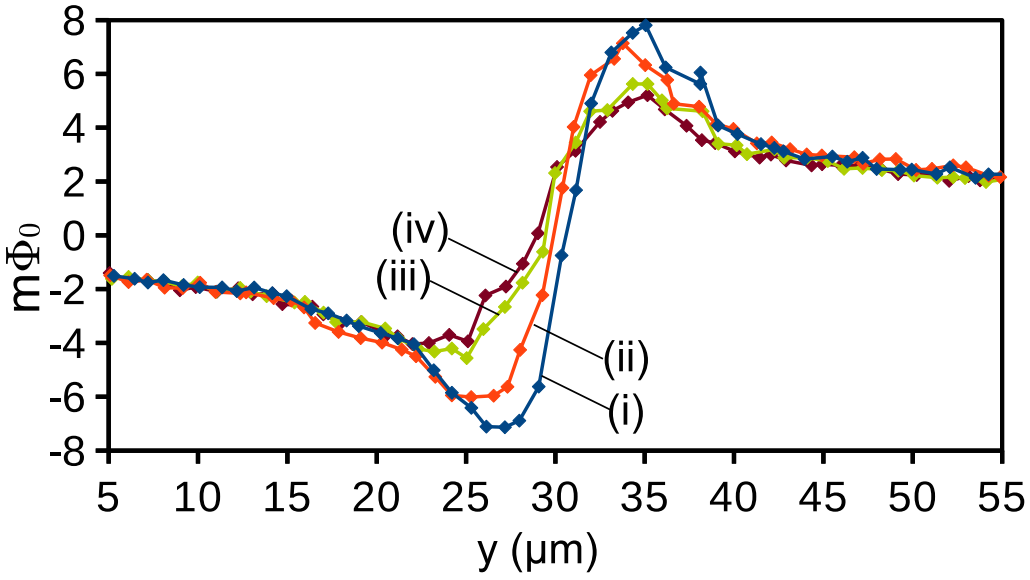

Fig. 4.6: Height dependence of line profiles of flux distribution in Figs. 4.5 (a), (b), (c) and (d) at $X = 20$ μm. The height of the SQUID probe from the sample surface was (i) 1.0, (ii) 1.5, (iii) 2.5, and (iv) 3.5 μm.

4.4 Reconstruction of two-dimensional current density distribution

We use the algorithm to obtain two-dimensional current distribution from the measured flux distribution based on Fourier analysis. [47] Two-dimensional current distribution is shown to be reconstructed from the magnetic flux distribution uniquely, although no algorithm is known to reconstruct three-dimensional current distribution from the magnetic flux distribution measured using a SQUID probe at a constant height scanning.

Magnetic field $\mathbf{B}(\mathbf{r}) = (B_x, B_y, B_z)$ induced by the current density $\mathbf{J}(\mathbf{r}) = (J_x, J_y, J_z)$ is given by the law of Biot and Savart

$$\mathbf{B}(\mathbf{r}) = \frac{\mu_0}{4\pi} \int \frac{\mathbf{J}(\mathbf{r}') \times (\mathbf{r} - \mathbf{r}')}{|\mathbf{r} - \mathbf{r}'|^3} d^3\mathbf{r}'. \tag{4.1}$$

The Green's function is defined by

$$G(x - x', y - y', z) = \frac{\mu_0 d}{4\pi} z \frac{1}{[(x - x')^2 + (y - y')^2 + z^2]^{3/2}}, \tag{4.2}$$

where d is the thickness of the current. By using $G(x - x', y - y', z)$, B_x is given by

$$B_x(\mathbf{r}) = \int_{-\infty}^{\infty}\int_{-\infty}^{\infty} G(x - x', y - y', z) J_y(x', y') dx' dy'. \tag{4.3}$$

Two-dimensional current density distribution $\mathbf{J}(x, y)$ can be reconstructed from the measured magnetic flux distribution $\mathbf{B}(x, y, z)$ based on a Fourier analysis. [47] The two-dimensional Fourier transform of the current density and magnetic field is defined by

$$j_y(k_x, k_y) = \int_{-\infty}^{\infty}\int_{-\infty}^{\infty} J_y(x, y) e^{i(k_x x + k_y y)} dx dy \tag{4.4}$$

and

$$b_x(k_x, k_y, z) = \int_{-\infty}^{\infty}\int_{-\infty}^{\infty} B_x(x, y, z) e^{i(k_x x + k_y y)} dx dy, \tag{4.5}$$

respectively. By using the two-dimensional Fourier transform of the Green's function

$$g(k_x, k_y, z) = \frac{\mu_0 d}{2} e^{-k_0 z}, \tag{4.6}$$

we have

$$b_x(k_x, k_y, z) = g(k_x, k_y, z) j_y(k_x, k_y), \tag{4.7}$$

where d is the thickness of the current and we defined $k_0 = \sqrt{k_x^2 + k_y^2}$. Similarly, b_z is given by

$$b_z(k_x, k_y, z) = ig(k_x, k_y, z) \left(\frac{k_y}{k_0} j_x(k_x, k_y) - \frac{k_x}{k_0} j_y(k_x, k_y) \right). \tag{4.8}$$

We assume quasi-stationary current density $\nabla \cdot \mathbf{J}(x, y) = 0$ in real-space and $-ik_x j_x(k_x, k_y) - ik_y j_y(k_x, k_y) = 0$ in k-space. A nano-SQUID probe facing θ to the surface of the sample detects $B_M(x, y, z) = B_x(x, y, z)\sin\theta + B_z(x, y, z)\cos\theta$. Because a nano-SQUID detects magnetic field averaged over the square SQUID loop, the Fourier transform of measured magnetic field $b_M(k_x, k_y, z)$ should be divided by [47]

$$h(k_x, k_y) = \frac{\sin(k_x L_{\mathrm{SQ}}/2)}{k_x L_{\mathrm{SQ}}/2} \frac{\sin(k_y L_{\mathrm{SQ}}/2)}{k_y L_{\mathrm{SQ}}/2}, \tag{4.9}$$

where L_{SQ} is the size of the SQUID loop to take into account the finite size of the SQUID in x- and y-directions. In the case of our nano-SQUID, $h(k_x, k_y)$ does not introduce noticeable difference because L_{SQ} is smaller than the step size of the measurement. For the z-direction, we assume a SQUID probe detects the average magnetic field B_{ave} at the effective height z_{eff} satisfying

$$B_{\mathrm{ave}} = \frac{\mu_0 I}{2\pi} \frac{1}{L_{\mathrm{SQ}}\sin\theta} \int_{z_0}^{z_0 + L_{\mathrm{SQ}}\sin\theta} \frac{\mathrm{d}z}{z} = \frac{\mu_0 I}{2\pi} \frac{1}{z_{\mathrm{eff}}}. \tag{4.10}$$

For $z_0 = 1.5$ μm, $L_{\mathrm{SQ}} = 1.0$ μm, and $\theta = 51°$, we obtain $z_{\mathrm{eff}} = 1.86$ μm.

We substitute $j_x = -\frac{k_y}{k_x} j_y$, into Eq.(4.8), and using Eq.(4.7), we obtain

$$b_M(k_x, k_y, z_{\mathrm{eff}}) = g(k_x, k_y, z_{\mathrm{eff}}) \left(\sin\theta - i \frac{k_0}{k_x} \cos\theta \right) j_y(k_x, k_y). \tag{4.11}$$

The current density can be readily obtained as

$$j_y(k_x, k_y) = \frac{2}{g(k_x, k_y, z_{\mathrm{eff}})} \frac{\sin\theta + i\frac{k_0}{k_x}\cos\theta}{\sin^2\theta + \frac{k_0^2}{k_x^2}\cos^2\theta} b_M(k_x, k_y, z_{\mathrm{eff}}) \tag{4.12}$$

in k-space and

$$J_y(x, y) = \frac{1}{(2\pi)^2} \int_{-\infty}^{\infty} \int_{-\infty}^{\infty} j_y(k_x, k_y) e^{-i(k_x x + k_y y)} dk_x dk_y \tag{4.13}$$

in real-space. $J_x(x,y)$ may be similarly obtained by using $j_x = -\frac{k_y}{k_x} j_y$. For the case of $k_x = k_y = 0$, $j_x(0,0)$ and $j_y(0,0)$ cannot be determined from $b_M(k_x, k_y, z_{\text{eff}})$. The obtained J_x and J_y have ambiguity by uniform current density distribution. In the following analysis, we set this uniform current density as zero. Figs. 4.8 (a), (b), (c), and (d) show reconstructed current density distributions $J_x(x,y)$ and $J_y(x,y)$ from the measured magnetic flux in Figs. 4.3 (c) and (d) at $I_{\text{sample}} = 70$ and 2.8 μA, respectively, for $\theta = 51°$. Calculations were performed on a mesh of 128×128 in the x and y directions. Figs. 4.7(a), (b) and (c) show reconstructed current density distribution $J_x(x,y)$ from the magnetic flux in Fig. 4.3(c) by using different type of window functions. $J_x(x,y)$ using a Hanning window [47, 65]

$$W(k) = \begin{cases} \frac{1}{2}\left(1 + \cos\left(\pi k / k_{max}\right)\right), & k < k_{max} \\ 0, & k > k_{max} \end{cases} \tag{4.14}$$

is shown in Fig. 4.7(a). $J_x(x,y)$ using a Parzen window [47, 65]

$$W(k) = \begin{cases} 1 - k/k_{max}, & k < k_{max} \\ 0, & k > k_{max} \end{cases} \tag{4.15}$$

was shown in Fig. 4.7(b). $J_x(x,y)$ using a Welch window [47, 65]

$$W(k) = \begin{cases} 1 - \left(k/k_{max}\right)^2, & k < k_{max} \\ 0, & k > k_{max} \end{cases} \tag{4.16}$$

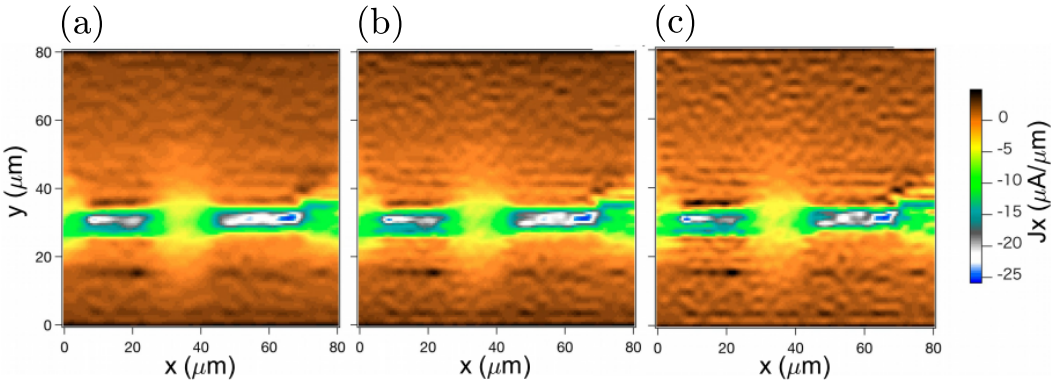

Fig. 4.7: Reconstructed current density $J_x(x,y)$ of magnetic field distribution shown in Fig. 4.3(c) with using a Hanning wiondow (a), a Parzen window (b) and a Welch window (c).

was shown in Fig. 4.7(c). In all the cases, we chose $k_{\max} = 1.5 \times 10^6$ m^{-1}. The image using a Welch window seems to contain the most high-spatial-frequency components. On the other hand, a Hanning widow seems to be the narrowest filter. In the following discussions, we used a Parzen window to eliminate high-spatial-frequency components of measured mappings [47]. We empirically chose $k_{\max} = 1.5 \times 10^6$ and 6.9×10^5 m^{-1} for $I_{\text{sample}} = 70$ and 2.8 μA, respectively, so that high-spatial-frequency noise is effectively reduced with minimum loss of spatial resolution. In the center region, where the 10 μm-stem crosses the bar with the width of 25 μm, the current density $J_x(x, y)$ is seen to spread to the wider bar. This can be more clearly indicated in $J_y(x, y)$ in Fig. 4.8(b) by the positive and negative current density near the corners of the mesa structure of the Hall-bar. At smaller current of $I_{\text{sample}} = 2.8$ μA, the main features of the current densities can still be resolved as shown in Figs. 4.8(c) and (d). Although the signal-to-noise ratio of the mapping of magnetic field in Fig. 4.3(d) is heavily degraded as compared to the case of $I_{\text{sample}} = 70$ μA in Fig. 4.3(c), the current densities are recovered at the expense of degraded spatial resolution by using $k_{\max} = 6.8 \times 10^5$ m^{-1} used for the Parzen window. The mappings of the magnetic field (Fig. 4.3(c)) and the reconstructed current density distributions (Figs. 4.8(a), (b)) using the nano-SQUID probe after mechanical polishing show remarkably better spatial resolution as compared to the mappings using the nano-SQUID probe without mechanical polishing (Figs. 4.9(c),(d)).This shows the advantage of the nano-SQUID probe after mechanical polishing over the unpolished nano-SQUID probe although the zero resistance was not observed due to the damage of Nb film in the polished nano-SQUID probe. The current obtained by integrating current densities $J_x(x, y)$ on the white bars in Fig. 4.8(a) is 84 and 91 μA for the crosssection A-B and C-D, respectively, in reasonable agreement with $I_{\text{sample}} = 70$ μA. Similarly, current across the white bars in Fig. 4.8(c) is 4.5 and 4.6 μA for the crosssection A-B and C-D, respectively, for $I_{\text{sample}} = 2.8$ μA.

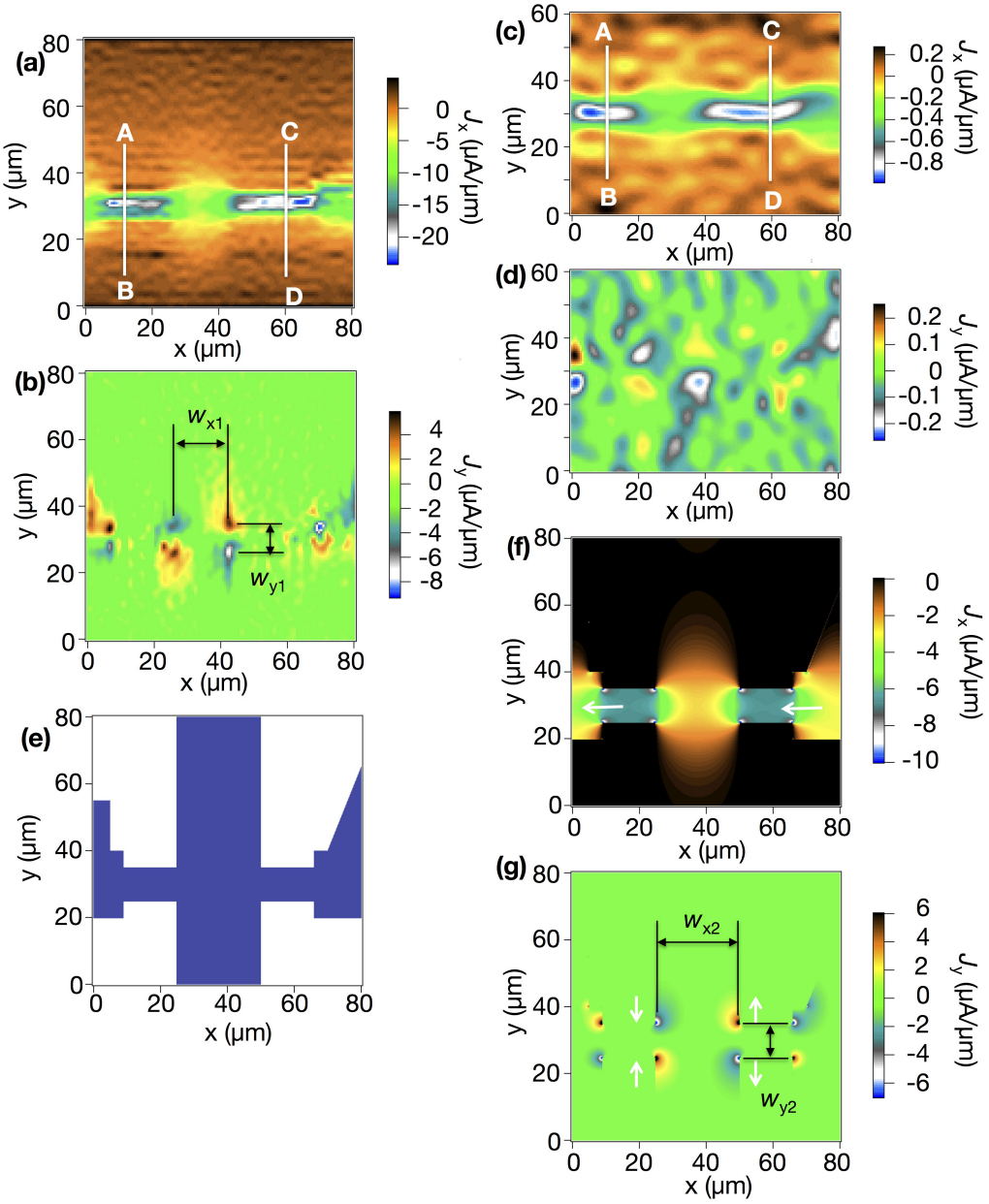

Fig. 4.8: (a) Reconstructed current density distributions $J_x(x, y)$ and (b) $J_y(x, y)$ from the measured magnetic flux in Fig. 4.3 at $I_{\text{sample}} = 70$ μA. (c) $J_x(x, y)$ and (d) $J_y(x, y)$ reconstructed from the measured magnetic flux in Fig. 4.3 at $I_{\text{sample}} = 2.8$ μA. (e) Pattern of Hall-bar structure assumed for $\sigma(x, y)$. Blue and white indicate area with $\sigma(x, y) = \sigma_0$ and $\sigma(x, y) = 0$, respectively. (f) Calculated current density $J_x(x, y)$ and (g) $J_y(x, y)$, assuming isotropic conductivity $\sigma(x, y)$. The white arrows indicate the direction of the current.

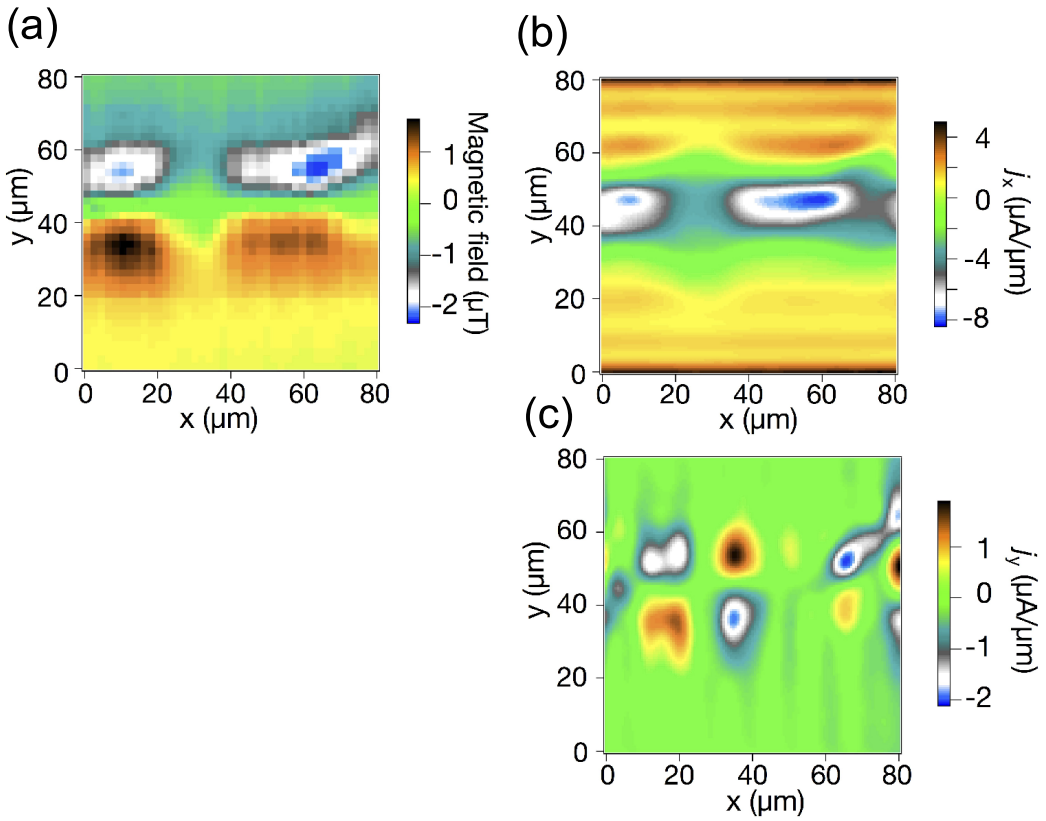

Fig. 4.9: (a) Mappings of magnetic field distribution induced by current in a GaAs/$Al_xGa_{1-x}As$ modulation-doped single heterojunction sample at $T = 4$ K using a nano-SQUID probe without mechanical polishing, at the applied magnetic field by a superconducting magnet of 0.25 mT. The current was $I_{\mathrm{sample}} = 70$ μA and the height of the SQUID probe from the sample surface was 4.0 μm. (b) Reconstructed current density distributions $J_x(x, y)$ and (c) $J_y(x, y)$ from the measured magnetic flux in (a) using $k_{\mathrm{max}} = 6.0 \times 10^5$ m^{-1} for the Parzen window.

4.5 Comparison of the measured current density with results of a numerical calculation

Two-dimensional quasi-stationary current density is calculated by assuming that the current density instantaneously responds to the electric field at the position of the electron as given by [66]

$$\mathbf{J}(x, y) = -\sigma(x, y)\nabla\phi(x, y), \tag{4.17}$$

which is applicable to a low mobility limiting case. Clearly, this model is not directly applicable to high mobility electron gas, nonetheless this model is useful to assist the understandings of the observed current density mappings by our SQUID microscope. One may refer to semiclassical [67, 68] or quantum mechanical [69] ballistic electron transport theories for more realistic descriptions. The measured current density $\mathbf{J}(x, y)$ may be described by the statistical or quantum mechanical average of the local electric current operator, which is described by the momentum $\mathbf{p}$ and the position $\mathbf{x}$ of an electron. Then ballistic electron transport theories take into account the scatterings of the electron from $\mathbf{p}$ to $\mathbf{p}'$ by such as the external electric field, the impurities, and the phonons. The description implied by Eq. (4.17) ignores these effects, in particular, the inertial motion of the current carrying electrons.

We also assume slow modulation frequency of the current with negligible displacement current $|\epsilon\partial\mathbf{E}/\partial t| << |\mathbf{J}|$ and isotropic conductivity $\sigma(x, y) = \sigma_{xx}(x, y) = \sigma_{yy}(x, y)$. Then we solve numerically

$$\nabla \cdot (\sigma(x, y)\nabla\phi(x, y)) = 0 \tag{4.18}$$

by a finite-difference method on a mesh of 400 × 400 with $\sigma_0 = 0.05$ S, where $\phi(x, y)$ is the electrostatic potential. Conductivity was assumed to be $\sigma(x, y) = \sigma_0$ inside the Hall bar structure and $\sigma(x, y) = 0$ elsewhere as shown in Fig. 4.8(e). Dirichlet boundary conditions were applied for x-direction, and the voltage was set to be -0.798 and 0 meV at $x = 0$ and 80 μm, respectively. A periodic boundary condition was applied to the y-direction. The electrostatic potential $\phi(x, y)$ was converged to an accuracy of less than 10^{-6} V.

Figs. 4.8(f) and 4.8(g) show calculated current density. The observed main features in Figs. 4.8(a) and 4.8(b) are reproduced in Figs. 4.8(f) and 4.8(g).

In particular, the spread of $J_x(x, y)$ to the wider stem of the Hall-bar in Fig. 4.8(a) is reproduced in Fig. 4.8(f), and the local maxima and minima in $J_y(x, y)$ near the corners of the mesa structure of the Hall-bar in Fig. 4.8(b) are reproduced in Fig. 4.8(g). The distances between the local maxima and minima in $J_y(x, y)$ are $w_{x1} = 16$ μm in Fig. 4.8(b) and $w_{x2} = 25$ μm in Fig. 4.8(g), indicating a sizable disagreement with $w_{x1} < w_{x2}$, whereas the difference in w_{y1} in Fig. 4.8(b) and w_{y2} in Fig. 4.8(g) is small. This disagreement is not explained by the finite k_{max} for the truncation of high-frequency components in the Fourier analysis. We calculated the magnetic field due to the calculated current density as given by Eq. (4.17), and reconstructed the current density distributions by changing k_{max} by the method described by Eqs. (4.1)-(4.15) and checked that $w_{\rm X2}$ and $w_{\rm Y2}$ did not depend on k_{max}. Consequently the disagreement between the observed and the calculated distances between the local maxima and minima in $J_y(x, y)$ is understood by the finite length that the electrons travel before they change momenta following the direction of the gradient of the electrostatic potential $\phi(x, y)$. The difference $w_{x2} - w_{x1} = 9$ μm is reasonably explained by the mean free path of the sample of 8.7 μm. Thus the disagreement between w_{x1} and w_{x2} is a manifestation of ballistic transport of the electrons. The reconstructed $J_x(x, y)$ in Fig. 4.8(a) is nearly symmetric and four main peaks in $20 < x < 50$ μm in Fig. 4.8(b) are nearly antisymmetric with respect to the center of the 25 μm-width bar, because ac bias current was applied to the Hall-bar structure and the magnetic field was detected synchronously using a lock-in amplifier. The effect of the limited spatial resolution due to small $k_{\rm max}$ is observed in Fig. 4.8(a) where the current density is larger at the center of the Hall-bar than the edge unlike the case in Fig. 4.8(f) where the current density is nearly homogeneous across the stem of the Hall-bar with the width of 10 μm. The depletion layer thickness was estimated to be 134 nm [62, 70] for similar GaAs single heterojunction sample with the electron density of 4.6×10^{15} m^{-2}. The height of the mesa structure of the sample was about 100 nm. Thus the depletion layer thickness of the two-dimensional electron gas and the widths of the lateral etching are too small to explain the measured current density distribution. Improvements in the signal-to-noise ratio of the magnetic flux measurements are required to increase $k_{\rm max}$ to obtain better spatial resolution.

4.6 Summary of local measurement of magnetic flux induced by current density in two-dimensional electron system

In this Chapter, we have described on our development of a weak-link nano-SQUIDs scanning microscope with small hysteresis in I-V curve and on reconstructions of two-dimensional current density vector in two-dimensional electron gas from measured magnetic field. We have constructed a weak-link scanning nano-SQUID microscope using a SQUID probe with small hysteresis in I-V curve suitable for a magnetic sensor for scanning measurements. We have measured magnetic field distribution created by the current in the Hall-bar structure. Two-dimensional current density components $J_x(x, y)$ and $J_y(x, y)$ were reconstructed from measured B based on a Fourier analysis. The reconstructed two-dimensional current density reproduced most of the features of current density calculated by solving Laplace equation, however, a significant deviation was found near the corners of the Hall-bar structure and was explained by ballistic electron transport.

Chapter 5

Local measurement of magnetic flux of tungsten carbide wire film sample

5.1 Background: tungsten carbide superconductor produced by FIB-CVD

FIB-CVD [71, 72, 73] with Ga^+ beam and tungsten hexacarboxyl ($W(CO)_6$) precursor [74, 75] is a promising technique to prepare superconducting films. FIB-CVD deposition of superconducting films has been acquired much interest as a template-free method to fabricate nano-SQUIDs that enables precise control of deposition, for example, at the apex of a probe tip of a scanning nano-SQUID microscope. A superconductor/normal metal/superconductor Josephson junction was fabricated using FIB-CVD and Fraunhofer oscillation of the critical current was observed [76]. FIB-CVD also provides a method to repair or modify superconducting circuits [77].

Thin films prepared by FIB-CVD of $W(CO)_6$ are amorphous with typical atomic concentrations of W: C: Ga = 40%: 40%: 20%, [74, 75] and are often called as tungsten-carbide (W-C) films. W-C nanowires were reported to exhibit superconductivity at a critical temperature T_c of 5.2 K, [74] which was much higher than the critical temperature of bulk crystalline tungsten of 0.01 K [78]. High T_c of W-C nanowires is associated with their amorphous structure [74, 79] . It has been shown that T_c of W-C wires was fitted well by a theory as a function of a parameter for the level of disorders [80, 81].

Superconductivity of W-C nanowires critically depends on the concentration of W. It was reported that W-C nanowires were superconducting for W concentration between 17.5 and 40% [81]. A tunneling spectroscopy measurement indicates that a W-C film has a superconducting gap of $\Delta = 0.66$ meV following s-wave BCS theory [82], while the melting transition in a vortex lattice was observed below T_c by scanning tunneling spectroscopy [42]. The current-voltage properties of W-C strips in high magnetic fields were reported to follow the quasi-three-dimensional vortex glass to liquid transition theory [83].

In this chapter, we investigate magnetic filed distribution in the vicinity of W-C films in an external magnetic field by a Nb weak-link scanning nano-SQUID microscope to explore superconducting properties of W-C films. Magnetic field distribution created by current flowing in a W-C strip is measured and the current density distribution in the W-C strip is reconstructed.

5.2 Tungsten carbide wire film sample

5.2.1 Fabrication of W-C samples

We used a dual-beam FIB-scanning electron microscope system (NB5000, Hitachi High-Technologies) to deposit W-C films. The acceleration voltage of Ga^+ ion beam was 40 kV and the base pressure was 1×10^{-4} Pa. We used tungsten hexacarboxyl ($W(CO)_6$) precursor. W-C films with thickness of 300 nm were grown with Ga^+ ion beam current of 700 pA at 1×10^{-3} Pa on a p-Si substrate. Nb/Au electrodes were fabricated by electron beam lithography with thicknesses of Nb and Au of 600 and 30 nm, respectively. Fig. 5.1(a) shows an optical micrograph of a deposited square W-C film with the size of 20 μm $\times$ 20 μm. On the left side of the square W-C film, two Nb/Au wires with a width of 2 μm were deposited. Fig. 5.1(b) shows an optical micrograph of a W-C strip with the size of 60 μm $\times$ 4 μm. Nb/Au wires were prepared for four-terminal electric transport measurements. In the vicinity of the W-C films, yellow blurred regions are seen in Fig. 5.1(a) and (b), due to unintentional deposition of W-C by the scatterings of ion beams. A part of the yellow blurred regions were milled by the FIB process as seen in the right half part in the dashed square in Fig. 5.1(b).

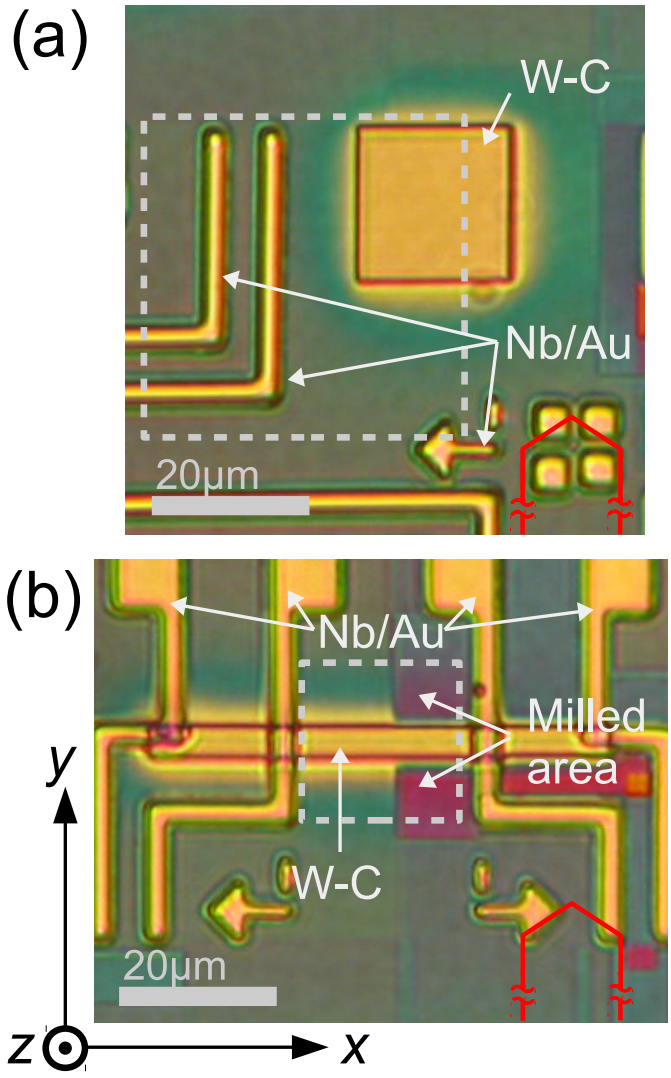

Fig. 5.1: (a) Optical micropraph of FIB assisted tungsten carbide film. The thickness and the size of tungsten carbide film was 300 nm and 20 μm$\times$ 20 μm, respectively. Two niobium wires are seen on the left part of the optical micrograph. (b) Optical micropraph of FIB assisted tungsten carbide wire with the size of 60 μm $\times$ 4 μm. Niobium wires were also deposited for four-terminal transport measurements. Dashed gray boxes indicate scanning area. Measurement configuration of a nano-SQUID probe is shown by red line.

5.2.2 Characteristics of W-C sample

An optical micrograph of a W-C film is shown in Fig. 5.1(a). The deposited W-C is seen to spread about several μm outside of the designed pattern of a square of 20 μm $\times$ 20 μm. This contrasts with the sharp edges of Nb/Au wires fabricated by EB lithography as seen in the left of the square W-C in Fig. 5.1(a). Temperature dependence of the four-terminal resistance (R) of the W-C wire sample is shown in Fig. 5.2(a) at an excitation current of 10μA at 0 T. Figure 5.2(a) indicates that the W-C sample is zero resistance below 5.5 K. The superconducting transition temperature T_c as defined by 10% of resistance drop from the resistance at the normal phase R_n ($R/R_n = 0.9$) is 5.9 K, which is comparable to the reported values of T_c = 4.8-6.2 K for W-C samples fabricated by FIB deposition [74, 75, 81, 82, 83]. Figure 5.3 shows current-voltage characteristics of the W-C wire sample without applying external magnetic field. The critical current density was estimated to be $J_c = 1.3\times10^6$ and 2.1×10^5 A/cm^2 at 2.0 and 4.0 K, respectively, which is slightly larger than the reported value for thin film of 1.5×10^5 A/cm^2 at 3 K [74] probably because of differences in the film thickness and the growth condition. Figure 5.2(b) shows perpendicular magnetic field dependence of resistance of the W-C wire sample at 2.0-5.0 K. The upper critical field B_{c2} is plotted in Fig. 5.2(c) as a function of T/T_c . The Ginzburg-Landau coherence length [50] is estimated to be $\xi_{GL}(0) = 5.8$ nm by using

$$B_{c2} = \frac{\Phi_0}{2\pi\xi_{GL}(0)^2}\left(1 - \frac{T}{T_c}\right). \tag{5.1}$$

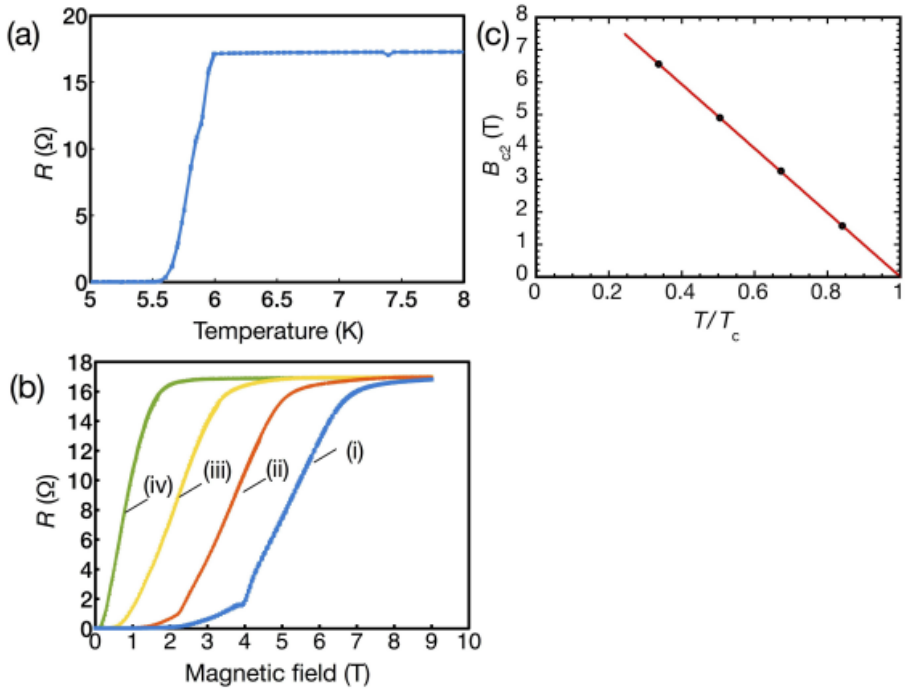

Fig. 5.2: (a) Temperature dependence of resistance of tungsten-carbide wire at 0 T. (b) Perpendicular magnetic field dependence of resistance of tungsten wire at (i) 2.0, (ii) 3.0, (iii) 4.0 and (iv) 5.0 K. (c) Upper critical field B_{c2} as a function of T/T_c. The red line is the best fitted line to Eq.(5.1).

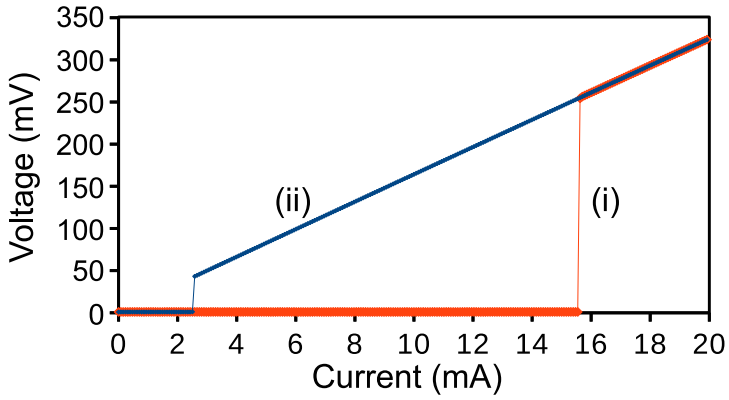

Fig. 5.3: Current-voltage characteristics of a tungsten-carbide wire shown in Fig. 5.1(b) at $T =$ (i) 2.0 and (ii) 4.0 K.

5.3 Mappings of flux distribution in W-C films

5.3.1 Measurement apparatus

We used the scanning nano-SQUID system to measure real-space imaging of magnetic field at surface of tungsten carbide film shown in Fig. 5.1(a). We investigate superconducting properties of tungsten carbide films. We used a SQUID probe without mechanical polishing, which was evaluated in Chapter 3 and the basic characteristics were shown in Fig. 3.7(a) and Fig. 3.8(a).

First, we describe the measurement apparatus for detection of wide range shift of magnetic filed. Because of screening by supercurrent, magnetic field on the surface of superconductors is expected to be reduced. In a measurement technique which we used in previous section, we had fixed the external magnetic field and current bias for achieving the maximum magnetic sensitivity. However, under the wide range of the change in magnetic field, it is difficult to keep the optimum conditions of SQUID operation for the maximum magnetic sensitivity.

To detect a large change in magnetic field with optimal sensitivity, we used a method to keep the magnetic flux penetrating the nano-SQUID constant while changing the external magnetic field $B_{\rm ext}$ applied by a superconducting magnet Figure 5.4 shows a schematic measurement circuit. A programmable dc voltage source (GS200, Yokogawa) was used as a constant voltage source $V_{\rm in}$. Constant current bias $I_{\rm sq}$ was applied to the SQUID probe by a voltage source $V_{\rm in}$ through a bias resistor of 3.78 kΩ. The output voltage signal from the SQUID $V_{\rm sq}$ was amplified at room temperature by a differential preamplifier (LI75A, NF corporation), and was detected using a digital multimeter (34401A, Agilent). The magnet current $I_{\rm mag}$ was supplied using a current source (R6142, Advantest). $I_{\rm sq}$ was set at the value for the maximum slope of $V_{\rm sq}$-$B_{\rm ext}$ curve, which was measured by the method described in Sec. 3.2.4 before a scanning operation. In this measurement, the voltage to magnetic field transfer function was 497 mT/V for $I_{\rm sq}$ of 209 μA at 3.7 K. On the sample surface, we measured a $V_{\rm sq}$-$B_{\rm ext}$ curve with the constant current bias $I_{\rm sq}$. We set a reference voltage $V_{\rm sq0}$ and a reference magnetic field $B_{\rm ext0}$ for the maximum slope of the curve. During the scanning measurements, $V_{\rm sq}$ was adjusted to be within $V_{\rm sq0} \pm \delta V$, where we set $\delta V = 0.5$ μV, giving the resolution of the magnetic field $\delta B = 0.12$ μ T. The magnetic field distribution on the sample surface was given by the feed back current $\delta I_{\rm mag}$ to the superconducting magnet.

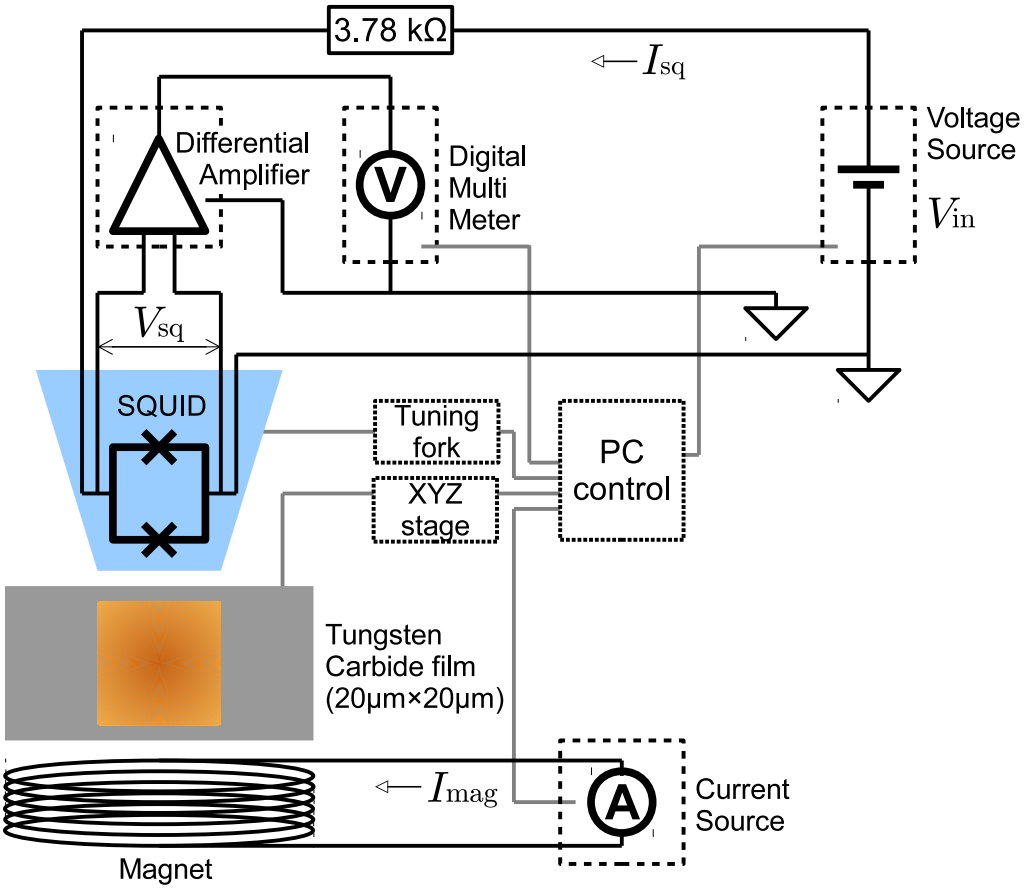

Fig. 5.4: Schematics of setup for mappings of magnetic field distribution in W-C films. Black lines and gray lines show a primary circuits and control connections, respectively. Constant current bias I_{sq} is applied to the SQUID probe by a voltage source V_{in} through a bias resistor of 3.78 kΩ. The output voltage signal from the SQUID V_{sq}, which is amplified at room temperature by a differential preamplifier, is detected using a digital multi meter. The magnet current I_{mag} is controlled from PC in order to keep V_{sq} constant.

5.3.2 Mapping of magnetic field change by W-C films

The scanning nano-SQUID microscopy was performed at a constant height mode with the distance between the SQUID probe and the sample surface of 3.5 μm. The scanning direction was parallel to the y-axis. Mapping of magnetic field normalized by magnetic field B_{ext0} of 0.171 mT is shown in Fig. 5.5(a). Reduction of magnetic field due to Meissner effect of the superconducting niobium wire with a width of about 4μm is clearly seen, however, the reduction of magnetic field on the square W-C film of 20 μm $\times$ 20 μm is small as shown in Fig. 5.5(a). A line profile of magnetic field change in Fig. 5.5(b) shows reduction of magnetic field due to niobium wires in the region $-13 < x < -17$ μm and at $-11 < x < -7$ μm. Reduction of magnetic field due to the W-C film was 0.9%.

5.4 Calculation of magnetic field distribution by a finite element method

Magnetic field distributions around Nb and W-C films were calculated by numerically solving the London equations by a finite element method. From Eq. (1.34), a kinetic momentum of an electron pair is given by

$$p = \hbar\nabla\phi = m^*\mathbf{v_s} + e^*\mathbf{A}. \tag{5.2}$$

By considering rotation of the momentum $\nabla \times p = \hbar\nabla \times \nabla\phi = 0$, Eq. (5.2) is rewritten as

$$m^*\nabla \times \mathbf{v_s} + e^*\nabla \times \mathbf{A} = 0. \tag{5.3}$$

By using superconducting current $\mathbf{J_s} = n_s^* e^* \mathbf{v_s}$, Eq. (5.3) becomes

$$\Lambda(\nabla \times \mathbf{J_s}) + \mathbf{B} = 0, \tag{5.4}$$

where $\Lambda \equiv \frac{m^*}{n_s^* e^{*2}}$ is a phenomenologial parameter. Eq. (5.4) is known as the second London equation and is a constitutive equation for the relation between superconducting current $\mathbf{J_s}$ and magnetic field $\mathbf{B}$ in superconductor. Considering a stationary state under constant magnetic field, we assume that electric field and the normal conducting current are zero. Using the

superconducting current $\mathbf{J_s} = \nabla \times \nabla \times \mathbf{A} = \frac{1}{\mu_0}\nabla \times \mathbf{B}$, Eq. (5.4) is given by

$$\begin{aligned} \frac{1}{\mu_0}\Lambda(\nabla \times \nabla \times \mathbf{B}) + \mathbf{B} &= 0 \\ -\frac{\Lambda}{\mu_0}\nabla^2\mathbf{B} + \mathbf{B} &= 0 \\ \nabla^2\mathbf{B} &= \frac{1}{\lambda^2}\mathbf{B}. \end{aligned} \tag{5.5}$$

Here λ is known as the penetration length of magnetic field and is defined by

$$\lambda \equiv \left(\frac{\Lambda}{\mu_0}\right)^{1/2} = \left(\frac{m^*}{\mu_0 n_s^* e^{*2}}\right)^{1/2}. \tag{5.6}$$

From Eq. (5.3), differential equations of the vector potential $\mathbf{A}$ and the superconducting current $\mathbf{J_s}$ are similarly given by

$$\nabla^2\mathbf{A} = \frac{1}{\lambda^2}\mathbf{A}, \tag{5.7}$$

$$\nabla^2\mathbf{J_s} = \frac{1}{\lambda^2}\mathbf{J_s}. \tag{5.8}$$

We assume that the vector potential $\mathbf{A}$ satisfies the following conditions

$$\nabla^2\mathbf{A} = \mu_0\mathbf{J}_s = \begin{cases} \frac{1}{\lambda^2} & \text{(inside of a superconductor)} \\ 0 & \text{(outside of a superconductor)} \end{cases} \tag{5.9}$$

Under this condition, Eq. (5.7) was numerically solved by a finite element method, and the vector potential $\mathbf{A}$ was obtained. We used a commercially available package (Comsol Physics).

Nb wires with 2 μm $\times$ 20 μm $\times$ 0.6 μm and a W-C film with 20 μm $\times$ 20 μm $\times$ 0.3 μm were assumed in the calculation. The London penetration depth λ for Nb wires was fixed to be 1 μm, while λ for a W-C film was varied between 0.85 and 1.6 μm. Figures 5.6(a) and (b) show calculated perpendicular magnetic field distribution (B_z) on the surface of Si substrate and a crosssection of at $y = 0$ μm and $z = 3.0$ μm at an external magnetic field of 0.171 mT. Figures 5.6(a) and 5.6(b) indicate that the reduction of the magnetic field is larger in the region above the W-C films than in the region above Nb wires, contradicting with our observations in Fig. 5.5. This result suggests that λ much larger than 1.6 μm for a W-C film should be

assumed to reproduce our result, or alternatively vortices are penetrating through the W-C film. λ and $\xi_{\rm GL}(0)$ for a W-C film with a thickness of 200 nm was estimated to be 850 and 6.25 nm, respectively [42]. It is unlikely to assume λ much larger than 1.6 μm because $T_c = 5.9$ K of our sample is larger than $T_c = 4.15$ K in the literature [42]. The external magnetic field of 0.171 mT is strong enough to allow penetration of vortices into the W-C film because we have $\Phi/\Phi_0 = 33.1$, where $\Phi = BA$ is the magnetic flux penetrating an area $A = 20 \times 20$ μm^2. Consequently, we consider the latter is more plausible, and calculated magnetic field distributions around Nb and W-C films by assuming 9 vortices are present in the square 20 μm $\times$ 20 μm W-C film as shown in Figs. 5.6(c) and 5.6(d). It has been shown by solving a linearlized Ginzburg-Landau equation [84, 85] that the Ginzburg-Landau free energy is lower for a square lattice of vortices than for a triangular lattice due to the square shape of the W-C film [86]. The lineprofiles in Fig. 5.6(d) for $\lambda = 1.4$ μm qualitatively reproduces our observation in Fig. 5.5.

Guillamon et al. performed low temperature scanning tunneling microscopy (STM) [82, 42] and spectroscopy measurements in W-C thin films, and they observed absence of hexagonal vortex lattice below about 0.2 T, instead they observed bunching of vortices close to linear depressions observed in a topographic STM image. The spacing between linear depressions was 100-300 nm, below the spatial resolution of our SQUID microscope. Moreover, they found that vortices at smooth and very flat regions change their position easily. The incomplete cancellation of the external magnetic field in the W-C film in our measurements is consistent with their observations.

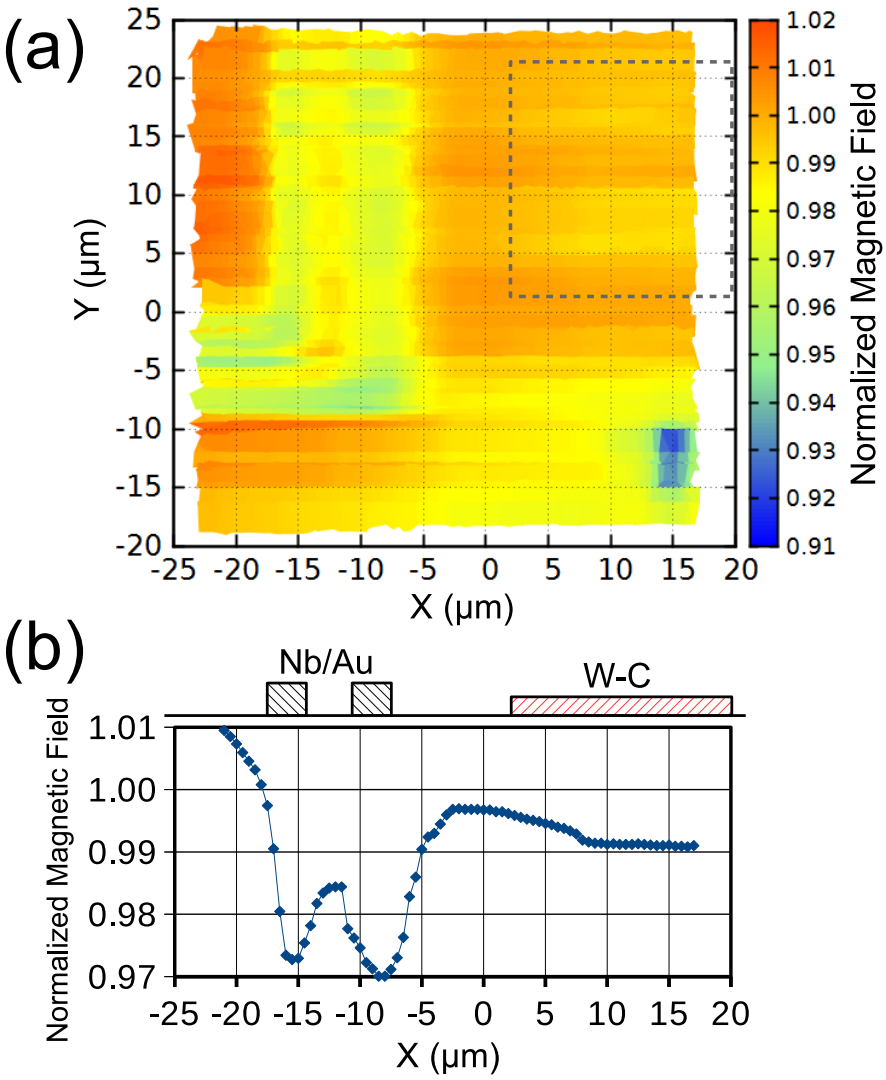

Fig. 5.5: (a) Mapping of magnetic field normalized by magnetic field of 0.171 mT at (x, y)=(0 μm, 0 μm). A gray dashed box indicates the W-C film shown in Fig. 5.1(a). (b) A lineprofile of normalized magnetic field averaged at $6 \leq y \leq 10$ μm. Two black hashed boxes and a red hashed box show x-position of Nb films and W-C film.

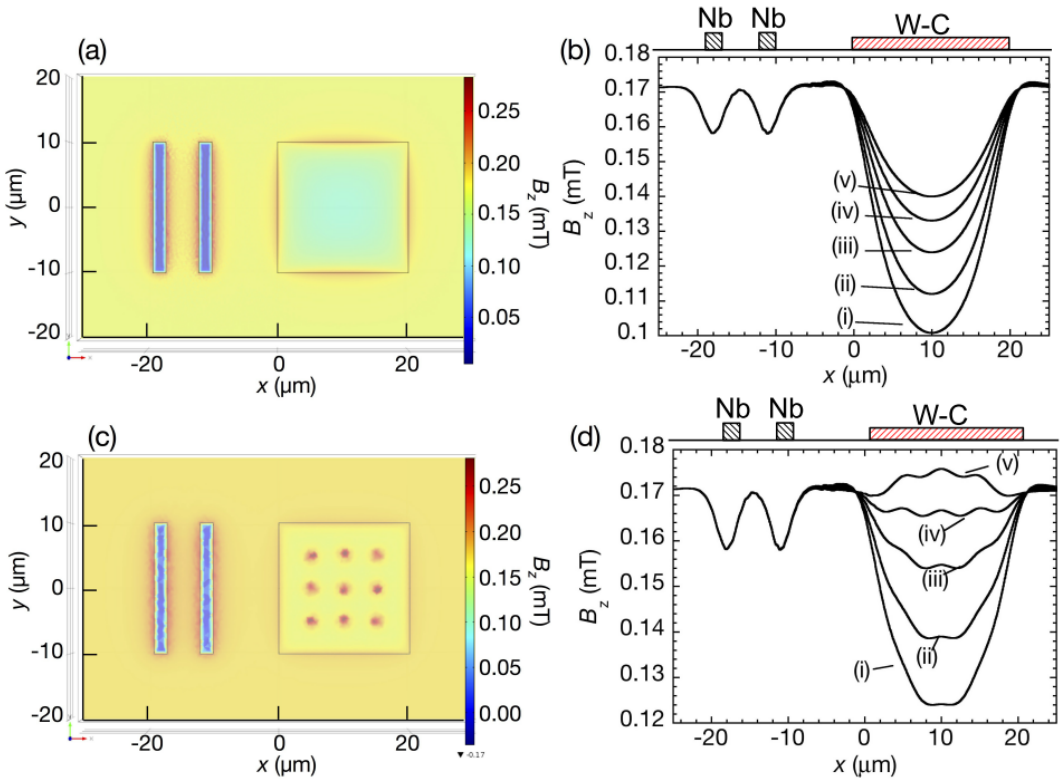

Fig. 5.6: (a) Calculated perpendicular magnetic field distribution (B_z) on the surface of the sample (z=0 μm). (b) Calculated perpendicular magnetic field distribution at y=0 μm and z=3.0 μm for λ = (i) 0.85, (ii) 1.0, (iii) 1.2, (iv) 1.4, and (v) 1.6 μm. Two black hashed boxes and a red hashed box show x-position of Nb films and W-C film. (c) (a) for the case of 9 vortices in the W-C sample. (d) (b) for the case of 9 vortices in the W-C sample.

5.5 Current density mapping

In order to estimate the current flow in the yellow blurred regions as shown in Fig. 5.1(b), we have conducted a measurement of the magnetic flux distributions due to current flowing in the W-C strip with the scanning area as shown in Fig. 5.1(b). We applied AC current of 70 μA to the W-C strip at the frequency of 1873 Hz at the external magnetic field of 0.17 mT. The AC current was well below the critical current of the W-C strip of 400 μA at 4.3 K. The height of the SQUID probe was 3.5 μm from the surface of the Si substrate. The obtained magnetic flux distribution is shown in Fig. 5.7(a). Current density distribution is reconstructed by a Fourier analysis by assuming two-dimensional current density distribution and is shown in Fig. 5.7(b). Figs. 5.7(a) and 5.7(b) indicate that the current flows primarily in the designed area of the W-C strip, and the current density in the unintentionally deposited W-C by scatterings of the ion beam is small.

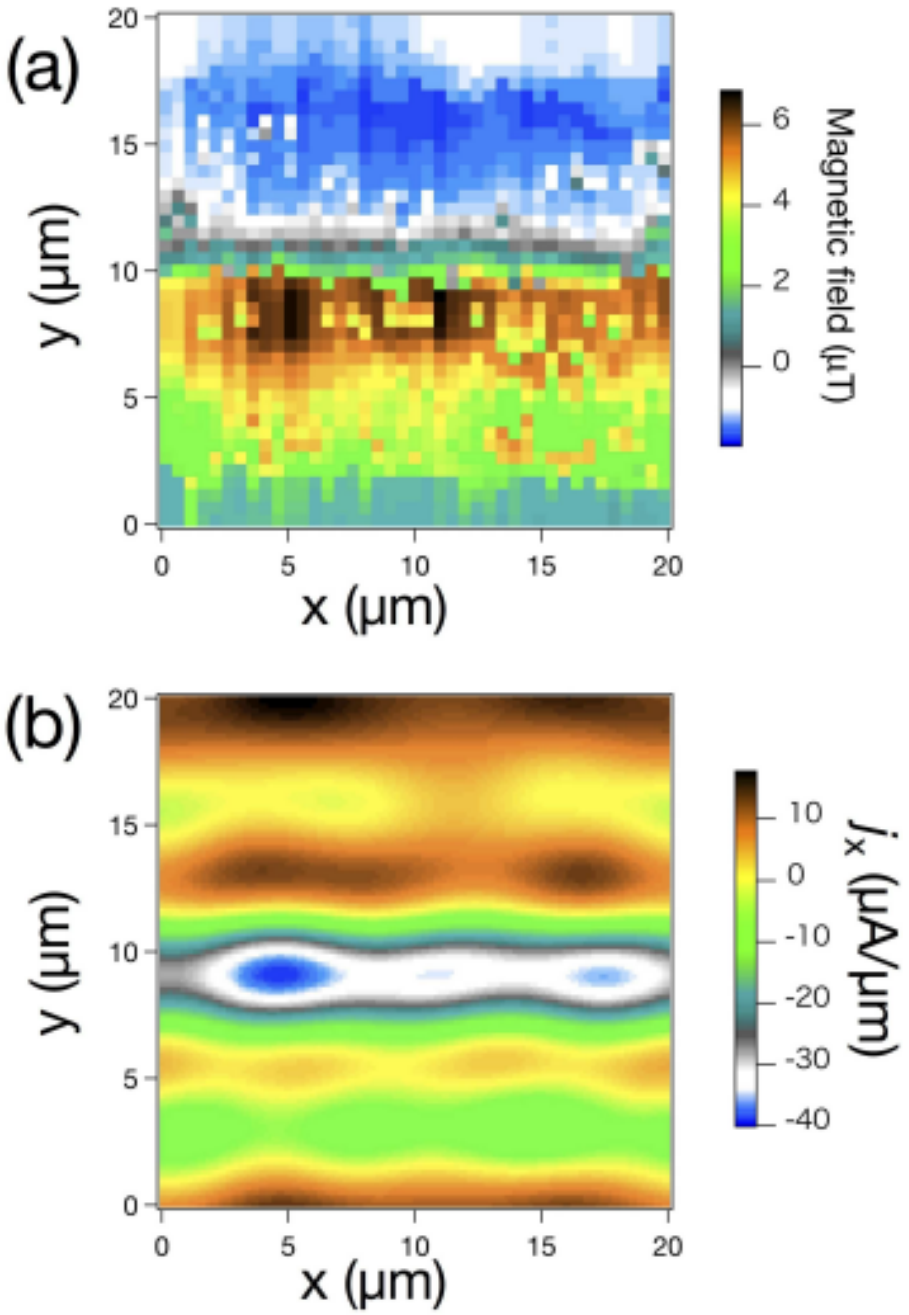

Fig. 5.7: (a) Magnetic field distribution due to current flowing in tungsten carbide wire at 4.3 K and at 0.2 mT. Applied current was ac 70 μA at frequency of 1873 Hz. (b) Reconstructed current density $j_x(x, y)$.

5.6 Summary of local measurement of magnetic flux of tungsten carbide wire film sample

In this Chapter, current density and magnetic flux imaging by scanning nano-SQUID microscopy have been presented on W-C films fabricated using FIB-CVD. First, reduction of magnetic field on Nb/Au wires and a W-C film has been measured. We have found that the reduction of magnetic field above the W-C film was 0.9%. The numerically calculated magnetic field distribution with vortices penetrating the W-C films qualitatively reproduces the measured magnetic field change. Second, current density distribution in a W-C strip has been reconstructed from the measured magnetic flux distribution flowing in the W-C strip. We have found that the current density in the unintentionally deposited W-C by scatterings of the ion beam is small. Our results indicate that FIB-CVD deposition of superconducting films is a promising template-free method to fabricate superconducting nano-devices such as nano-SQUIDs [7, 13].

Chapter 6

Conclusions

In this thesis, I have described development of a novel Nb weak-link nano-SQUID probe fabricated by a Bosch process and FIB milling technique, development of a novel scanning nano-SQUID microscope system, and its applications to characterize properties of semiconductors and superconductors.

First, I have demonstrated that the novel scanning nano-SQUID microscope system meets the required magnetic flux sensitivity and the spatial resolution to characterize properties of semiconductors and superconductors. The spatial resolution and the magnetic field sensitivity have been estimated to be less than 2 μm and 3.1 nT/Hz$^{1/2}$ at 2 kHz, respectively.

Second, I have successfully mapped magnetic field created by currents flowing in a Hall-bar structure of GaAs/Al_xGa_{1-x}As modulation-doped single heterojunction. Current density distributions in the two-dimensional electron gas have been reconstructed from the measured magnetic flux distributions, and good agreement has been obtained with the current distribution calculated by solving a Laplace equation. The reconstructed current density distributions have revealed ballistic nature of conductance in the 2DEG in GaAs/Al_xGa_{1-x}As modulation-doped single heterojunction.

Third, the scanning nano-SQUID microscope system has been demonstrated to be a powerful tool to characterize a tungsten carbide wire that has been attracting much interests recently because of potential large applications as nano-scale superconducting devices. Mappings of magnetic flux created by currents flowing in tungsten carbide wires and Nb/Au wires has been obtained and the current density distribution has been reconstructed. Meissner effect in tungsten carbide thin films has also been investigated by mappings of magnetic flux, indicating penetration of vortices in tungsten

carbide thin film.

I expect that the newly developed scanning nano-SQUID microscope system should further play large roles in characterizing a wide variety of semiconductor and superconductor nanostructure devices.

Bibliography

[1] R. C. Jaklevic, J. Lambe, A. H. Silver, and J. E. Mercereau, Phys. Rev. Lett. **12**, 159 (1964)

[2] J. Clarke and A. Braginski, *The SQUID Handbook: Fundamentals and Technology of SQUIDs and SQUID Systems* (Wiley-VCH Verlag, 2004)

[3] J. Gallop, Supercond. Sci. Technol. **16**, 1575 (2003)

[4] C. P. Foley and H. Hilgenkamp, Supercond. Sci. Technol. **22**, 064001 (2009)

[5] K. Hasselbach, C. Veauvy, and D. Mailly, Physica C **332**, 140 (2000)

[6] L. Hao, J. Macfarlane, J. Gallop, D. Cox, J. Beyer, D. Drung, and T. Schurig, Appl. Phys. Lett. **92**, 192507 (2008)

[7] D. C. Cox, J. C. Gallop, and L. Hao, Nanofabrication **1**, 53 (2014)

[8] G. J. Podd, G. D. Hutchinson, D. A. Williams, and D. G. Hasko, Phys. Rev. B **75**, 134501 (2007)

[9] C. D. Tesche and J. Clarke, J. Low. Temp. Phys. **29**, 301 (1977)

[10] C. Granata, A. Vettoliere, M. Russo, and B. Ruggiero, Phys. Rev. B **84**, 224516 (Dec 2011)

[11] W. Wernsdorfer, Supercond. Sci. Technol. **22**, 064013 (2009)

[12] W. Wernsdorfer, D. Mailly, and A. Benoit, J. Appl. Phys. **87**, 5094 (2000)

[13] T. Matsumoto, H. Kashiwaya, H. Shibata, H. Takayanagi, S. Nomura, and S. Kashiwaya, Physica C **471**, 1246 (2011)

[14] F. Baudenbacher, L. E. Fong, J. R. Holzer, and M. Radparvar, Appl. Phys. Lett. **82**, 3487 (2003)

[15] M. Faley, K. Pratt, R. Reineman, D. Schurig, S. Gott, C. Atwood, R. Sarwinski, D. Paulson, T. Starr, and R. Fagaly, Supercond. Sci. Technol. **17**, S324 (2004)

[16] J. Clarke, W. Goubau, and M. Ketchen, J. Low. Temp. Phys. **25**, 99 (1976)

[17] J. M. Martinis and J. Clarke, IEEE Trans. Magn. **19**, 446 (1983)

[18] V. V. Danilov, K. K. Likharev, and A. B. Zorin, IEEE Trans. Magn. **19**, 572 (1983)

[19] J. Kirtley, Rep. Prog. Phys. **73**, 126501 (2010)

[20] S. K. H. Lam and D. L. Tilbrook, Appl. Phys. Lett. **82**, 1078 (2003)

[21] W. Wernsdorfer, Advances in Chemical Physics **118**, 99 (2001)

[22] W. Wernsdorfer, K. Hasselbach, D. Mailly, B. Barbara, A. Benoit, L. Thomas, and G. Suran, J. Magnetism and Magnetic Materials **145**, 33 (1995)

[23] M. Jamet, W. Wernsdorfer, C. Thirion, D. Mailly, V. Dupuis, P. Melinon, and A. Perez, Phys. Rev. Lett. **86**, 4676 (2001)

[24] S. McVitie, R. Ferrier, J. Scott, G. White, and A. Gallagher, J. Appl. Phys. **89**, 3656 (2001)

[25] A. Sandhu, A. Okamoto, I. Shibasaki, and A. Oral, Microelectronic Engineering **73-74**, 524 (2004)

[26] A. Sandhu, K. Kurosawa, M. Dede, and A. Oral, Jpn. J. Appl. Phys. **43**, 777 (2004)

[27] I. K. Kominis, T. W. Kornack, and M. V. Allred, J. C. Romalis, Nature **422**, 596 (2003)

[28] A. Gruber, A. Drabenstedt, C. Tietz, L. Fleury, J. Wrachtrup, and C. von Borczyskowski, Science **276**, 2012 (1997)

[29] R. Schirhagl, K. Chang, M. Loretz, and C. L. Degen, Annu. Rev. Phys. Chem. **65**, 83 (2014)

[30] B. L. T. Plourde and D. J. Van Harlingen, Rev. Sci. Instrum. **70**, 4344 (1999)

[31] D. Vasyukov, Y. Anahory, L. Embon, D. Halbertal, J. Cuppens, L. Neeman, A. Finkler, Y. Segev, Y. Myasoedov, M. L. Rappaport, M. E. Huber, and E. Zeldov, Nat. Nano. **9**, 639 (2013)

[32] L. N. Vu, M. S. Wistrom, and D. J. Van Harlingen, Appl. Phys. Lett. **63**, 1693 (1993)

[33] Y. Tokura, T. Honda, K. Tsubaki, and S. Tarucha, Phys. Rev. B **54**, 1947 (1996)

[34] C. Veauvy, K. Hasselbach, and D. Mailly, Rev. Sci. Instrum. **73**, 3825 (2002)

[35] N. C. Koshnick, M. E. Huber, J. A. Bert, C. W. Hicks, J. Large, H. Edwards, and K. A. Moler, Appl. Phys. Lett. **93**, 243101 (2008)

[36] C. W. Hicks, J. R. Kirtley, T. M. Lippman, N. C. Koshnick, M. E. Huber, Y. Maeno, W. M. Yuhasz, M. B. Maple, and K. A. Moler, Phys. Rev. B **81**, 214501 (2010)

[37] K. C. Nowack, E. M. Spanton, M. Baenninger, M. Knig, J. R. Kirtley, B. Kalisky, C. Ames, P. Leubner, C. Brne, H. Buhmann, L. W. Molenkamp, D. Goldhaber-Gordon, and K. A. Moler, Nat. Mater. **12**, 787 (2013)

[38] R. Proksch, G. D. Skidmore, E. D. Dahlberg, S. Foss, J. Schmidt, C. Merton, B. Walsh, and M. Dugas, Appl. Phys. Lett. **69**, 2599 (1996)

[39] A. J. Brook, S. J. Bending, J. Pinto, A. Oral, D. Ritchie, H. Beere, M. Henini, and A. Springthorpe, Appl. Phys. Lett. **82**, 3538 (2003)

[40] S. Wildermuth, S. Hofferberth, I. Lesanovsky, E. Haller, L. M. Andersson, S. Groth, I. Bar-Joseph, P. Kruger, and J. Schmiedmayer, Nature **435**, 440 (2005)

[41] Y. Zhang, J. Schubert, N. Wolters, M. Banzet, W. Zander, and H. Krause, Physica C **372-376**, 282 (2002)

[42] I. Guillamón, H. Suderow, A. Fernandez-Pacheco, J. Sesé, R. Córdoba, J. M. De Teresa, M. R. Ibarra, and S. Vieira, Nat. Phys. **5**, 651 (2009)

[43] L. Hao, J. Macfarlane, J. Gallop, E. Romans, D. Cox, D. Hutson, and J. Chen, IEEE Trans. Appl. Supercond. **17**, 742 (2007)

[44] A. Finkler, Y. Segev, Y. Myasoedov, M. L. Rappaport, L. Neeman, D. Vasyukov, E. Zeldov, M. E. Huber, J. Martin, and A. Yacoby, Nano Letters **10**, 1046 (2010)

[45] K. K. Likharev, Rev. Mod. Phys. **51**, 101 (1979)

[46] K. Hasselbach, D. Mailly, and J. R. Kirtley, J. of Appl. Phys. **91**, 4432 (2002)

[47] B. J. Roth, N. G. Sepulveda, and J. P. Wikswo, J. Appl. Phys. **65**, 361 (1989)

[48] J. Bardeen, L. Cooper, and J. J. R. Schrieffer, Phys. Rev. **108**, 1175 (1957)

[49] V. Ginzburg and L. Landau, Zh. Eksp. Teor. Fiz. **20**, 1064 (1950)

[50] M. Tinkham, *Introduction to superconductivity, 2nd ed.* (McGraw-Hill, 1996)

[51] T. V. Duzer and C. W. Turner, *Principles of superconductive devices and circuits* (E. Arnold, 1981)

[52] L. Gor'kov, Zh. Eksp. Teor. Fiz. **36**, 1918 (1959)

[53] G. B. Arfken and H. J. Weber, *Mathematical methods for physicists 6th ed* (ElsevierAcademic Press, 2005)

[54] L. G. Aslamazov and A. I. Larkin, JETP Lett. **9**, 87 (1968)

[55] R. P. Feynman, R. B. Leighton, and M. Sands, *The Feynman Lectures on Physics* (Addison-Wesley, 1964)

[56] B. Antonio and P. Gianfranco, *Physics and Application of the Josephson Effect* (Wiley, 1982)

[57] W. C. Stewart, Appl. Phys. Lett. **12**, 277 (1968)

[58] D. E. McCumber, J. Appl. Phys. **39**, 3113 (1968)

[59] J. Clarke and R. H. Koch, Science **242**, 217 (1988)

[60] K. Karrai and R. D. Grober, Appl. Phys. Lett. **66**, 1842 (1995)

[61] H. Ito, Y. Shibata, K. Furuya, S. Kashiwaya, Y. Ootuka, and S. Nomura, Physics Procedia **3**, 1171 (2010)

[62] H. Ito, K. Furuya, Y. Shibata, S. Kashiwaya, M. Yamaguchi, T. Akazaki, H. Tamura, Y. Ootuka, and S. Nomura, Phys. Rev. Lett. **107**, 256803 (2011)

[63] M. E. Cage, R. F. Dziuba, B. F. Field, E. R. Williams, S. M. Girvin, A. C. Gossard, D. C. Tsui, and R. J. Wagner, Phys. Rev. Lett. **51**, 1374 (1983)

[64] S. Komiyama, T. Takamasu, S. Hiyamizu, and S. Sasa, Solid State Commun. **54**, 479 (1985)

[65] W. H. Press, S. A. Teukolsky, W. T. Vetterling, and B. P. Flannery, *Numerical Recipes in C* (Cambridge University Press, Cambridge, 1988)

[66] M. Reiser, Comp. Meth. Appl. Mech. and Eng. **1**, 17 (1972)

[67] W. Fawcett, A. Boardman, and S. Swain, J. Phys. Chem. Solids. **31**, 1963 (1970)

[68] R. Hockney, R. Warriner, and M. Reiser, Electron. Lett. **10**, 484 (1974)

[69] S. E. Laux, A. Kumar, and M. V. Fischetti, J. Appl. Phys. **95**, 5545 (2004)

[70] S. Mamyouda, H. Ito, Y. Shibata, S. Kashiwaya, M. Yamaguchi, T. Akazaki, H. Tamura, Y. Ootuka, and S. Nomura, Nano Letters **15**, 2417 (2015)

[71] K. Gamo, N. Takakura, N. Samoto, R. Shimizu, and S. Namba, Jpn. J. Appl. Phys. **23**, L293 (1984)

[72] S. Matsui and Y. Ochiai, Nanotechnology **7**, 247 (1996)

[73] I. Utke, P. Hoffmann, and J. Melngailis, J. Vac. Sci. Technol. B **26**, 1197 (2008)

[74] E. S. Sadki, S. Ooi, and K. Hirata, Appl. Phys. Lett. **85**, 6206 (2004)

[75] E. Sadki, S. Ooi, and K. Hirata, Physica C: Superconductivity **426-431**, 547 (2005)

[76] J. Dai, R. Kometani, K. Onomitsu, Y. Krockenberger, H. Yamaguchi, S. Ishihara, and S. Warisawa, J. Micromech. Microeng. **24**, 055015 (2014)

[77] M. J. Martínez-Pérez, J. Sesé, F. Luis, R. Córdoba, D. Drung, T. Schurig, E. Bellido, R. d. Miguel, C. Gómez-Moreno, A. Lostao, and D. Ruíz-Molina, IEEE Trans. Appl. Super. **11**, 345 (2011)

[78] J. W. Gibson and R. A. Hein, Phys. Rev. Lett. **12**, 688 (1964)

[79] I. Luxmoore, I. Ross, A. Cullis, P. Fry, J. Orr, P. Buckle, and J. Jefferson, Thin Solid Films **515**, 6791 (2007)

[80] M. S. Osofsky, R. J. Soulen, J. H. Claassen, G. Trotter, H. Kim, and J. S. Horwitz, Phys. Rev. Lett. **87**, 197004 (2001)

[81] J. Dai, K. Onomitsu, R. Kometani, Y. Krockenberger, H. Yamaguchi, S. Ishihara, and S. Warisawa, Jpn. J. Appl. Phys. **52**, 075001 (2013)

[82] I. Guillamón, H. Suderow, S. Vieira, A. Fernández-Pacheco, J. Sesé, R. Córdoba, J. De Teresa, and M. Ibarra, New J. Phys. **10**, 093005 (2008)

[83] Y. Sun, J. Wang, W. Zhao, M. Tian, M. Singh, and M. H. W. Chan, Sci. Rep. **3**, 2307 (2013)

[84] L. F. Chibotaru, A. Ceulemans, V. Bruyndoncx, and V. V. Moshchalkov, Nature **408**, 833 (2000)

[85] T. Mertelj and V. V. Kabanov, Phys. Rev. B **67**, 134527 (2003)

[86] S. Kashiwaya, private communication.

Acknowledgments

I would like to express my deep gratitude to Prof. Shintaro Nomura, my research supervisor, for his patient guidance and useful critiques of this research work. I would also like to thank Dr. Satoshi Kashiwaya, for his advice and assistance in both of theoretical and experimental parts of this work. My grateful thanks are also extended to Dr. Hiromi Kashiwaya for fabricating the nano-SQUID samples by a FIB milling system, to Dr. Ryosuke Ihsiguro, who provided some tungsten carbide samples. Regarding to the nano-SQUID probes, I express my thanks to the members of research group of Prof. Hideaki Takayanagi for preparing some superconducting films. I would also like to extend my thanks to the professors in Tsukuba Nanotechnology Human Resource Development Program, especially Prof. Ota Norio and Prof. Kiyoshi Asakawa for their useful advises from an expanded perspective. I would like to thank to the members of research group of Prof. Nomura, especially Mr. Yuki Oshima for fabricating the Hall-bar sample. Finally, I wish to thank my parents and my friends for their support and encouragement throughout my study.
This thesis was partly supported by Tsukuba Nanotechnology Human Resource Development Program. For the sample fabrication process, a part of this study was supported by NIMS Nanofabrication Platform and AIST Nano-Processing Facility in Nanotechnology Platform Project sponsored by the Ministry of Education, Culture, Sports, Science and Technology (MEXT) of Japan. For the evaluation of samples, a part of this study was supported by Cryogenics Division and Open Facility Network Office in the Research Facility Center for Science and Technology of University of Tsukuba.